2020

# Synthesis, Conformational Analysis, and Thermodynamic Study of N1-cyclic Inosine Diphosphate Ribose and Its Analogs: Towards the SAR of a Calcium Ion Releasing Second Messenger

Wenjie Lyu

# SYNTHESIS, CONFORMATIONAL ANALYSIS, AND THERMODYNAMIC STUDY OF N1-CYCLIC INOSINE DIPHOSPHATE RIBOSE AND ITS ANALOGS: TOWARDS THE SAR OF A CALCIUM ION RELEASING SECOND MESSENGER

A thesis submitted in partial fulfillment

of the requirements for the degree of

MASTER OF SCIENCE

to the faculty of the

DEPARTMENT OF CHEMISTY

of

ST. JOHN'S COLLEGE OF LIBERAL ARTS AND SCIENCES

at

ST. JOHN'S UNIVERSITY

New York

by

Wenjie Lyu

Date Submitted _____ Date Approved _____

_____ _____

Wenjie Lyu Steven M. Graham

## ABSTRACT

SYNTHESIS, CONFORMATIONAL ANALYSIS, AND THERMODYNAMIC STUDY OF N1-CYCLIC INOSINE DIPHOSPHATE RIBOSE AND ITS ANALOGS: TOWARDS THE SAR OF A CALCIUM ION RELEASING SECOND MESSENGER

Wenjie Lyu

N1-cyclic inosine 5'-diphosphate ribose, another class of the well-known calcium second messenger cyclic adenosine 5'-diphospate ribose, reveals nearly identical concentration-response calcium releasing activity intracellularly in a Jurkat T-cells (JTC) system. In this study, a three steps synthetic route is proposed to synthesize cIDPR analog 8-bromo-N1-cIDPR (8-Br-N1-cIDPR), the first 8-substitued analog has agonistic activity. The structure-activity relationship (SAR) of this messenger was investigated by the knowledge of its conformational landscapes, determined by variable-temperature NMR spectroscopy, in conjunction with PSEUROT and population analysis, allowing the study of thermodynamic parameters. A pure in-phase (PIP) heteronuclear correlation NMR experiment was adopted for direct extraction of coupling constants of non-first order proton signals. 8-Br-N1-cIDPR in many ways shows the opposite thermodynamics compared to cADPR analogs, despite its clear agonistic behavior.

## DEDICATION

To my mama, the strongest woman, the *motivation*.

To Angela Ruiz, my othermother, the *inspiration*.

## ACKNOWLEDGEMENTS

I would like to express my sincere thanks to my research mentor, Dr. Steven M. Graham, for giving the opportunity to work on this project and always providing the guidance throughout this research. An absolute inspiration was given to me by him to explore the molecular world. A special thanks to all my lab mates, Sarah Saatori, Inis Serrano, Tanner Perez, Chiemeka Uwakwe, Brooke Butler, and Sarah Grega, for all the great memories and being each other's motivations. Deep and sincere gratitude to my committee, Dr. Joseph Serafin, Dr. Philip Lukeman, and Dr. David Brown, for their continued support and encouragement. Thanks to the Department of Chemistry at SJU, my completion of this project could not have accomplished without the help of all the faculty members and staffs. Special thanks to Eric C. Johnson, from Bruker Biospin, for modifying those excellent pulse programs for us.

Finally, to my family, my mother and my father, my deepest gratitude. A young boy who lived oversea away from his family since the age of 15 could not accomplish anything without their selfless love and support.

## TABLE OF CONTENTS

## LIST OF TABLES

## LIST OF FIGURES

## LIST OF SCHEMES

## INTRODUCTION

The oxidized form of nicotinamide adenine dinucleotide (NAD, **3**, Figure 1), abbreviated as $NAD^+$, plays a key role in biological system and has been traditionally described to be a cofactor in electron transfer during oxidoreduction reactions (***1***). Since the 1960's, beyond its role as an electron carrier in redox reactions, it was discovered that $NAD^+$ is also involved in non-redox pathways in cells (***2***), and soon been recognized as a key substrate in many biochemical activities (as illustrated in Figure 2), including covalent protein modifications via mono-ADP-ribosylation (MAR) and poly-ADP-ribosylation (PAR), deacetylation mediated via ADP-induced enzymes, and cell signaling via generation of cellular second messengers (***3***). $NAD^+$ levels remain extremely abundant in most living cells. In eukaryote cells, such as human cells, $NAD^+$ is synthesized via two major pathways: *de novo* pathway, which utilizes the tryptophan to generate quinolinic acid that ultimately is converted to $NAD^+$, and salvage pathway, which uses nicotinamide (Nam, **2**, Figure 1) to generate $NAD^+$ (***4***). Cellular $NAD^+$ levels appear to decline during chronological aging, and this decline is claimed to be the consequence of aging and cause the development of aging-related cellular dysfunction, suggesting the potential correlation between cellular NAD levels and lifespan (***3***,***5***,***6***). $NAD^+$ serves as the substrate for a large range of enzymes, including poly-ADP-ribose polymerases (PARPs), sirtuins (Sir2), and ADP-ribosyl cyclase. These enzymes modulate the degradation of $NAD^+$ to generate ADP-ribose derivatives that involved in biological activities. For example, $NAD^+$ is consumed via Sir2 in $NAD^+$-induced deacetylation of histones, and such deacetylation is responsible for aging, DNA repair, and apoptosis (***7***,***8***). These enzymes transfer acetyl groups from substrate proteins to the moiety of

$NAD^+$, releasing nicotinamide and O-acyl-ADP-ribose as side products (***9***). In poly-ADP-ribosylation, a post-translational modification (PTM) in cellular processes, $NAD^+$ is cleaved as substrate of poly-ADP-ribose polymerases (PARPs) to generate ADP-ribose monomers, serving as transferal units added onto proteins in large branched chains (***10***). Most MARs, PARs, as well as protein-conjugated MARs or PARs, including their derivatives, bind to macrodomain, a conserved protein fold that exists in all kingdoms of life, including viruses, bacteria, and eukaryotes (***11***). Regarding the viral macrodomains, the macrodomain sequence is found heavily conserved within non-structural protein 3 (nsP3) of alphaviruses and coronaviruses. Often the mutation of macrodomain does not attenuate the replication and virulence of the virus and leads to apoptosis, associated with the activation of PARPs, as shown in alphaviruses (***12***). However, one study revealed the mutation associated with respiratory syndrome coronavirus contributed to virus attenuation, moreover, it induced the sensitivity to interferon (IFN) and inflammatory cytokines (***13***). Such phenomenon was observed during the outbreak of SARS-CoV-2, known as COVID-19; a detrimental result of the infection was a cytokine storm (cytokine release syndrome), which contributed in multiple organ failures after the elimination of the virus (***14***). It was proposed that the use of PARP inhibitors could be used in the treatment in SARS-CoV-2 infection to block the cytokine storm, because of its ability to prevent the overactivation of PARs, though further clinical studies are highly required (***15***).

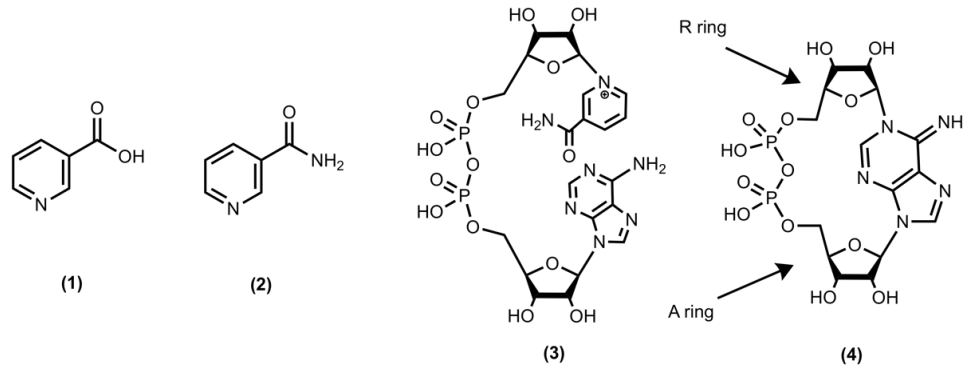


**Figure 1.** (1) Nicotinic acid. (2) Nicotinamide. (3) Nicotinamide adenine dinucleotide. (4) Cyclic adenosine 5'-diphosphate ribose.

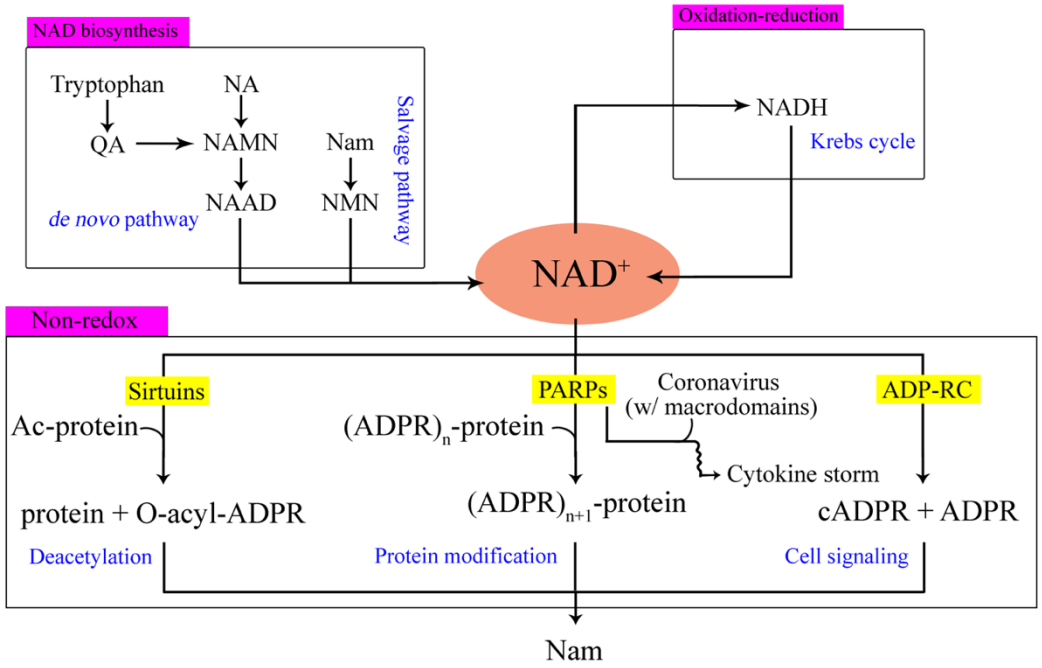


**Figure 2.**Shown here are the pathways for biosynthesis and non-redox degradation of $NAD^+$. The upper left side illustrates the biosynthesis of NAD in human cells from two pathways and three precursors, including a) *de novo* pathway: tryptophan is converted to nicotinic acid mononucleotide (NAMN) via quinolinic acid (QA), which is converted to nicotinic acid adenine dinucleotide (NAAD), the intermediate that can be ultimately amidated to $NAD^+$; b) nicotinic acid (NA, **1**, Figure 1) is converted to NAMN, and then follows the same process as de novo pathway; c) salvage pathway: nicotinamide (Nam) is converted to nicotinamide mononucleotide (NMN) by nicotinamide phosphoribosyl-transferase (NamPRT), the required enzyme, and NMN is the precursor for the synthesis of $NAD^+$. The upper right side shows how $NAD^+$ is involved in oxidation-reduction reactions in cells. In Krebs cycle, NAD is frequently used to be the electron carrier as energy fuels. The bottom half part demonstrates how $NAD^+$ is involved in non-redox processes, known as the degradation of NAD, including a) deacetylation mediated via sirtuins; b) poly-ADP ribosylation modulated by PARPs (such ribosylation can lead to cytokine storm during coronavirus infection); c) calcium ion releasing signaling by generating cAPDR via ADP-RC. The side product of these degradation is Nam, which can be recycled for the synthesis of NAD.

$NAD^+$ also serves, as relevant in this study, to be the precursor for the synthesis of cyclic adenosine 5'-diphosphate ribose (cADPR, **4a,** Figure 1), which is well recognized as the signaling molecule that causes intracellular calcium ion release. The enzymic cyclization was catalyzed by ADP-ribosyl cyclase, found in many cells, including CD38, the lymphocyte surface antigen in mammalian cells that has ADP-ribosyl cyclase activity, modulating both the synthesis and hydrolysis of cADPR (and its analogues) from $NAD^+$ molecule (and its analogues) (***16***,***17***). The release of calcium ions can ultimately lead to the increase of intracellular calcium levels, regulating series of cellular process (***18***). Such cellular processes are crucial and have shown to be important in many physiological conditions, including egg fertilization, skeletal and heart muscle contraction, and insulin secretion (***19***,***20***). The function of cADPR was first discovered in 1987 and soon established that it was an ubiquitous $Ca^{2+}$ -releasing second messenger (***21***), placing it alongside inositol-1,4,5-trisphophaste ($IP_3$), a known second messenger also participates in calcium release signaling. Despite the clear biological outcome cADPR formation leads to, the role of this second messenger in term of chemical mechanism in living cells is still poorly understood. It is well known that generation of cADPR intracellularly leads to the opening of the ryanodine receptors (RyR), the intracellular calcium channels located in the sarco-/endo-plasmic reticulum membrane, allowing $Ca^{2+}$ to efflux from the reticulum membrane. However, rather than directly bind to the RyR, it is generally believed that the physiological outcome of cADPR is mediated via other accessory proteins, such as calmodulin (***22***), and RyR activity is modulated by the resulting signaling (***23***) (Figure 3). In 1997, a study showed that cADPR was the ligand for FKBP12.6, a soluble receptor for the immunosuppressive drug FK506, and the binding of

cADPR on FKBP12.6 frees RyR from FKBP12.6 to relieve the inhibition of the channels, allowing the release of $Ca^{2+}$ (***24***). Contrarily, a 2001 report claimed that a tightly binding cADPR along the cell membrane in a sea urchin homogenate system was not affected by FK506 (tacrolimus) or the related rapamycin (***18***). One report claimed that when RyRs were blocked by a scorpion toxin, cADPR was still able to induce the increase of intracellular $Ca^{2+}$ level, suggesting that cADPR might not involve in the opening of RyR but functioning via some RyR-independent signaling mechanisms (***25***). In addition to $Ca^{2+}$ release via RyR, it was found that cADPR can directly induce intracellular $Ca^{2+}$ release in neutrophils and mediate $Ca^{2+}$ mobilization (***26***), and a recent study claimed that cADPR can regulate $Ca^{2+}$ influx via $Ca^{2+}$ permeable channels when cADPR binds and gates to TRPM2 channel, shedding light upon a different approach of the RyR-independent $Ca^{2+}$ signaling mechanism induced by cADPR (***27***). In summary, the discrepancy regarding the mechanism of cADPR as a calcium-releasing second messenger arise from the differences among species used in the studies, and the distinct isoforms of RyRs characterized in various tissues. Therefore, the absolute mechanism of this second messenger remains unclear. One approach to investigate the mechanism of cADPR for $Ca^{2+}$ signaling and the potential correlation between its structure and its obvious biological activity is to study the conformational landscapes of cADPR and its analogues. Such analogues should act as a potent agonist or antagonist, be ideally membrane permeable, and be relatively stable to hydrolysis (***28***). In addition, a close conformational analysis of these analogues and the similarity/difference of their conformations and thermodynamic properties in contrast to their parent cADPR are often desired for the study of structure-activity relationship (SAR). In our study on this

particular topic, most of our knowledge of the structure-activity relationship of cADPR and its analogues came from the synthesis and evaluation of these conformational landscape (***29***).

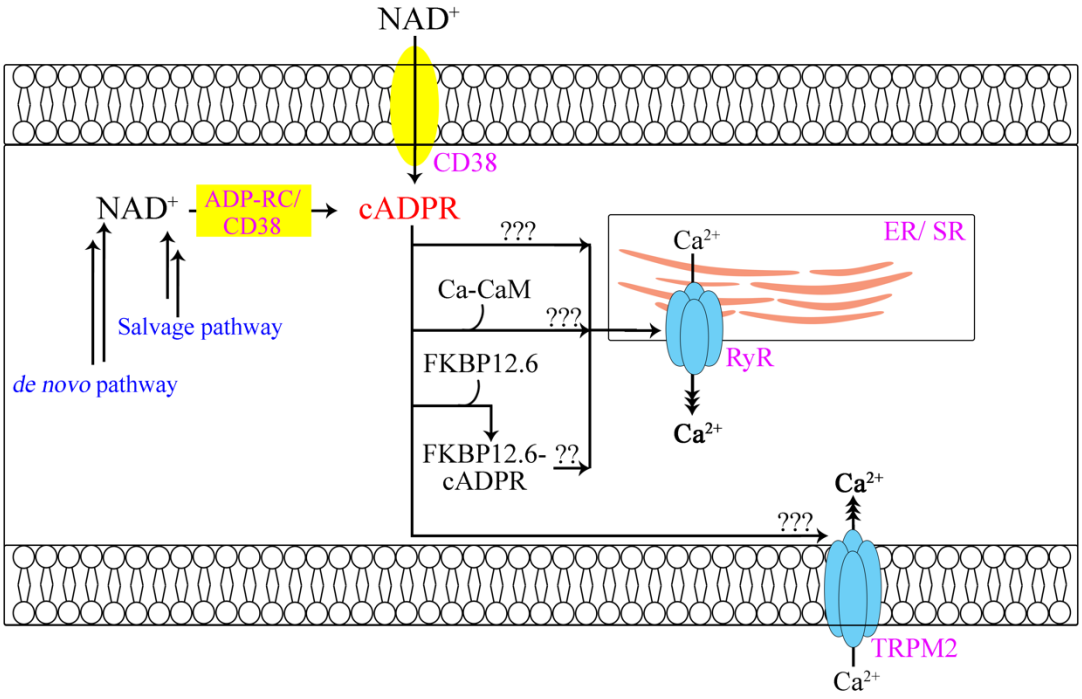


**Figure 3.** Physiological activities of intracellular and extracellular calcium releasing driven by cADPR. Two pathways are responsible for the synthesis of $NAD^+$ intracellularly, including *de novo* pathway and salvage pathway. Intracellular cADPR is synthesized from $NAD^+$ catalyzed by CD38/ADP-RC. Here illustrate four hypotheses on how cADPR modulates the calcium release: a) cADPR directly binds on RyR, modulating the intracellular calcium release from ER/SR; b) cADPR-RyR complex leads the intracellular calcium release mediated via calcium- calmodulin complex; c) cADPR binds to FKBP12.6 and the resulting complex modulates the intracellular calcium release; d) cADPR directly gates on TRPM2, causing calcium influx extracellularly.

**The SAR in cADPR and cIDPR analogues.** Since the discovery of the novel compound cADPR, there has been great in interest studying the analogues of cADPR to expand the knowledge for the SAR studies. There are many analogues that have been synthesized and studied (Table 1), including the parent molecule cADPR, which had $EC_{50}$ for 30-90 nM in a sea urchin homogenate (SUH) system (***28***). Its deoxy analogue

2’-deoxy-A-cADPR (2’-dA-cADPR, **4b**) was as potent as cADPR, with $EC_{50}$ for 58 nM in a SUH system. Deoxy and methoxy analogues, including 3’-deoxy-A-cADPR (3’-dA-cADPR, **4c**) and 2’-methoxy-A-cADPR (2’-OMe-A-cADPR, **4d**), shared similar agonistic activity, however, with reduced activity and functioning only at much higher concentration in a SUH system, having $EC_{50}$ for >5 μM and 26 μM, respectively (***30***,***31***). Contrarily, 3’-methoxy-A-cADPR (3’-OMe-A-cADPR, **4e**), a methoxy analogue showed antagonistic activity, having $IC_{50}$ for 4.8 μM in a SUH system (***30***). Similar activity was also observed on fluoro-substituted analogues, including 2’-deoxy-2’’-fluoro-A-cADPR (2’-dA-2’’-F-cADPR, **4f**), β-2’-fluoro-2’’,3’’-dideoxy-cADPR (β-FddA-cADPR, **4g**), and 3’-deoxy-3’’-fluoro-A-cADPR (3’-dA-3’’-F-cADPR, **4i**), with $EC_{50}$ for 470 nM, 25 μM, and 1.5 μM in SUH assay, respectively (***31***,***32***). To clarify the SAR, it was hypothesized that the alternation at the 2’- or 3’- hydroxy group was the key factor leads to reducing efficiency on agonistic activity or even leads to antagonists, though further conformation studies are still required (***29***,***33***). 8-substitued cADPR analogues, including 8-amino-cADPR (8-$NH_2$-cADPR, **4s**) and 8-bromo-cADPR (8-Br-cADPR, **4q**), were found to all be antagonists, having $IC_{50}$ in a SUH system for 970 nM and 105 nM, respectively (***34***). While most 8-substituted cADPR shared antagonistic activity, this is not the case for cIDPR derivatives, such as 8-bromo-N1-cIDPR (8-Br-N1-cIDPR, **12b**). As another class of cADPR analogues, N1-cIDPR had been recently studied extensively. In a Jurkat T-cells (JTC) system, the addition of cIDPR led to a rapid release of $Ca^{2+}$ from the intracellular stores that previously loaded with calcium ions (***35***). The concentration-response relationships of cIDPR and cADPR were nearly identical, especially at 100 μM ( in JTC system) where the amount of $Ca^{2+}$ released by cIDPR was

indistinguishable from that induced by cADPR (***35***). One issue with cADPR and its analogues is that cADPR often undergoes hydrolysis, having a half-life of 24 hours at pH 2.0 at 37 °C (***36***), and has poor membrane permeability that prevents it from moving across cellular membranes via membrane channels. One exception, its deaza analogues, reveals significant enhancement on permeability and resistance to hydrolysis, such as the partial agonist 7-deaza-cADPR (**8a**), with an $EC_{50}$ for 90 nM (***23***). Moreover, cIDPR and its analogs shares the advantages to be resistance to hydrolysis. In contrast to other 8-substitued cADPR analogues, 8-Br-cIDPR appeared to be the first 8-substited agonist affecting $Ca^{2+}$ release and extracellular $Ca^{2+}$ entry (without the interaction with TRPM2) (***37***). In a microinjected JTC system, 8-Br-cIDPR revealed $EC_{50}$ for ~300 μM, and more importantly, 8-Br-cIDPR resulted in a membrane-permeant molecule (***37***). However, there has been not yet a report on conformational analysis on cIDPR and its analogues, thus emphasizing the importance on this particular study. For future studies, we plan to synthesize and evaluate 8-amino-cIDPR (8-$NH_2$-cIDPR, **12d**) and 8-azido-cIDPR (8-$N_3$-cIDPR, **12c**), nevertheless, the calcium ion releasing activity of these two analogues was still yet reported.

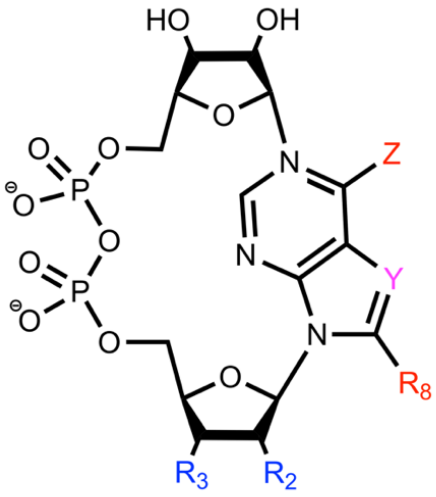


| | R3 | R2 | R8 | Y | Z |
|---|---|---|---|---|---|
| **4a** | OH | OH | H | N | $NH_2$ |
| **4b** | OH | H | H | N | $NH_2$ |
| **4c** | H | OH | H | N | $NH_2$ |
| **4d** | OH | $OCH_3$ | H | N | $NH_2$ |
| **4e** | $OCH_3$ | OH | H | N | $NH_2$ |
| **4f** | OH | F | H | N | $NH_2$ |
| **4g** | H | F | H | N | $NH_2$ |
| **4i** | F | OH | H | N | $NH_2$ |
| **4q** | OH | OH | Br | N | $NH_2$ |
| **4s** | OH | OH | $NH_2$ | N | $NH_2$ |
| **8a** | OH | OH | H | CH | $NH_2$ |
| **12b** | OH | OH | Br | N | O |
| **12a** | OH | OH | H | N | O |
| **12c** | OH | OH | $N_3$ | N | O |
| **12d** | OH | OH | $NH_2$ | N | O |

| | Agonist $EC_{50}$ | Antagonist $IC_{50}$ | Assay | Ref. |
|---|---|---|---|---|
| **4a** | 30-90 nM | | SUH | (***28***) |
| | <100 μM | | MIJTC | (***35***) |
| **4b** | 58 nM | | SUH | (***30***) |
| **4c** | >5 μM | | SUH | (***30***) |
| **4d** | 26 μM | | SUH | (***31***) |
| **4e** | | 4.8 μM | SUH | (***30***) |
| **4f** | 470 nM | | SUH | (***31***) |
| **4g** | 25 μM | | SUH | (***31***) |
| **4i** | 1.5 μM | | SUH | (***32***) |
| **4q** | | 970 nM | SUH | (***34***) |
| **4s** | 89 μM | 105 nM | SUH | (***34***) |
| **8a** | 90 nM (partial) | | SUH | (***38***) |
| **12b** | ~300 μM | | MIJTC | (***37***) |
| **12a** | ≈ $EC_{50}$ of **4a** | | JTC | (***35***) |
| **12c** | t.b.d. | t.b.d. | | (***35***) |
| **12d** | t.b.d. | t.b.d. | | (***35***) |

**Table 1.** Agonistic ($EC_{50}$) and antagonistic values ($IC_{50}$) for cADPR and cIDPR analogues. "SUH" stands for sea urchin egg homogenate. "JTC" stands for Jurkat T-cells. "MIJTC" stands for microinjected Jurkat T-cells. Note here calcium release induced by **12a** is almost indistinguishable from calcium release induced by **4a** in JTC. "t.b.d." stands for to be determined.

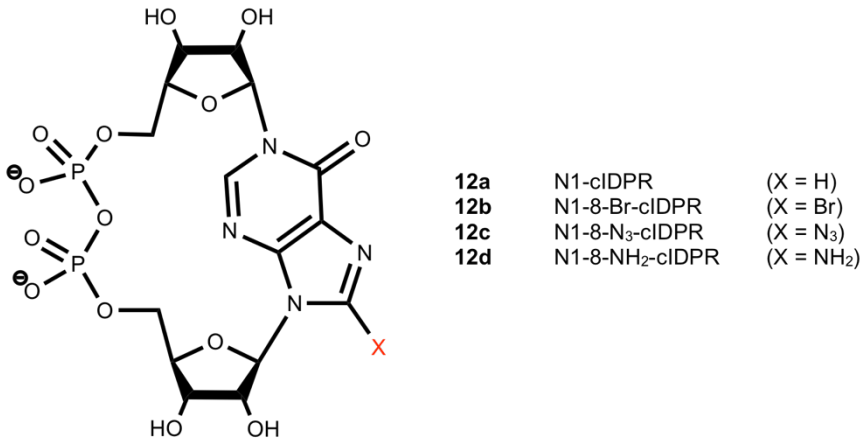


**Figure 4.** Chemical structure of cIDPR. The analogues of cIDPR discussed in this study varied at carbon-8 position, marked in red.

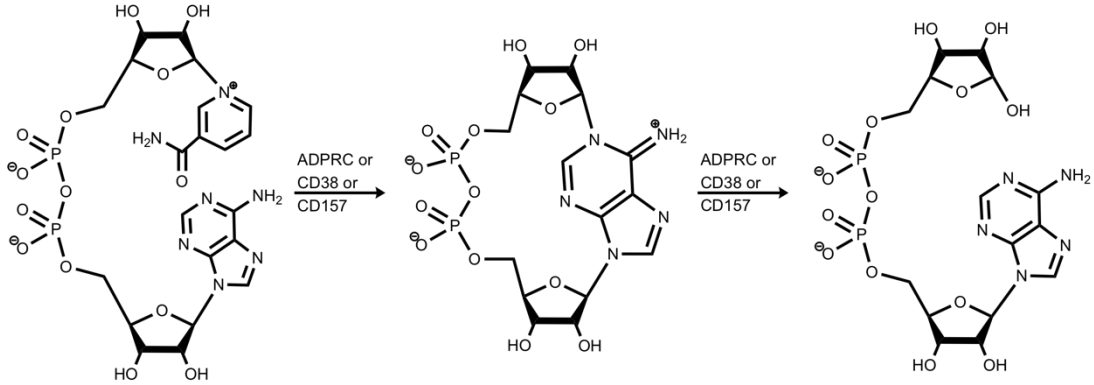


**Figure 5.** Enzymic synthesis of cADPR from $NAD^+$ and hydrolysis of cADPR to ADPR, catalyzed by ADP-ribosyl cyclase (ADP-RC). ADP-RC used in this study was acquired from the mollusk Aplysia *californica* as a soluble and commercially available enzyme. CD38 and CD157 are transmembrane glycoproteins having ADP-RC activity. cADPR can be further hydrolyzed to form ADPR in the presence of ADP-RC. cADPR alone can also undergo hydrolysis with a half-life of 24 hours at pH 2.0 at 37 °C *(**36**)*.

**Synthesis and Significance of cIDPR Analogues.** Recent studies on N1-cyclic inosine 5'-diphosophate ribose (N1-cIDPR, **12a**) (Figure 4), a mimic of cADPR analogues, reveals similar biological outcome compared to cADPR, but shows significant variation on their conformational landscapes (***18***), ability to permeate membranes (***37***), and metabolic stability (***35***). Traditionally, the optimistic synthesis for cADPR and its analogues follows the chemoenzymatic synthesis approach, in which an $NAD^+$ analogue

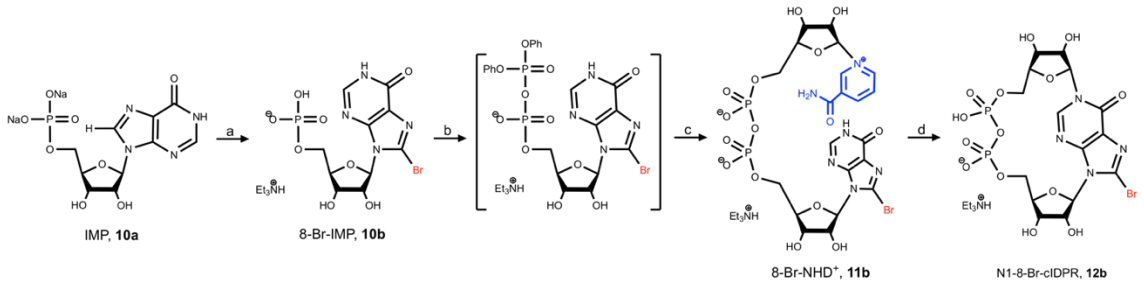


**Scheme 1.** Synthetic pathway of N1-8-Br-cIDPR. Reagents and conditions: (a) $Br_2$, 0.4 M acetate buffer pH 4.0, 2.5-3 days; (b) dry DMF, DPPC, TEA, 1.5-2 hr; (c) (i) dry DMF, $Ac_2NMN$, pyr, TEA, 1.5-2 hr (ii) $NH_3$, MeOH, 15 min; (d) HEPES buffer pH 7.01, ADPRC, 9.5-48 hr.

is cyclized to cADPR via the action of ADP-ribosyl cyclase (ADP-RC) (Figure 5), a relatively simple procedure, in contrast to the total chemical synthesis approach that involves multiple steps (***39***). In this study, we modified the synthetic procedure proposed by Potter et. al. (***35***), and advocate this scheme (**Error! Reference source not found.**) for the synthesis of 8-Br-cIDPR with greater conversion on intermediates, simplified procedure with three main steps, and better yield on final product. The requisite precursor for cIDPR synthesis, nicotinamide hypoxanthine 5'-dinucleotide ($NHD^+$, **11a**), is a substrate of ADP-RC, however, cyclization occurs at the N7 position of the cIDPR moiety rather than N1 due to its preference for adopting the anti-conformation, leading to the physiologically inactive messenger N7-cIDPR (Figure 6). In fact, cyclization catalyzed by ADP-RC were proceed via a common covalent intermediate. Once a covalent bond is formed from catalytic base of the cyclase to the substrate, the enzyme favors the syn orientated nucleobase to cleave the enzyme-substrate bond when aligning in a hairpin conformation, followed with cyclization of the substrate on the N1 position (***35***). Study revealed that a bulky substituent at C8 position on $NHD^+$, such as bromine, which gives the analogue nicotinamide 8-bromohypoxanthine 5'-dinucleotide (8-Br-$NHD^+$, **11b**), can adopt syn conformation on the nucleoside (details in Discussion) (***35***).

Reported by Potter et al.'s group (***35***), such intermediate can be recognized and cyclized at N1 position catalyzed by ADP-RC, forming 8-Br-N1-cIDPR. Our study for the synthesis of cIDPR improved from the original via our modified procedure, with greater conversion rate, better yield, and simplified ion exchange method for purification. Moreover, chemoenzymatic synthesis of cADPR and its analogues often undergo hydrolysis, either because of the short spontaneous half-life (***40***), or decyclization catalyzed by the enzyme, but cIDPR has the advantage to be more stable to hydrolysis over the synthetic cyclization. The unusual chemical stability of 8-Br-N1-cIDPR provides the possibility to synthesize other cIDPR analogues directly from its parent analogue via chemical synthesis approach (Scheme 2)., giving a distinct feature different from cADPR.

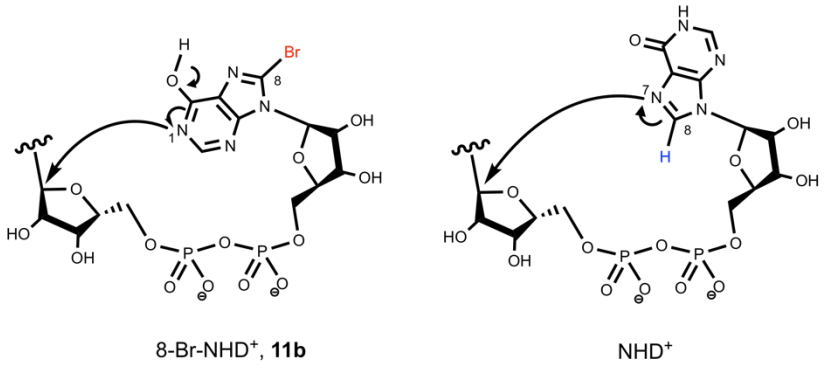


**Figure 6.** Schematic representation of enzymatic cyclization of $NHD^+$ and 8-Br-$NHD^+$ catalyzed by ADP-RC. In the case of 8-Br-$NHD^+$, a bulky substituent bromine at C8 position leads to syn conformation at the nucleobase of ADPR, and cyclization at N1 is thermodynamically and kinetically favored. In contrast, with nucleobase of ADPR at anti conformation, $NHD^+$ cyclized at N7, leading to biologically inactive molecule.

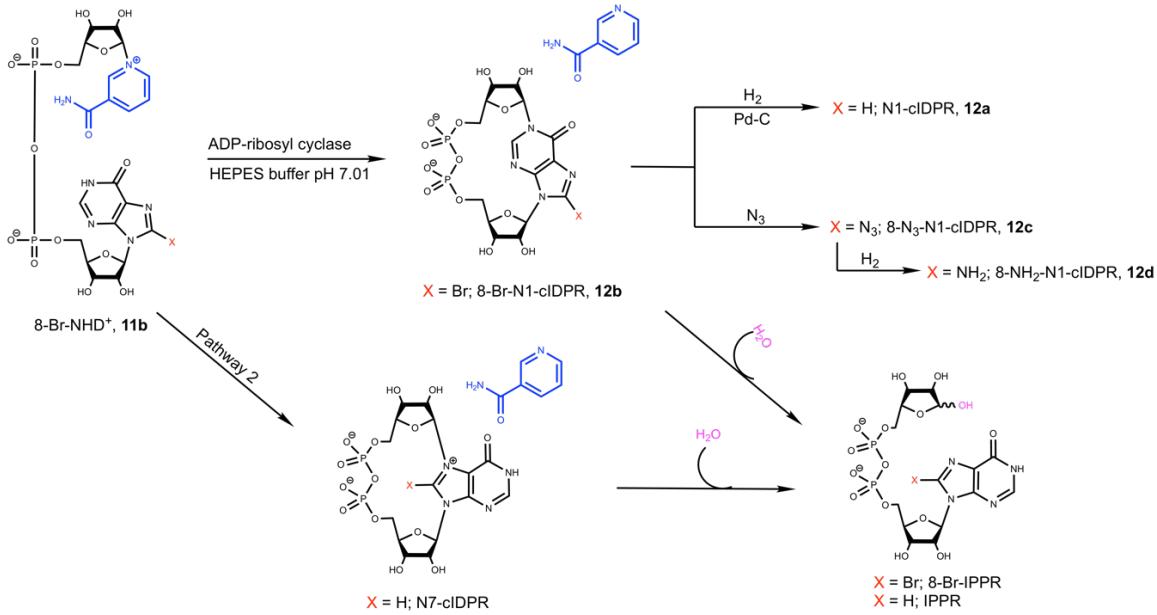


**Scheme 2.** Two chemoenzymatic pathways of cyclization driven by variable 8-substituted $NHD^+$ analogues. Pathway 1, 8-Br-$NHD^+$ undergoes cyclization catalyzed by ADPRC at N1 position, forming the signaling active N1-cIDPR analogues. Pathway 2, 8-H-$NHD^+$ undergoes cyclization at N7 position, forming the signaling inactive N7-cIDPR. Both pathways can be hydrolyzed into non-cyclic molecules catalyzed by ADPRC, though cIDPR analogues are more stable to hydrolysis than cADPR analogues under same condition.

**NMR spectroscopy and conformational analysis.** cADPR is a cyclic adenine nucleotide with linkage of pyrophosphate binding at 5' position on the two furanose rings, respectively, where most of the conformational variations occur. The conformational analysis of furanose can be approached by pseudorotation concept. Pseudorotation concept, first proposed by Kilpatrick et. al. in 1947 (***41***), has become the basis for the study of the conformation of five membraned rings. The geometry of the furanose ring can be analyzed by the endocyclic torsion angles in the rings, reflected in by the *J* coupling values acquired by solution NMR spectrometry. Requisite *J* coupling values normally can be extracted from a high resolution 1D $^1$H spectrum. In the case of cADPR and its analogues, overlapping signals were traditionally (***29***,***33***) isolated via 1D TOCSY, 1D NOESY, and phosphorus-decoupled NMR experiments to extract desired *J*

values from crowded regions. Unfortunately, this does not apply to signals of cIDPR analogues. Several of the signals in 8-Br-N1-cIDPR have extremely close chemical shift differences ($\Delta\delta \leq 8$ Hz), and are coupled, resulting in a non-first order ABC spin system in the $^{1}$H spectrum. A non-first order pattern cannot be analyzed by usual 1D selective NMR experiments, for instance, 1D TOCSY, but instead can only obtained by computational simulation. Shown in Figure 7a, the simulation spectra, an AB system was going from first order to non-first order pattern with decreasing $\Delta\nu/J$, and the line difference of the non-first order pattern no longer equals the coupling constant value. To solve this problem, we used the pure in-phase (PIP) heteronuclear correlation NMR experiment (PIP-HSQC), proposed by Parella et. al. (***42***). PIP-HSQC selected the protons on $^{13}$C satellites (Figure 7b), which are shifted +/- approximately 60 Hz from the proton signal. For example, in case of ethylbenzene (Figure 7d), aromatic protons are magnetically inequivalent, thus resulting in 'messy' signals. Shown in Figure 7c, on a 1D selective PIP-HSQC spectrum, proton signals are split into two 'satellite' signals by the 1-bond $^{13}$C-$^{1}$H coupling. When selected at C4 (Figure 7c), the left triplet gets more non-first order since it was moved closer to H3, while the right triplet gets cleaner first order pattern, which allows accurate measurement of coupling constants. $^{13}$C satellite allows easy observation and precise measurement of coupling constants of the non-first order signals, which now adopt first order pattern (details in Discussion). The proposed PIP-HSQC utilized a z-filter to suppress unwanted homo- and heteronuclear anti-phase contributions contributing to distorted multiplets and make *J* values extractable from such spectra in precise. In addition, our previous studies (***29***,***33***) had showed that, in cADPR and many of its analogues, both A rings and R rings (Figure 1) often favor the 'south'

conformation, but in 8-Br-N1-cIDPR, the A-ring favored the 'south' conformation but the R-ring favored the 'north' conformation.. Such phenomena were first observed in 2005 (***35***), but a complete conformational analysis and thermodynamic study was not undertaken and is discussed in this thesis.

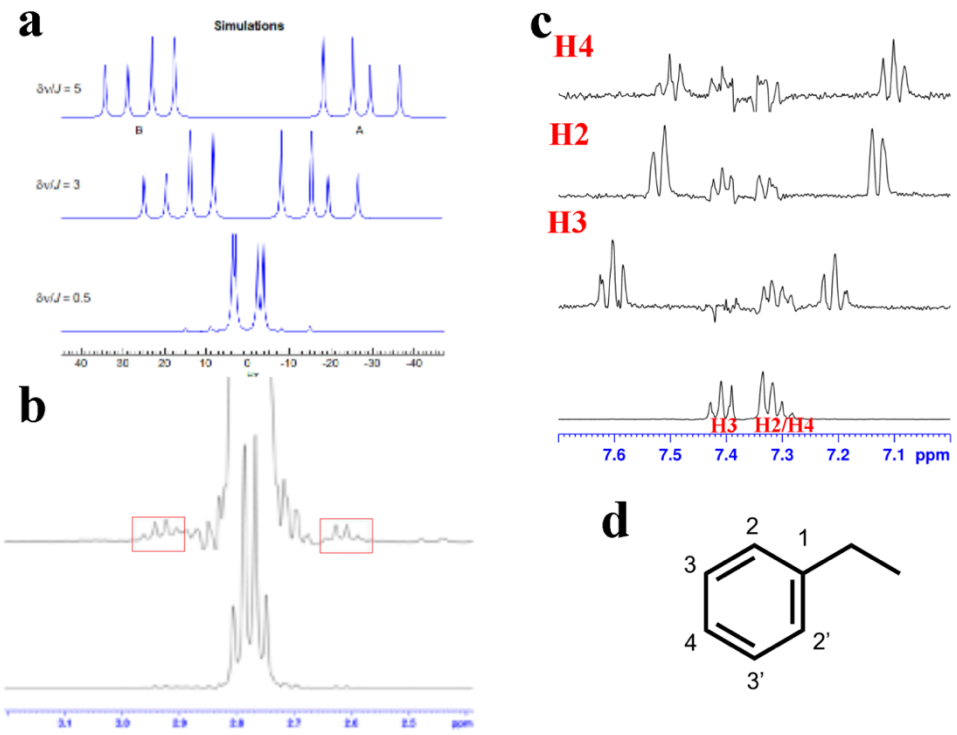


**Figure 7.** (a) Simulation spectra show the distortion as an AB system changes from first order ($\Delta\nu/J$ =5) to non-first order ($\Delta\nu/J$ =0.5). (b) The -CH2- in ethylbenzene satellites (boxed). (c) $^{1}$H spectrum and sel-PIPHSQC spectra of ethylbenzene. Selected at C4, the left satellite proton signal lost it first order pattern since it was moved closed to H3, while the right satellite remained first order. (d) Chemical structure of ethylbenzene.

## RESULT AND DISCUSSION

**Synthesis.** In this study, 8-Br-N1-cIDPR (**12b**) was prepared by the conversion of 8-Br-$NHD^+$ (**11b**) using ADP-ribosyl cyclase (ADP-RC), from *Aplysia californica,* a soluble and commercially available enzyme. The synthesis of **12b** followed a three-step chemoenzymatic approach consisting of: first, bromination of nucleotide IMP, selectively on C8 to give 8-Br IMP (**10a**), the requisite precursor that adopts syn conformation; second, activation of the 5'-phosphate of **10a** by forming a pyrophosphate bond, which was later attacked by NMN, giving **11b**, the requisite $NHD^+$ analog; finally, cyclization of **11b** catalyzed by Aplysia *californica* to yield the product **12b**. The overall reaction scheme of **12b** is shown in Scheme 3. As mentioned in the introduction, cIDPR analogs have the advantage of being more stable to hydrolysis. A syn conformation of this starting nucleotide was required for the ultimate N1-selective cyclization, and such conformation could be favored by a bulky substituent at C8 position on the nucleotide, such as bromine (***35***). Thus, a high yield of this initial step was ideal and preferred for the ultimate synthesis. Starting from commercially available hydrous disodium IMP, C8-selected bromination was performed following the method modified from Potter et. al. (***35***,***43***). In the literature, the reaction was carried in aq. $Na_2HPO_4$ (pH 6.2) buffer, stirred in dark for 5 days, and purified twice via a reversed phase (RP) column eluted by triethylammonium bicarbonate (TEAB) solution to yield 33% of the product. We modified this method, to a stirred solution of IMP dissolved in sodium acetate/acetic acid buffer (pH 4.0), added freshly prepared bromine water dropwise, and the resulting solution was stirred in dark for up to 2.5 days. This conversion of IMP into **10a** was monitored by HPLC and, as the literature claimed, this conversion cannot be driven to

completion (***35***). We observed the similar result that, after certain period of time, the product ceased to increase, or began to increase slowly, as monitored by RP HPLC. However, such separation could not be accomplished by a standard C18 column, as the two peaks merge or overlap. We then found Synergi fusion RP column, a polar embedded C18 phase that offers balanced polar and hydrophobic selectivity, provided clear separation between IMP and **10a** with significantly different retention times (7.3 min and 8.6 min, respectively), using only isocratic elution method (Figure 8). The conversion

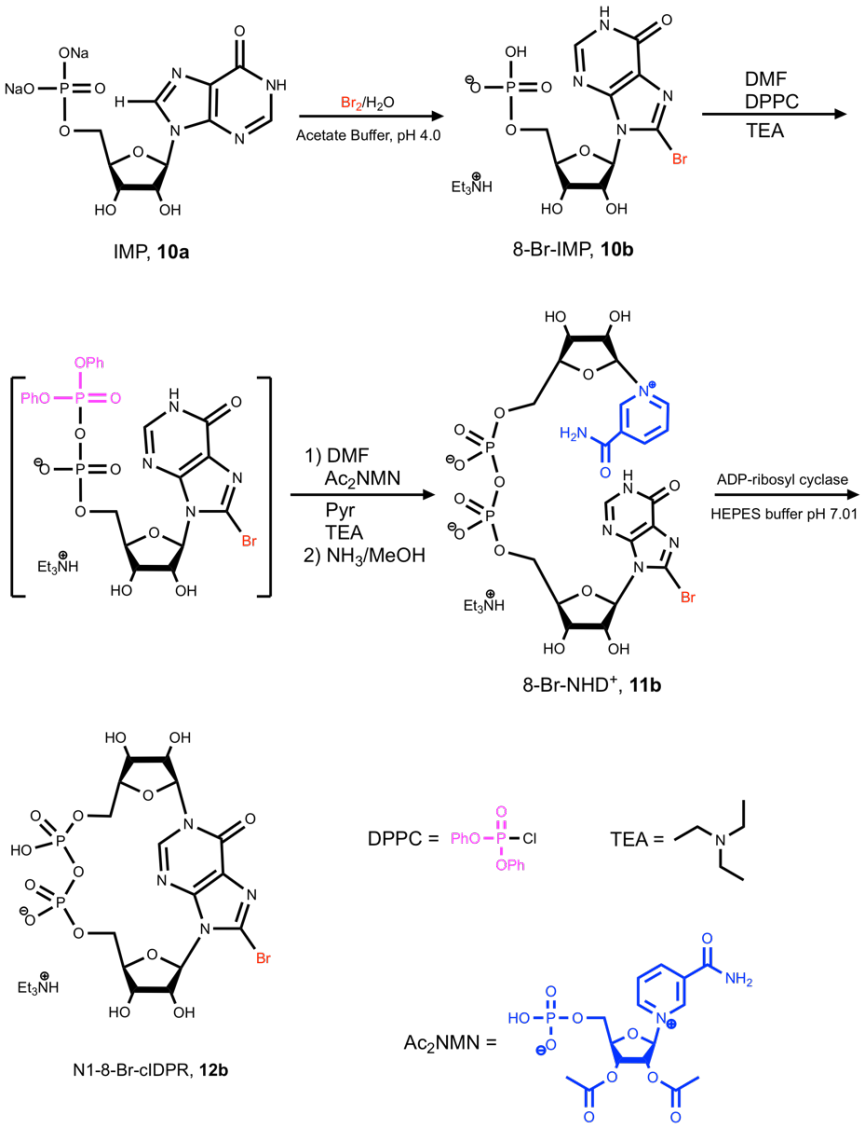


**Scheme 3.** Route for synthesis of 8-Br-N1-cIDPR.

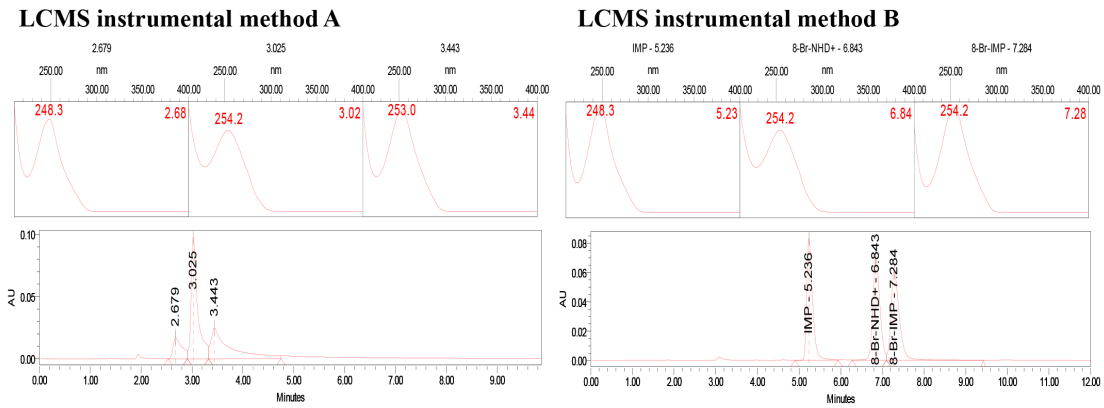


**LCMS instrumental method A:**

- column: **5 µm C18 150 x 4.6 mm**
- Mobile phase:
  - A: 5mM formic acid, pH 3.0
  - B: 90:10 5mM Formic acid : isopropanol
- Ratio: 80:20 A:B (isocratic)

**LCMS instrumental method B:**

- column: **4 µm Fusion-RP 150 x 4.6 mm**
- Mobile phase:
  - A: 5mM formic acid, pH 3.0
  - B: 90:10 5mM Formic acid : isopropanol
- Ratio: 85:15 A:B (isocratic)

**Figure 8.** LCMS instrumental method A utilized a 5 µm C18 column. LCMS instrumental method B utilized a 4 µm Fusion-RP column. The two instrumental methods followed the same elution method. Results revealed that method A provided poor separation, while method B gave baseline separation of IMP, **10a**, and **11b**.

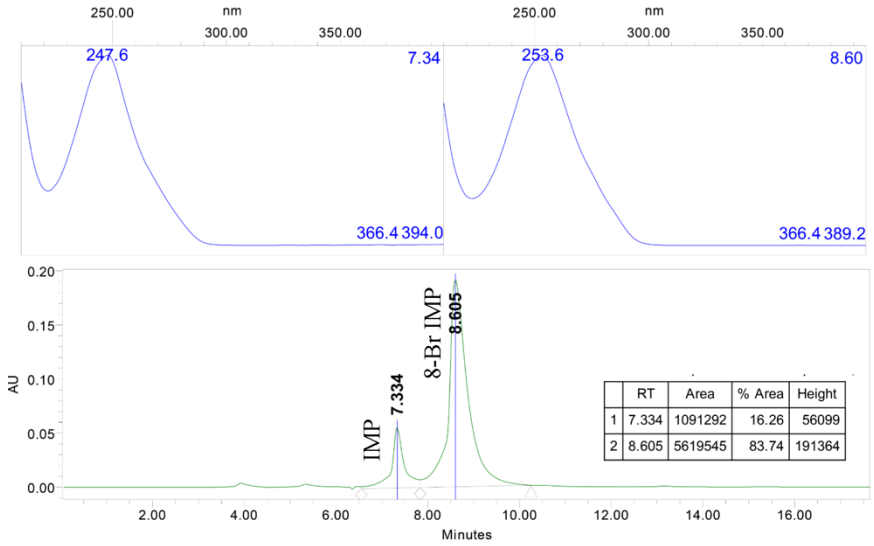


**Figure 9.** HPLC trace monitoring the bromination of IMP into 8-Br IMP, following the chromatographic method detailed in Experimental Procedure. IMP had $\lambda_{max}$ at 247.6 nm, and 8-Br IMP had $\lambda_{max}$ at 253.6 nm. Chromatograph provided celar baseline seporation between IMP ($R_t$ =7.334 min) and 8-Br IMP ($R_t$ =8.605 min).

rate of IMP into **10a** went consistently over 73%, and ultimately up to 84% (Figure 9). This high conversion rate matches the literature value reported by Ijzerman et. al., with their conversion rate of 85% (***43***). Note here acetate buffer was used instead of phosphate buffer, for the purpose of adopting an ion-exchange (IE) chromatographic system for purification instead of a RP chromatographic system used in the literature (***35***). The resulting solution was quenched by brief evaporation, and evaporated twice from water, to remove excess acetic acid from the buffer. By evaporating the excess acetic acid prior to pH adjustment and sample loading, the salt concentration was reduced, thus allowing higher loading. The separation utilized a column packed with Q Sepharose Fast Flow resins, a quaternary amine strong anion exchanger. We chose triethylammonium acetate (TEAA) to be the elute, as it was traditionally used in our previous synthesis of cADPR analogs (***29***,***33***). Eluted with a gradient of TEAA solution (pH 7.0), the early fractions were unreacted IMP, a few following fractions contained the mixture of both IMP and **10a**, and lastly pure **10a.** Purity was verified by RP HPLC analysis of individual fraction, as well as combined fractions (Figure 10). The identity of this product was also established by mass spectroscopy and NMR. The mass spectrum acquired by LC-MS showed clear signal for the introduction of bromine (m/z: 425, 427). Comparison of the $^{1}$H NMR chemical shift for A2' between IMP and **10a**, a significant downfield by +0.55 ppm was observed (Figure 11), as well as slight shifting of other signals. This phenomenon is caused by the syn conformation driven by the introduction of bromine atom due to its larger size, placing H2' edge on to the aromatic deshielding cone of the inosine base (***44***).

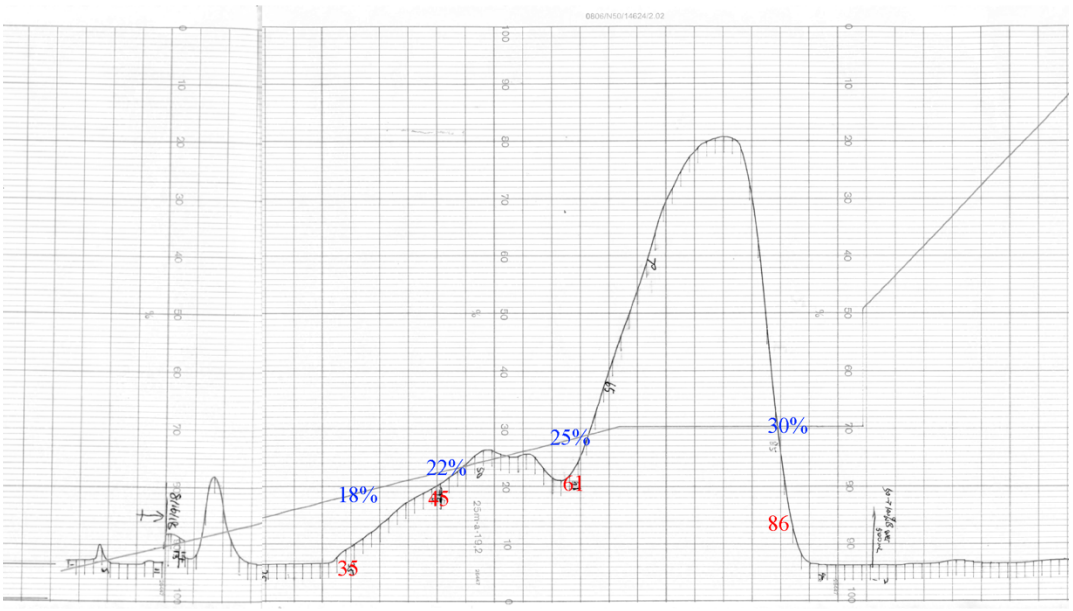


**Figure 10.** The chromatograph reveals the reaction mixture purified by GradiFrac through the preconditioned Q Sepharose Fast Flow column (acetate form) utilizing a gradient of 5-30% TEAA (1 M, pH 7.0) over 1000 mL. Early frations 35-45 (18-22% TEAA) were pure IMP that were not converted. Fraction 61-86 (25-30% TEAA) were pure 8-Br IMP, as verified by HPLC analysis. These fractions were combined and evaporated.

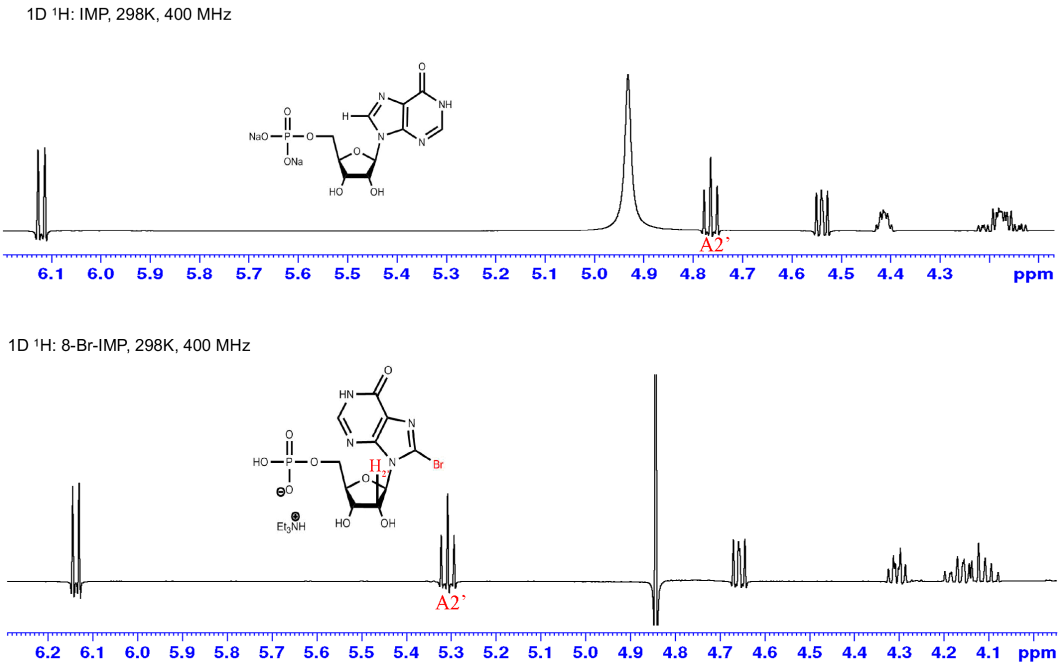


**Figure 11.** Comparison of $^{1}H$ NMR spectra between IMP and 8-Br-IMP. H2' signal shifts downfield by +0.55 ppm, a consequence of the syn conformation induced by the addition of bromine atom at C8. .

A challenge worth mentioning here is that the excess counterion TEAA could not be removed by simple evaporation and/or co-evaporation from other organic solvents, such as methanol. In our case, significant amount of exceed TEAA reminded after evaporating 5 times from water and 5 times from methanol, as indicated in the $^{1}$H NMR spectra. We attempted a precipitation method, by dissolving the pure **10a** sample in small amount of water and added the resulting solution into ice-cold rapidly stirred acetone dropwise. The resulting precipitate was verified to contain only 1-2 equiv. amount of TEAA, thus excess TEAA was removed successfully. Our recent study found TEAB could be more easily removed by evaporation, offering potential application that can be used in future studies, which will be discussed below.

The coupling step of **10a** joined the inosine analog to NMN via pyrophosphate bond formation to form NHD analog **11b**. We followed Michelson's procedure (***45***) in which diphenyl phosphoryl chloride (DPPC) was chosen to activate the 5'-phosphate on the initial nucleotide toward a nucleophilic attack, leading to the formation of a $P^1$-nucleoside-5'-$P^2$-diphenyl pyrophosphate (Scheme 2). The Michelson procedure was chosen for its less time consuming and simpler operation. The resulting pyrophosphate contained a weak base leaving group, thus could be displaced by another 5'-phosphate group of a second nucleotide from nucleophilic attack. In our case, we used commercially available nicotinamide mononucleotide (NMN) as the second nucleotide to form the ultimate $NHD^+$ analog. The 2'-hydroxy and 3'-hydroxy groups on NMN were first protected by forming 2'-3'-di-O-acetyl NMN ($Ac_2$NMN), to enhance solubility and minimize the exposure time of the weak NMN glycosidic bond to the reaction conditions (***33***). Pure **10a** was dried by evaporation from anhydrous DMF multiple times before use.

Anhydrous **10a** reacted with DPPC (1-1.5 hr), monitored by HPLC/LC-MS, generally to completion. Remarkably, in our case of activating **10a**, the starting nucleotide never completely disappeared, but often left with roughly 5%, relative to activated **10a**, as monitored by HPLC. We believe that small amount of moisture that often left to the reaction conditions, reacted with DPPC prior to the actual reaction between **10a** and DPPC. Upon the completion of this activation, solid anhydrous $Ac_2$NMN was then added directly into the reaction, which contained pyrophosphate activated **10a**, under the atmosphere of dry $N_2$ gas. This part of the reaction also optimistically went to completion, monitored by HPLC/LC-MS. Following the same ion-exchange chromatography as for **10a**, the purification of crude **11b** afforded in modest yield, however, $NAD^+$/$NHD^+$ synthesis suffered from low yield traditionally. When it came to desalting, we used the precipitation method, as discussed previously, to desalt the pure product **11b**. We also attempted an Oasis HLB desalting column to desalt the sample, but the results came out poorly, with best result having 4 equiv. of TEAA, as verified by $^1$H NMR. The poor performance could be that the large scale of the reaction exceeded the capacity of these desalting columns.

The enzymatic cyclization of **11b** into **12b** proceeded in quantitative yield using the *Aplysia californica* ADP-ribosyl cyclase (Figure 12). The main product was clearly **12b** after a 9.5 hr incubation period at room temperature, with small portion of linear 8-Br-IDPR, either converted directly from **11b**, or hydrolyzed from **12b** catalyzed by ADP-RC (Figure 12d). Signals of **12b** and 8-Br-IDPR were identified on a mass spectrum, by 17 mass unit difference for the additional hydroxyl group. Note here the incubation time could be longer than 9.5 hr but less than 48 hr, according to multiple trials we attempted

under the same reaction condition. The cyclization was typically run on a 50 μmol scale and diluted in 25 mM HEPES buffer (pH 7.03-7.21). It was crucial to have an overall diluted condition (~ 0.5 mM), because the side product nicotinamide is believed to be an inhibitor of the cyclization at the concentration of about 1 mM (***46***). The purification of **12b** followed the same ion-exchange chromatography as discussed above, using a column packed by Q Sepharose Fast Flow resins.

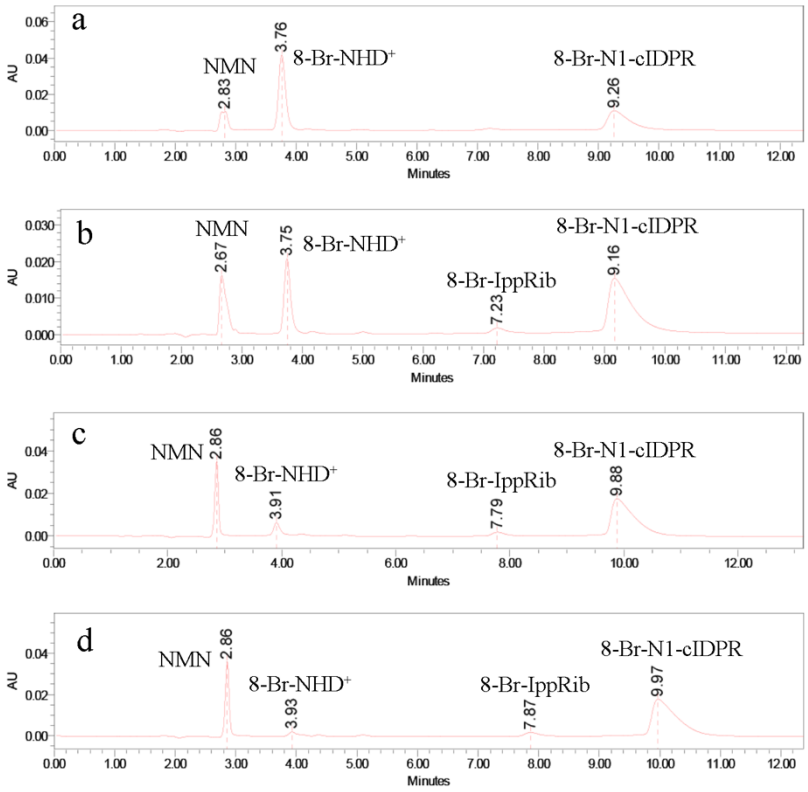


**Figure 12.** (a) HPLC chromatograph of cyclization of **11b** into **12b** incubated after 3 hr. (b) Same cyclization incubated after 6 hr. (c) Same cyclization incubated after 8 hr. (d) Same cyclization incubated after 9.5 hr. Note here the reaction went to almost completion, with small portion of 8-Br-IppRib formed as side product. Reaction was operated at room temperature.

In an attempt to desalt the purified NHD product **12b** using simple evaporation, we used two other eluents, trimethylammonium acetate solution (TMAA, pH 7.0) and triethylammonium bicarbonate (TEAB, pH 7.5). Both eluates were observed to be

removed by multiple evaporation from water and organic reagents. Comparing our precipitation method and evaporation method of TMAA/TEAB, both methods showed similar modest yield in the case of **12b**. In contrast, then same eluate TMAA could not be removed in the synthesis of **11b**. The resulting pure **12b** was found to be N1 selective as verified by HMBC experiment (discussed below). The di-/mono-triethylammonium salt **12b** showed broad lines in its proton spectrum, thus the sample was cation exchanged through column packed by SP Sepharose Fast Flow resins, a strong cation exchanger, to yield the disodium salt **12b**, used to prepare the NMR sample.

The proposed synthesis procedure of the other cIDPR analogs, N1-cIDPR (**12a**), 8-azido-cIDPR (8-$N_3$-cIDPR, **12c**), and amino-cIDPR (8-$NH_2$-cIDPR, **12d**), though have not attempted, are shown in Scheme 4, Scheme 5, Scheme 6, respectively, as reference.

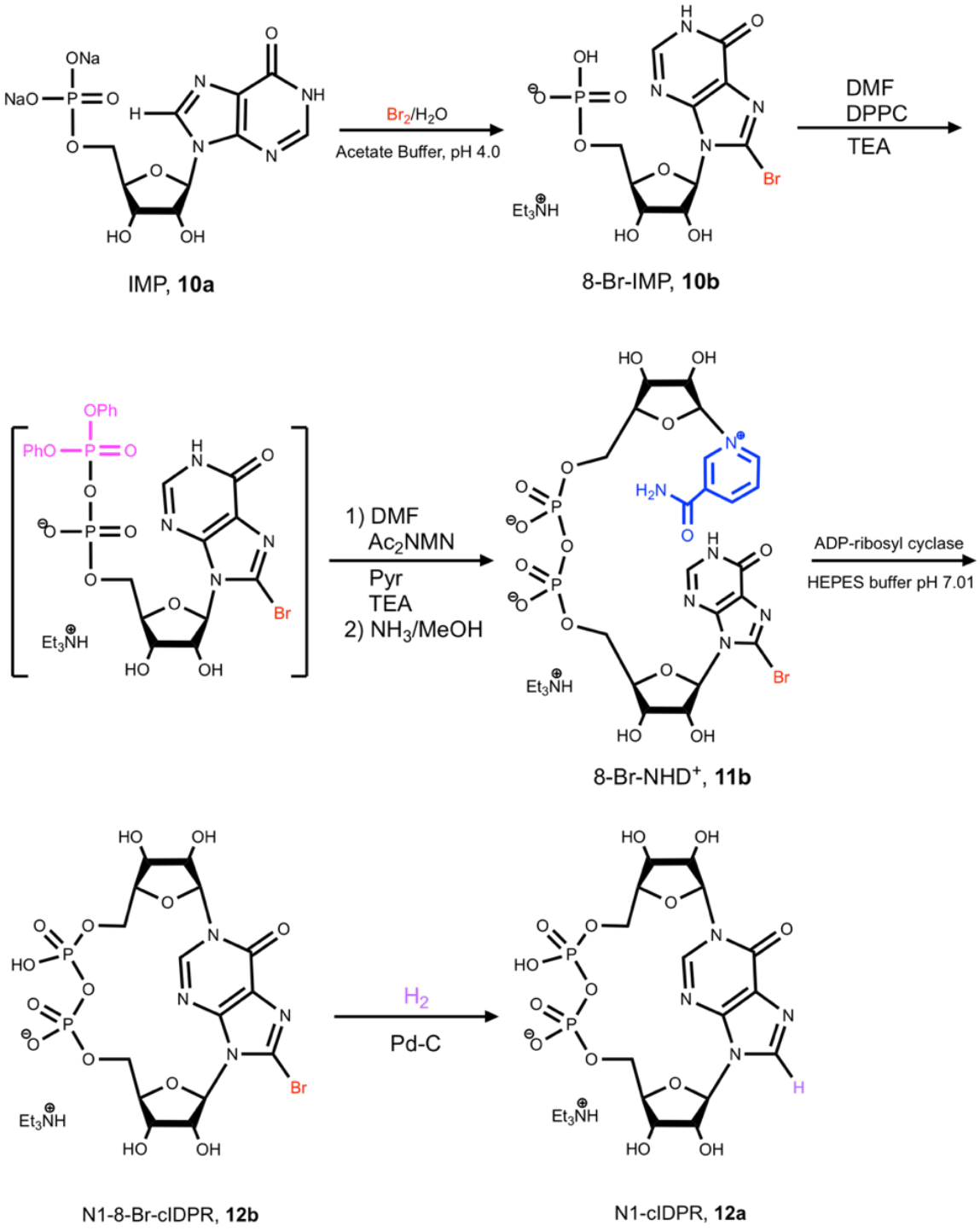


**Scheme 4.** Route for synthesis of N1-cIDPR.

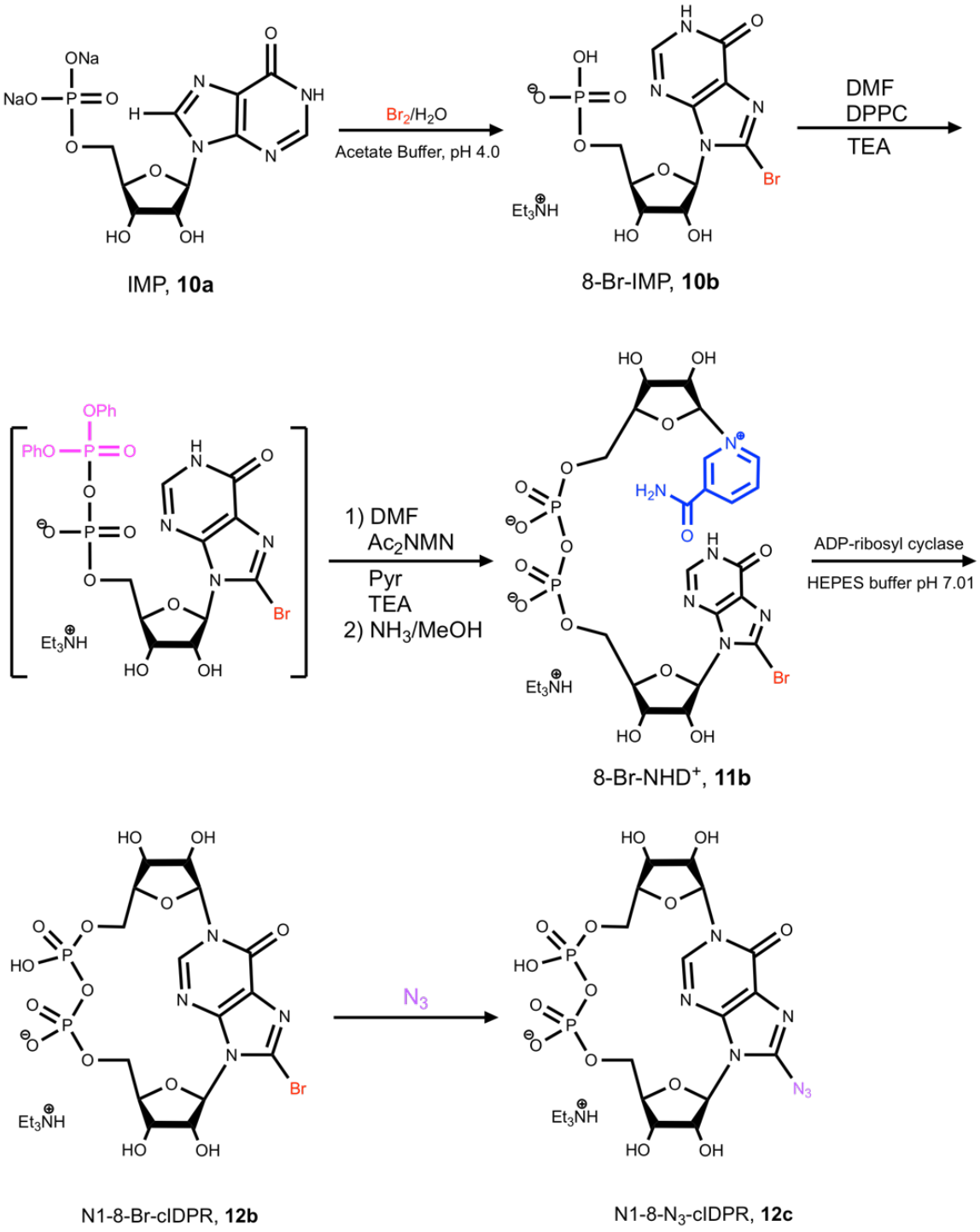


**Scheme 5.** Route for synthesis of 8-$N_3$-cIDPR.

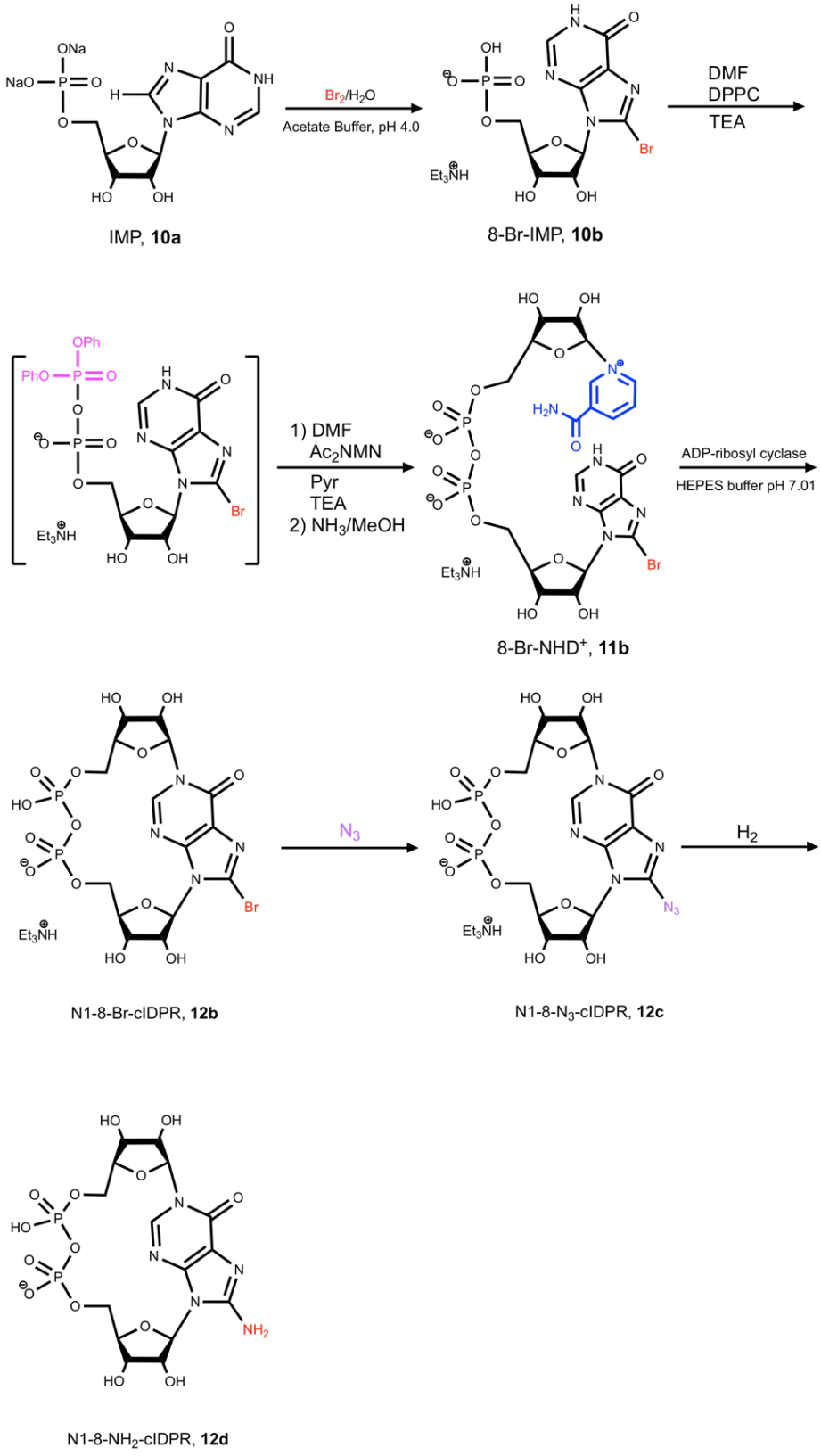


**Scheme 6.** Route for synthesis of 8-$NH_2$-cIDPR.

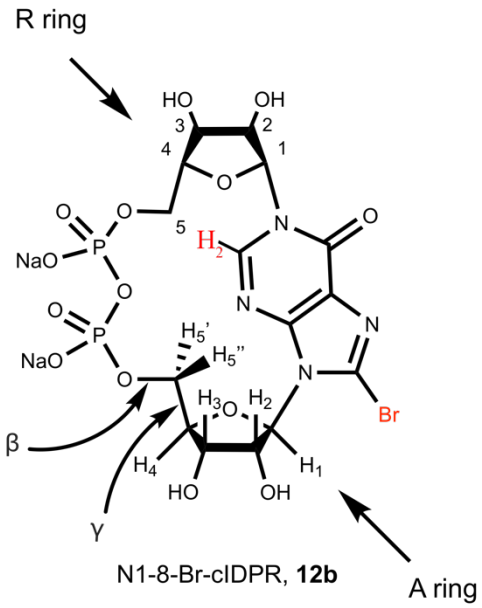


**Figure 13.** Chemical structure of 8-Br-N1-cIDPR, with atoms of furanose rings labeled.

**NMR spectroscopy and conformational analysis.** The NMR sample was prepared from the disodium salt of **12b** dissolved in $D_2O$, with TMSP added as the internal standard. In our experience, disodium salts provided better resolution compared with triethylammonium salt. The solid sample of **12b** was evaporated from $D_2O$ multiple times, to minimize the water signal that interferes with the signals of furanose rings. The HMBC spectrum of **12b** showed cross-peaks resulting from three bond coupling of the only heteroaromatic proton (8.85 ppm) binding at C2 of hypoxanthine to C1' (94.74 ppm) of the R-ring, and C4 of hypoxanthine (152.1 ppm) to both H2 (8.85 ppm) and H1' (6.14 ppm) of the A-ring. These analytical results strongly indicated that the bond was formed between C1' of the R-ring and N1 of the hypoxanthine ring, verifying the N1-selective cyclization. The variable temperature experiments were collected at 277K, 298K, 318K, 338K, and 358K. The temperature range covered slightly above the freezing point of $D_2O$, and below the boiling point of it. Note here, **12b** is hydrolytically

stable and decomposed at very slow rate even at high temperature, unlike cADPR analogs previously studied by our group (***33***). Figure 14 shows the $^{1}$H NMR spectra of **12b** over its temperature range, and it is clear that the chemical shift of $^{1}$H signals of **12b** changed slightly over the temperature range. In this study, the conformational analysis using PSEUROT requires us to extract accurate first order $^{1}$H-$^{1}$H coupling constants of the various three-bond spin vicinal systems. First order multiplets on a $^{1}$H spectrum can directly yield coupling constants within the accuracy of the digital resolution of the spectrum (collected in 0.12 Hz/pt; processed in 0.06-0.12 Hz/pt). The essential coupling values needed to study the conformations and phosphate backbone are, A-ring $J_{1'2'}$ and R-ring $J_{1'2'}$, A-ring $J_{2'3'}$, $J_{3'4'}$ and R-ring $J_{2'3'}$, $J_{3'4'}$, A-ring $J_{4'5'}$, $J_{4'5''}$, $J_{5'5''}$, $J_{5'P}$, $J_{5''P}$ and R-ring $J_{4'5'}$, $J_{4'5''}$, $J_{5'5''}$, $J_{5'P}$, $J_{5''P}$ (Figure 13). These coupling constants helped to define the conformational landscape of the two furanose rings, as well as the conformation about C5'-O5' (β-bond) and C4'-C5' (γ-bond). In general, $J_{1'2'}$, $J_{2'3'}$, $J_{3'4'}$ can be extracted from H1' and H3' signals of a $^{1}$H spectrum, with exception that signals might overlap with water signal at certain temperature. The splitting patterns of $^{1}$H signals of **12b** are summarized in Table 2, in comparison with splitting patterns of cADPR and 8-Br-N1-cADPR. It is worthwhile to point out some signals of the R-ring of **12b**, for instance, R1' appeared as singlet, an indication of north-oriented conformation. The A2' signal was less ideal to extract $J_{2'3'}$ because of its appearance as a triplet, due to the near equivalence of $J_{1'2'}$ and $J_{2'3'}$ in the A-ring. Likewise, the highly split A4' signal, which couples to A3', A5'/5'', sometimes, even to phosphorus, is a poor choice. H5'/H5'' naturally appeared to be a doublet of triplets (dt), impacted by 5'-5'' coupling and the near equivalence of $J_{4'5'/4'5''}$ and $J_{5'P/5''P}$. A exception is H5'' of the A-ring, which usually appeared to be a

doublet of doublet of doublet (ddd), due to the large coupling constant $A_{4'5''}$.The combination of routine $^{1}H$ NMR and phosphorus-decoupled $^{1}H$ ($^{1}H\{^{31}P\}$) NMR was used to extract the coupling constant of H5'/5'' to P5' by subtracting $\Sigma(J_{4'5'/4'5''} + J_{5'5''})$ from $\Sigma(J_{4'5'/4'5''} + J_{5'5''} + J_{5'P/5''P})$, as shown in Figure 15. The difference between the first and last peak of a first-order signal equals the sum of each individual coupling constant under the same proton signal. Additional information was also acquired using 1D TOSCY and/or 1D NOESY for, first, assigning the proton signals on the furanose ring, second, extracting coupling constants at the temperature when signals start to overlap, and third, assigning H5' and H5'', as interacting with H3' via 1D NOESY.

| | cADPR | 8-Br-N1-cADPR | 8-Br-N1-cIDPR (**12b**) |
|---|---|---|---|
| A1' | d | d | d |
| A2' | t | t | t |
| A3' | dd | dd | dd |
| A4' | dt | dt | dt |
| A5' | dt | dt | dt |
| A5'' | ddd | ddd | ddd |
| R1' | d | d | s |
| R2' | t | t | non-1$^{st}$ order |
| R3' | dd | dd | non-1$^{st}$ order |
| R4' | m | m | non-1$^{st}$ order |
| R5' | dt | dt | dd |
| R5'' | dt | dt | dd |

**Table 2.** Observed splitting patterns of cADPR, 8-Br-N1-cADPR, and **12b**. Patterns highlighted are uncommon splitting patterns of **12b** in contrast to cADPR analogs, including: singlet of R1', non-1$^{st}$ order patterns of R2', R3', and R4', and dd of R5' and R5''.

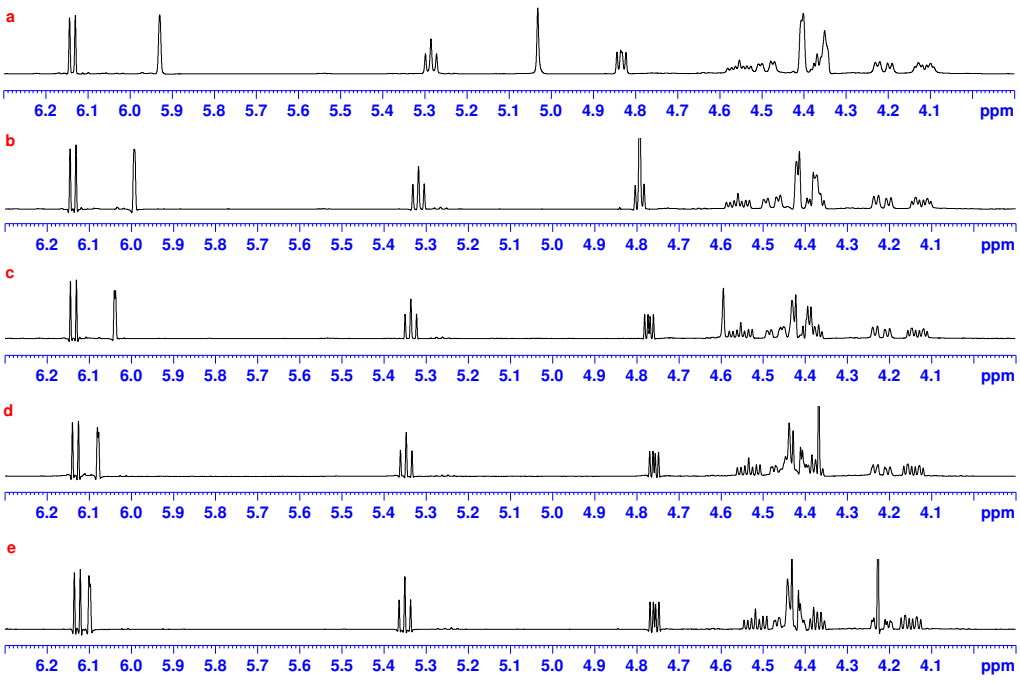


**Figure 14.** $^{1}$H spectra of **12b** at variable temperatures, including (a) 277K, (b) 298K, (c) 318K, (d) 338K, and (e) 353K. Note here the $^{1}$H signals do not experience much change in chemical shift over variable temperatures.

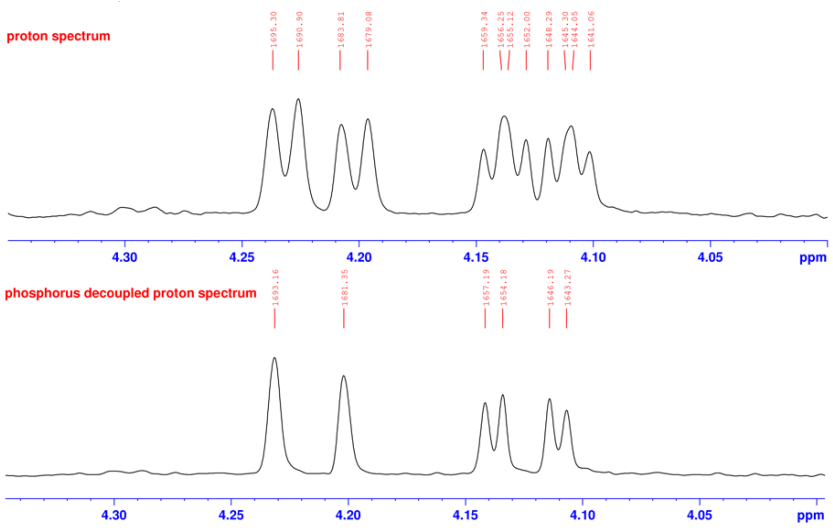


**Figure 15.** The top spectrum is the $^{1}$H spectrum of 8-Br-N1-cIDPR, with the downfield signal of R5'' (dd), and the upfield signal of A5' (dt). The bottom spectrum is the phosphorus decoupled $^{1}$H spectrum of the same compound, with the phosphorus decoupled downfield doublet and upfield doublet-doublet.

One of the notable features of **12b**, in contrast to cADPR, as our group studied previously (***29***,***33***,***47***), was the unique north-oriented R-ring. Distinctively, R1' appeared to be singlet on $^{1}$H spectrum (5.97 ppm, 298K), observed on both 400 MHz and 800 MHz NMR spectrometers, due to the small coupling between R-H1' and R-H2' in the north conformation (Figure 16). To the best of our knowledge, we are the first to comment on the significance of the R1' singlet. The second feature was the true higher order coupling patterns revealed by the R-ring signals of **12b**, including R2', R3', and R4', within the same crowed region. In a first-order spin system, the chemical shift difference in hertz ($\Delta\nu$) is larger compared to the coupling constants between the corresponding protons. Generally, systems are considered to be first order, when $\Delta\nu/J$ is greater than 8 or so (***48***). In a non-first order system, extra lines appear along the signal, and the signal cannot be analyzed by first order methods because the line separation no longer equals the coupling constant. R-ring R2', R3', and R4' protons of **12b** appeared on a $^{1}$H spectrum within a narrow region, within roughly 18 Hz apart each other at maximum. Traditionally we used 1D-TOSCY to extract coupling constants from crowed regions, but it did not apply in this case due to: (1) extreme small coupling constant between R1' and R2' that leads to poor TOCSY transfer when radiating on R1', (2) overlapping and merging of R2', R3', and R4', preventing selectable irradiation, and (3) small coupling of R4' and R5'/5'' resulting in poor TOCSY transfer when radiating either R5' signal using 1D TOSCY. Once an estimate of $J_{R2'R3'}$ and $J_{R3'R4'}$ was obtained via PIP-HSQC, the coupling constants of **12b** were extracted and further refined by DAISY simulation, as stated in Table 3.

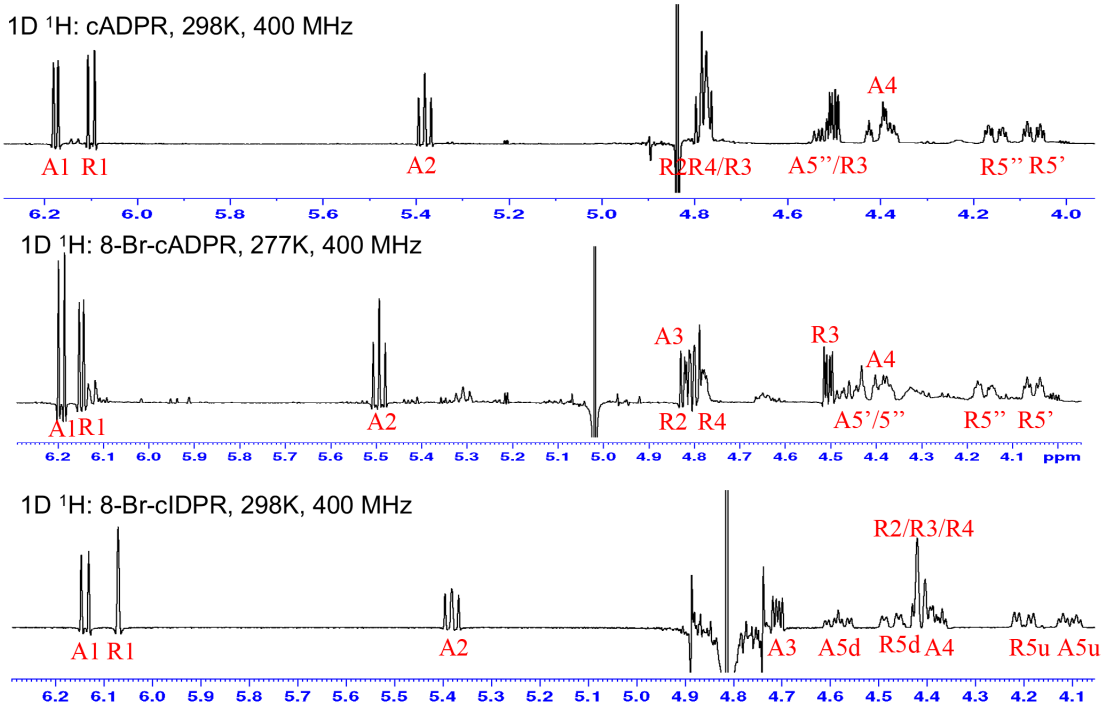


**Figure 16.** Comparison of $^{1}$H spectra of cADPR, 8-Br-N1-cADPR, and **12b**. Note here R1’ of cADPR and 8-Br-N1-cADPR appeared to be doublet, while R1 of **12b** revealed to be singlet, an indication of north-oriented conformation of R-ring. The bottom spectrum shows the overlapping of R2’, R3’, and R4’ (4.40-4.44 ppm), within the range of 18 Hz.

The input observed coupling constants before simulation, of $J_{1'2'}$, $J_{2'3'}$, and $J_{3'4'}$ in the A-ring, were generally extracted from the 1D $^{1}$H spectrum at its corresponding temperature, with routinely applied resolution enhancement. $J_{4'5'/5''}$, $J_{5'/5''P}$, and $J_{5'5''}$ in A-ring were applied with the same resolution enhancement, and calculated via the equation discussed above, from the combination of routine $^{1}$H NMR and $^{1}$H $\{^{31}P\}$ NMR. R-ring $J_{1'2'}$ was obtained with more aggressive processing of resolution enhancement. $J_{4'5'/5''}$, $J_{5'/5''P}$, and $J_{5'5''}$ of the R-ring were extracted with the same method as the A-ring. The non-first order signals of the R-ring, $J_{2'3'}$ and $J_{3'4'}$ were extracted from the slice of a 2D PIP-HSQC spectrum at the corresponding R-C3’.

| Coupling Constants of 8-Br cIDPR furose Ring via DAISY | | | | | | | | | |
|---|---|---|---|---|---|---|---|---|---|
| A ring | T (K) | J1'2' | J2'3' | J3'4' | J4'5' | J4'5" | J5'5" | J5'P | J5"P |
| | 277 | 5.44 | 5.16 | 3.45 | 3.02 | 7.09 | 11.00 | 4.27 | 3.76 |
| | 298 | 5.61 | 5.18 | 3.29 | 3.06 | 7.27 | 11.07 | 4.29 | 3.62 |
| | 318 | 5.70 | 5.22 | 3.20 | 3.11 | 7.31 | 10.99 | 4.32 | 3.48 |
| | 338 | 5.66 | 5.25 | 3.14 | 3.26 | 7.19 | 10.94 | 4.30 | 3.58 |
| | 353 | 5.65 | 5.30 | 3.21 | 3.30 | 7.07 | 10.94 | 4.35 | 3.66 |
| | | | | | | | | | |
| R ring | T (K) | J1'2' | J2'3' | J3'4' | J4'5' | J4'5" | J5'5" | J5'P | J5"P |
| | 277 | 1.17 | 4.66 | 7.78 | 1.78 | 0.90 | 11.90 | 3.66 | 4.34 |
| | 298 | 1.38 | 4.57 | 7.49 | 1.47 | 1.24 | 11.89 | 3.88 | 4.56 |
| | 318 | 1.45 | 4.43 | 7.07 | 1.48 | 1.22 | 11.78 | 3.85 | 4.64 |
| | 338 | 1.49 | 4.65 | 7.28 | 1.60 | 1.75 | 12.05 | 3.67 | 4.61 |
| | 353 | 1.52 | 5.05 | 6.39 | 1.40 | 1.89 | 11.93 | 4.47 | 5.49 |

**Table 3.** Coupling constants for **12b** of A-ring and R-ring via DAISY simulation. In case of A-ring, *J*1'2', *J*2'3', and *J*3'4' were generally extracted from 1D TOSCY spectra. *J*4'5', *J*4'5'', and *J*5'5'' were extracted from phosphorus decoupled spectra. *J*5'P and *J*5''P were calculated by the subtraction described in the Discussion. In case of R-ring, *J*1'2' was extracted from 1D $^{1}$H spectrum, with resolution enhancement. *J*2'3' and *J*3'4' were extracted from carbon dimension slices of 2D PIP-HSQC spectra. *J*4'5', *J*4'5'', *J*5'5'', *J*5'P, and *J*5''P were extracted following the same method as the A-ring.

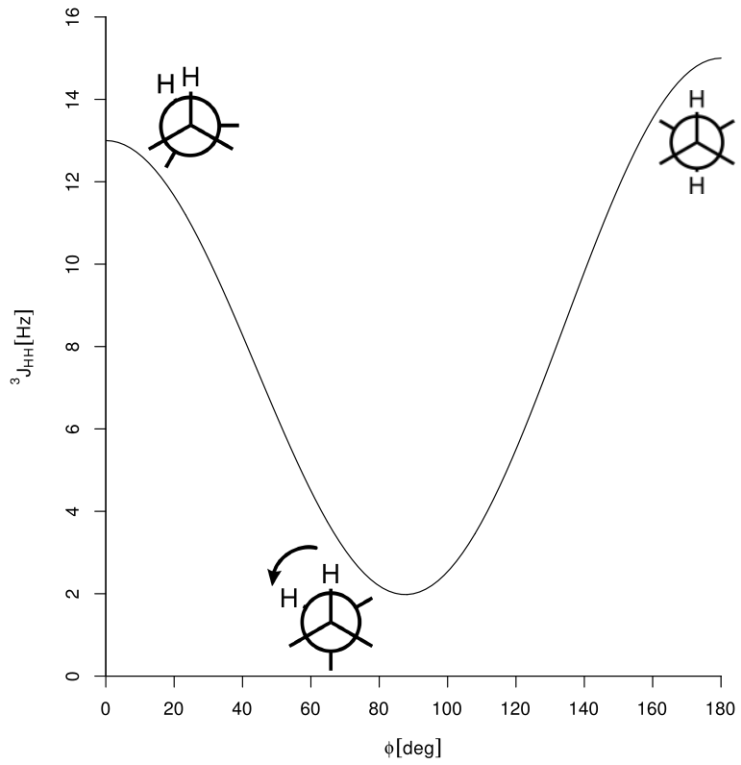


**Figure 17.** Karplus curve. Note the curve may shift down in certain cases, have the lowest $^3J_{HH}$ at nearly 0 Hz *(**49**)*.

**Conformational Analysis Using PSEUROT.** As a well-known concept to study the relative orientation of vicinal (H-C-C-H) protons, the Karplus equation indicates that the magnitude of a 3-bond coupling constant depends on the torsion angle (Φ) between the two planes. As shown in Figure 17 (***49***), a typical Karplus curve, the 3-bond coupling is the largest at Φ = 180°, an anti-conformation, and the smallest at Φ ≈ 90°, decreasing to nearly 0 Hz (note here in the figure the curve could shift down depending on the actual case). With the extracted coupling constants in hand, this leads to pseudorotation, the concept first developed by Kilpatrick el. al. in 1947 to investigate the conformation of five-membered ring (***47***), including the furanoses in this study. Like other cyclic structures, five-membered ring tends to avoid planarity and eclipsed conformations by adopting envelope conformations ($_2$E) or twist conformations ($^2$T$_3$), in which subscript

indicates atoms below the plane (exo) and superscript above the plane (endo), resulting in 20 possible conformations, with 10 in envelope forms and 10 in twist forms, as shown in Figure 18, the pseudorotation wheel of furanose ring (***50***,***51***). Five-membered rings are parameterized by two factors, a phase angle *P*, with north conformation $P_N = 0°$, and south conformation $P_S = 180°$, and the maximum puckering amplitude $\psi_m$, indicating the deviation of the ring from planarity. The observed coupling constants extracted from a $^1H$ spectrum is the weighted average of the respective coupling constants of two equilibrating conformations, the north conformation (P =0°, or C2'-exo-C3'-endo) and the south conformation (P =180°, or C2'-endo-C3'-exo), resulting in a two-state north/south equilibrium (Figure 18) (***47***). A quick and rough analysis of **12b**, the conformation can be obtained by noting that north-favored conformers will show a small $J_{1',2'}$ and a large $J_{3',4'}$, whereas south-favored conformers will show a large $J_{1',2'}$ and a small $J_{3',4'}$ (Figure 19). By this analysis, the A-ring of **12b** is clearly mostly south ($J_{1',2'}$ =5.61 Hz, $J_{3',4'}$ =3.29 Hz, 298K), while R-ring is mostly north ($J_{1',2'}$ =1.38 Hz, $J_{3',4'}$ =7.49 Hz, 298 K). The precise ratio of north to south (N/S) conformation can be predicted by the PSEUROT program (***52***), which uses the three-bond H-C-C-H coupling constants to predict phase angles P, for the north ($P_N$) and south ($P_S$) conformers, the puckering amplitude of north conformer ($\psi_m^N$) and south conformer ($\psi_m^S$), and the N/S ratio. The coupling constants listed in Table 3 are the input for version 6.3 of the PSEUROT program.

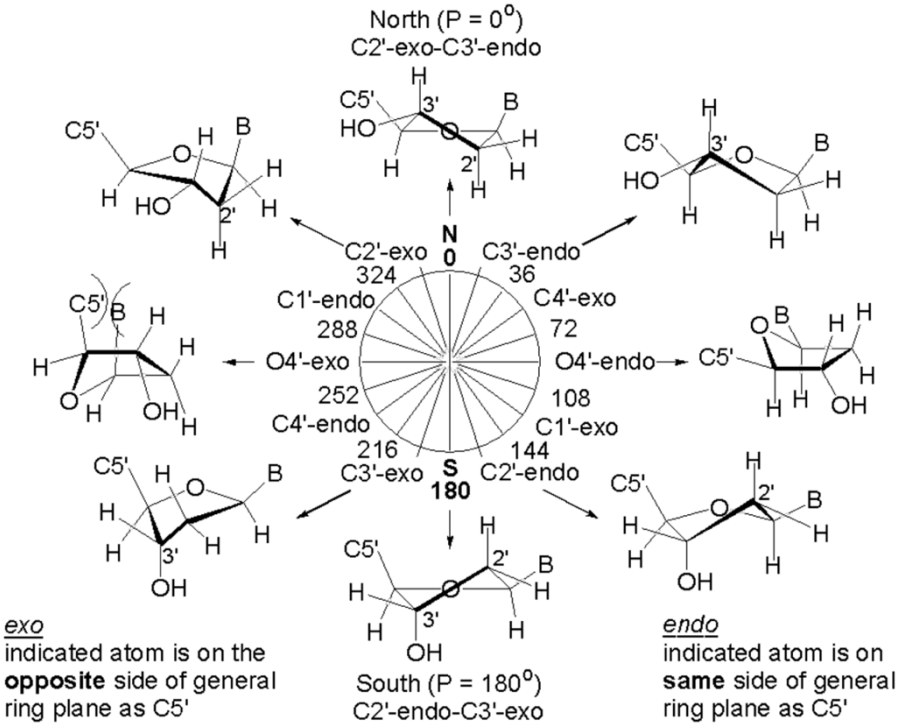


**Figure 18.** Pseudorotation wheel illustrates the geometries of five-membered furanose ring.

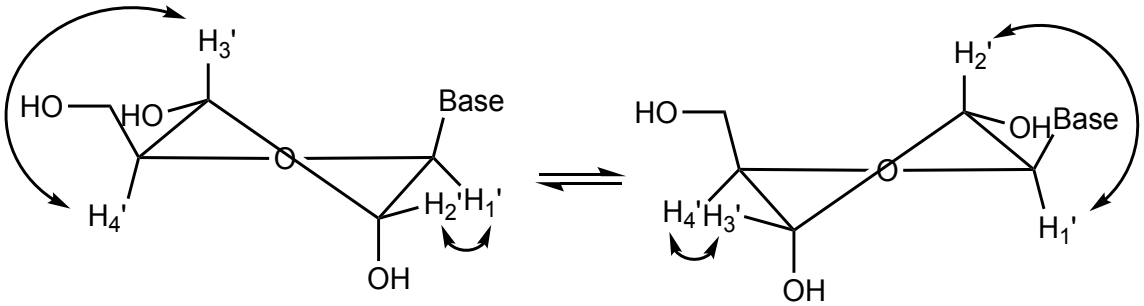


2'-exo-3'-endo (N)
$H_1$'-$C_1$'-$C_2$'-$H_2$', torsion angle ~ 90°
$H_3$'-$C_3$'-$C_4$'-$H_4$', torsion angle ~ 180°
small $J_{1'2'}$
large $J_{3'4'}$

2'-endo-3'-exo (S)
$H_1$'-$C_1$'-$C_2$'-$H_2$', torsion angle ~ 180°
$H_3$'-$C_3$'-$C_4$'-$H_4$', torsion angle ~ 90°
large $J_{1'2'}$
small $J_{3'4'}$

**Figure 19.** North and south conformations of a furanose ring. A small $J_{1'2'}$ and a large $J_{3'4'}$ indicates a north conformation. A large $J_{1'2'}$ and a small $J_{3'4'}$ indicates a south conformation.

In addition to the input of observed coupling constants, the user also provides initial guesses of $P_{N,}$ $P_S$, $\psi_m^N$, $\psi_m^S$, and the mole fractions of N/S equilibria. the 'A' and 'B' parameters are the set of parameters to correlate the endocyclic ring torsions to the exocyclic H-H torsions (***33***). These parameters are the "starting" point of the calculation and normally set based on typical values of the associated nucleotides. The program takes each initial guess conformer and uses the "A" and "B" parameters to create the exocyclic H-H torsion angles to calculate what the $^3J$ coupling for what that conformer should be. The $J_{cal}$ is then compared to the observed coupling values $J_{obs}$. The pseudorotation parameters of **12b**, in comparison with cADPR analogs, are listed in Table 4.

| | **A ring** | | | | **R ring** | | | |
|---|---|---|---|---|---|---|---|---|
| | $P_N$ | $\Phi_N$ | $P_S$ | $\Phi_S$ | $P_N$ | $\Phi_N$ | $P_S$ | $\Phi_S$ |
| **cADPR** | 22.5 | 35 | 177.1 | 31.5 | 340 | 40 | 215.8 | 36.6 |
| **8-Br cIDPR** | 3.4 | 32.7 | 169.2 | 30 | 23.5 | 44.9 | 233.2 | 23.4 |
| **2'dA cADPR** | 356.9 | 38 | 166.8 | 27 | 338.2 | 40 | 217 | 36.8 |
| **7-deaza cADPR** | 355.3 | 35 | 159.2 | 30.2 | 343.3 | 40 | 212 | 34.4 |
| **8-Br cADPR** | 20.3 | 35 | 173.7 | 28.8 | 337.2 | 40 | 215.4 | 36.2 |

**Table 4.** Pseudorotation parameters (degrees) of **12b** and cADPR analogs.

**Thermodynamic Parameters.** The thermodynamic parameters in this study are predicted by the thermo-equation $\Delta G° = \Delta H° - T\Delta S°$. The PSEUROT output data in Table 4 is the basis for a precise thermodynamic analysis using van't Hoff plots (Figure 20), calculating ΔH° and ΔS° values, listed in Table 5. Values of ΔH° and ΔS° inform as to whether the preferences for major conformers are enthalpy-driven or entropy-driven. A prediction can also be made as which conformer is the more disordered conformer: the conformer that increases with increasing temperature is the more disordered. In our previous work on cADPR and analogs, in case of the A-ring, it was always the minor

north (N) conformers that significantly increased with increasing temperature, indicating the more disordered conformer was the N conformer (***33***). Moreover, thermodynamic parameters at 298K listed in Table 5 shows the dominance of the enthalpy term over the temperature-entropy term in the A-ring of cADPR analogs, showing that the major south (S) conformer is favored enthalpically. The opposite trend was observed on the R-ring of cADPR analogs (***33***). The R-ring of cADPR analogs consistently shows a small ΔH° value and larger T ΔS° term, indicating the entropy-driven behavior of the R-ring. Interestingly, in contrast to cADPR analogs, 8-Br-N1-cIDPR (**12b**) shows the opposite thermodynamics (Figure 20, Table 5), despite its agonistic activity similar to cADPR. Quantitively van't Hoff equation predicts the conformer whose population increases with the increasing temperature is the more disordered conformer. The N/S equilibria of the A-ring of **12b** are characterized by the small value ΔH° and large positive value of TΔS° that favors S-conformers, and the N/S ratios were changed marginally with the increasing temperature, indicating that the N/S equilibria of the A-ring are indeed entropy-driven. This is the opposite of cADPR and its analog. Moreover, in case of R-ring, the population of south, the minor conformer, increases with increasing temperature, indicating that the S-conformer is the more disordered conformer. As shown in Figure 20b, the S-conformer is enthalpically disfavored with ΔH (N/S) of +1.71 kcal/mol, showing that the N conformer is favored by 1.71 kcal. The ΔH term of 1.71 kcal exceeds the TΔS term of 1.03 kcal, showing that the R-ring is enthalpically favored, which is also the opposite of cADPR and its analogs. The reasons of these differences between cADPR and **12b** regarding thermodynamics are unclear and will be the subject of future investigations.

8-Br-N1-cIDPR

| A ring | | | R ring | | |
|---|---|---|---|---|---|
| %N | %S | *K* | %N | %S | *K* |
| 35 | 65 | 1.86 | 79 | 21 | 0.27 |
| 33 | 67 | 2.03 | 76 | 24 | 0.32 |
| 31 | 69 | 2.23 | 72 | 28 | 0.39 |
| 31 | 69 | 2.23 | 73 | 27 | 0.37 |
| 32 | 68 | 2.13 | 63 | 27 | 0.59 |

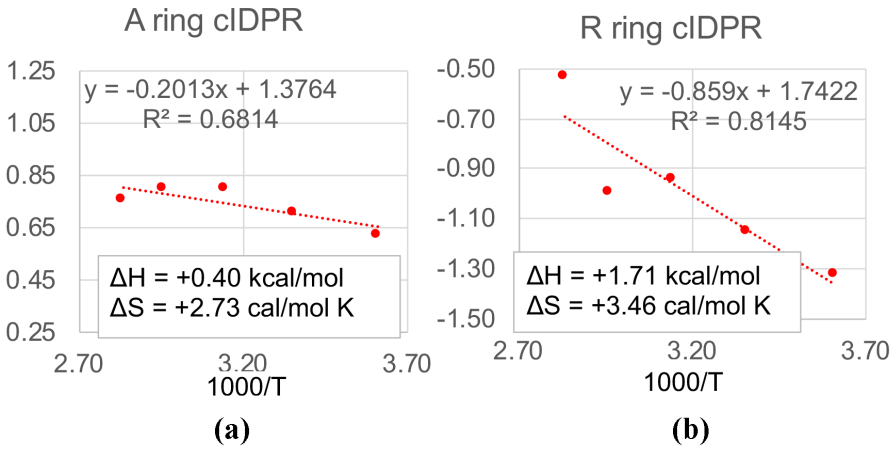


**Figure 20.** The van't Hoff plots (ln K as a function of 1000/T) of (a) A-ring and (b) R-ring of **12b**. The slope of each line is -ΔH°/R, and the y-intercept is ΔS°/R.

| | A ring | | | | R ring | | | |
|---|---|---|---|---|---|---|---|---|
| | Δ*H* | TΔ*S* | Δ*G* | N:S | Δ*H* | TΔ*S* | Δ*G* | N:S |
| cADPR | **-0.81** | -0.36 | -0.45 | 32:68 | 0.04 | **0.64** | -0.6 | 27:73 |
| 8-Br cIDPR | 0.40 | **0.82** | -0.42 | 33:67 | **1.71** | 1.03 | 0.68 | **67:33** |
| 2'dA cADPR | **-1.13** | -0.65 | -0.49 | 31:69 | -0.33 | **0.33** | -0.67 | 24:76 |
| 7-deaza cADPR | **-0.88** | -0.28 | -0.6 | 27:73 | -0.25 | **0.29** | -0.54 | 29:71 |
| 8-Br cADPR | **-0.24** | 0.15 | -0.39 | 34:66 | 0.1 | **0.73** | -0.63 | 26:74 |

**Table 5.** Thermodynamic parameters of cADPR analogs and **12b** for N/S equilibria. ΔG°, ΔH°, and TΔS° are in kcal/mol, ΔS° in cal/(mol K). Number in blue indicates the favored thermodynamic parameter. Number in red indicates the uncommon N/S equilibrium.

**First Order vs. Non-First Order Signal.** Naturally, analogs of nucleotides experience crowed region of the furanose ring over the range of 4.0-6.0 ppm, referenced by TMSP. Signals overlapping and merging on one another, revealing non-first order splitting pattern, makes it difficult to directly extract coupling constant from a normal 1D $^{1}H$ spectrum. Our team traditionally used 1D TOCSY and phosphorus-decoupled $^{1}H$ ($^{1}H\{^{31}P\}$) NMR experiments to extract *J* values from those crowed regions (***29***). There was always at least one signal of the furanose ring isolated from the others, coupling "well" and far away enough from the testing signal. For instance, in this study, we used 1D TOCSY to radiate at A2' that enhanced both A1' and A3', when the signal overlapped with water signal. As discussed above, such methods did not apply to the R-ring of **12b**, due to the appearance of certain key signals within the same crowed region, and small coupling between these signals and other corresponding signals. We attempted to radiate at R1', with the expectation to enhance R2' and ideally R3'. Starting with short spinlock mixing time (D9) at 15 ms, no signal was enhanced over 256 scans. With D9 at 60 ms, R2' signal started to appear from the crowed region, nonetheless, as broad singlet, showing no theoretically expected coupling with R3' (Figure 20) and an unanalyzable non-first order splitting pattern. In fact, even if there was a good TOCSY transfer from R1' to R2', R2' is still a non-first order signal, a broad singlet, whereas first-order rules, assuming coupling to R1' and R3', predict a doublet of doublets. A similar procedure was followed with 1D NOESY using various mixing time, resulting in the same observation of either no significant enhancement or unanalyzable pattern. We then redirected the approach by acquiring heteronuclear experiments instead, such as HSQC and HMBC, though knowing that the accurate extraction of *J* values from these spectra has been

problematic due to the characteristic mixed phases leading to difficult data analysis (***53***). In addition, the low natural abundance of $^{13}C$ adversely affected the overall signal-to-noise compared to proton experiments. In these experiments, a 2D HSQC spectrum was first acquired, followed by extracting a spectrum of desired proton from slicing the corresponding carbon dimension (Figure 22). Unsurprising, signals of R-ring sliced from a 2D HSQC spectrum appeared to be low resolution, distorted, and non-first order. The challenge here was, the similar magnitudes of the proton-proton coupling constants to small carbon-proton coupling can introduce unwanted effects in both splitting pattern and transfer efficiency, as evolving during the defocusing/refocusing periods (***42***). The closeness of targeting signals in chemical shift value also distort the proton signal even on a heteronuclear experiment. Parella el. al. proposed a modified HSQC pulse sequence, named as Pure-In-Phase (PIP) HSQC, based on *a conventional HSQC pulse train with an appended adiabatic z-filter applied just before a refocusing gradient perfect-echo element and acquisition* (***42***).

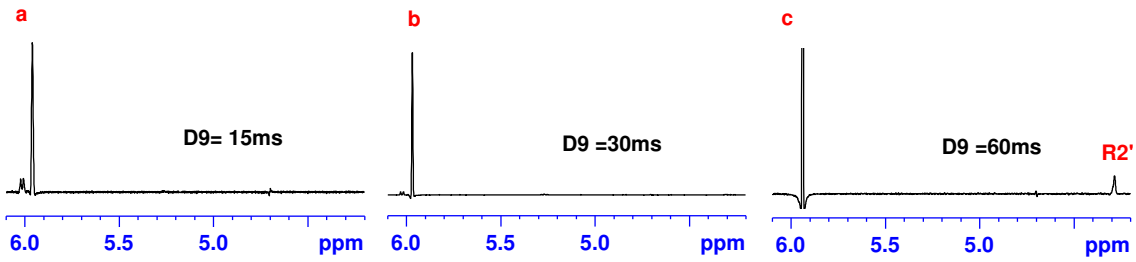


**Figure 21.** 1D selective TOSCY spectra of **12b** radiated at R1', including (a) D9 at 15 ms, (b) D9 at 30 ms, and (c) D9 at 60 ms. R2' started to appear starting from D9 at 60 ms.

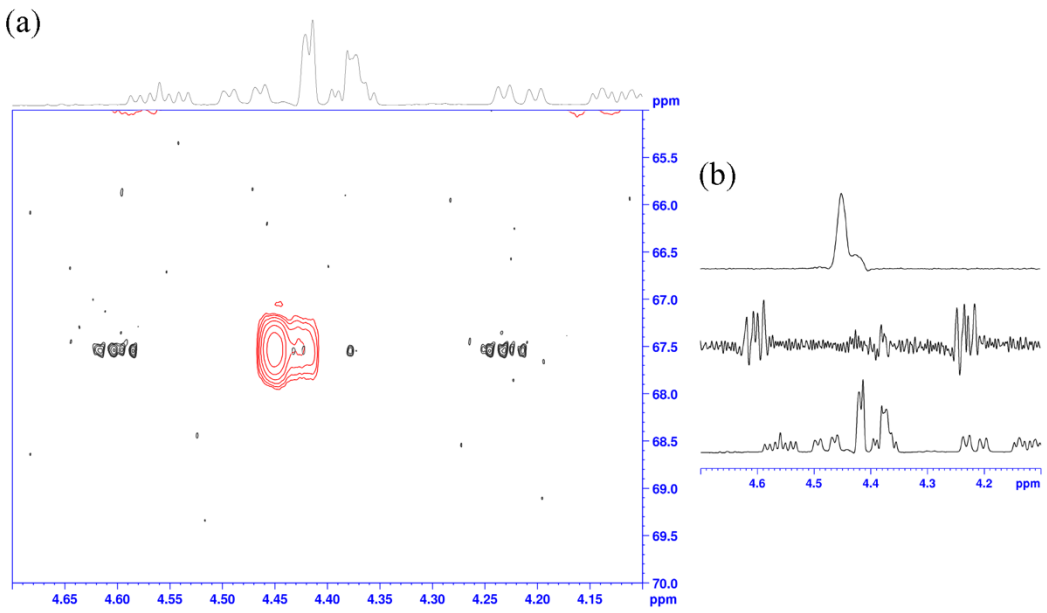


**Figure 22.** (a) 2D HSQC spectrum of **12b**. Cross peak in red was acquired via Bruker's hsqcedetgpsisp2.3. Two satellite cross peaks in black were acquired via PIP-HSQC. (b) Bottom spectrum is 1D $^{1}$H spectrum of **12b**. Middle spectrum is PIP-HSQC spectrum sliced at R3'. Top spectrum is HSQC spectrum sliced at R3'.

This pulse sequence program was originally designed to quantitatively analyze the small proton-carbon coupling constants $J_{CH}$ from a 2D HSQC spectrum because of its non-distorted patterns. Also, the $^{13}$C satellite proton signal appearing along carbon domain on the 2D spectrum acquired from this pulse program coincidently solves our problem – by having two satellite signals separated by $^{13}$C (typically 125-160 Hz), non-first order proton signal can now adopt its first order pattern. A test of **12b** showed a first order doublet of doublet of R3' signal, 150 Hz apart each other separated by $^{13}$C, sliced from the corresponding carbon dimension (Figure 22). Usually the $^{1}$H FIDs are collected with $^{13}$C decoupled to leave a single correlation between $^{13}$C and the $^{1}$H bonding to it. In practice, one can collect exclusively the proton bonding to $^{13}$C, with $^{13}$C decoupling

deactivated. Without $^{13}C$ decoupling, it allows observation of $^{13}C$ satellite of proton signals in the absence of intense proton signals due to $^{1}H$-$^{12}C$ correlation. Thus, while protons on $^{12}C$ are overlapped and non-first order, protons on the $^{13}C$ satellites are shifted far enough to become first-order, offering precise measurement of 3-bond H-H coupling constants. However, 2D experiments are often long in experiment time and lack the digital resolution needed to extract accurate coupling constants. The resolution enhancement method we often used on a 1D spectrum does not apply to the slice of a 2D spectrum. Inspired by the 1D version TOCSY experiments we've had experience with, and working with Eric Johnson, at Bruker, we modified this 2D PIP-HSQC into a 1D version of selective PIP-HSQC. In addition, as comparison, we modified the novel Bruker's pulse program 1D selective 'selhsqcqpsisp', at SJU, by rmoving the 'cpd2' entry to halt the $^{13}C$ decoupling at proton dimension during the acquisition, naming it 'selhsqcgpNDsisp' (ND stand for 'no decoupling'). The two pulse programs are illustrated in Figure 23. Note here modified PIP-HSQC affords pure in phase experiments when the delay $\Delta$ is optimized as a function of $^{1}J$(CH), as well as a gradient-based $^{1}H$ z-filter applying before the acquisition. We tested the two pulse programs with standard samples, 30% menthol in $CDCl_3$ and 10% ethylbenzene in $CDCl_3$. These two samples were chosen for, first, testing carbon selectivity of the pulse program, and second, testing the first order pattern from a higher order signal. We evaluated the two pulse programs based on the selectivity, signal-to-Noise (S/N) ratio, and the natural line shape of the first order signal. Note here the key factor on the sensitivity of satellite signals is the $180^{\circ}$ $^{1}H$ refocusing pulse, controlled by shape pulse parameter Gaus1_180r.1000, and of its selective length (p36) and power level (spw26). The following length of selective pulses

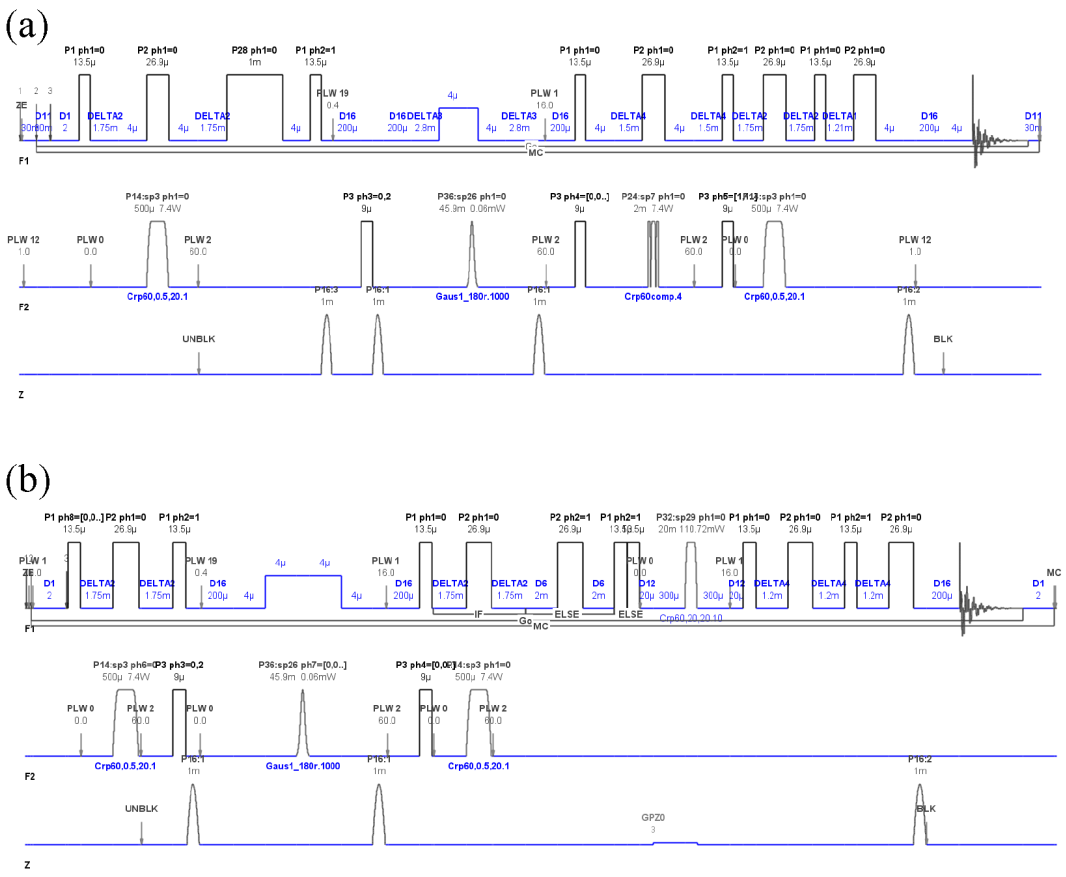


**Figure 23.** Two pulse sequence are illustrated (a) 'selhsqcqpsisp' and (b) 'selpiphsqc'. The delay Δ of 'selpiphsqc' is set to $1/[2^1J(CH)]$. The z-filter of 'selpiphsqc' utilizes a chirped adiabatic 180° $^1$H pulse applied with a purging GPZ0 gradient.

were chosen, 92435 µs, 45873 µs, 23497 µs, 11732 µs, 9366 µs, and 4616 µs, leading to the selective excitation bandwidth of 10 Hz, 20 Hz, 40 Hz, 80 Hz, 100 Hz, and 200 Hz, respectively. The delay D2 was set accordingly, based on the acquisition time. Delay in the program is also calculated based on the constant CNST2, which was set based on the measured Δ$\nu$ of the two satellite proton signals. The results of 30% menthol (Figure 24) are summarized in Table 6. Selected at 71.199 ppm (o2p), experiments of 'selhsqcgpNDsisp' revealed similar S/N ratio, roughly all above 250, expect the one with selected bandwidth at 20 Hz (p36 =45.873 µs, spw26 =56.1 µW), with S/N ratio at 64.

On the other hand, experiments of ‘selpiphsqc’ activated at the same carbon all suffered from poor S/N, with the highest only at 130, with bandwidth at 100 Hz. Experiments selected at 15.94 ppm (o2p) showed overall high S/N, applying to both pulse program, except one ‘selhsqcgpNDsisp’ experiment with selected bandwidth at 20 Hz. Experiments selected on this carbon showed similar S/N outcomes between ‘selhsqcgpNDsisp’ and ‘selpiphsqc’, with few exceptions, mainly at long pulses/shorter selective integral width. In general, ‘selhsqcgpNDsisp’ consistently suffered from phase distortion, which slightly affected the extracted coupling constants (Figure 25). The applied z-filter in PIP-HSQC did help to achieve better line shape, however, S/N of ‘selpiphsqc’ is in general lower than S/N of ‘selhsqcgpNDsisp’. In addition, in case of menthol, S/N of experiments selected at 15.94 ppm (o2p) are generally greater than experiments selected at 71.199 ppm (o2p).

| Sample | p36 (us) | spw26 | | Intergral width (Hz) | sino | ns | o2p | pulprog | CNST2 | | lb | gb | td | si | d1 (s) |
|---|---|---|---|---|---|---|---|---|---|---|---|---|---|---|---|
| | | (uW) | dB | | | | | | used | measured | | | | | |
| 30% menthol w/ selhsqcND | 92.435 | 13.8 | 48.59 | 10 | 256 | 64 | 71.199 | selhsqcgNDsisp | 125 | 138 | -0.5 | 0.04 | 65536 | 65536 | 2 |
| | 45.873 | 56.1 | 42.51 | 20 | 64 | 64 | 71.199 | selhsqcgNDsisp | 125 | 138 | -0.5 | 0.04 | 65536 | 65536 | 2 |
| | 23.497 | 210 | 36.78 | 40 | 282 | 64 | 71.199 | selhsqcgNDsisp | 125 | 138 | -0.5 | 0.04 | 65536 | 65536 | 2 |
| | 11.732 | 858 | 30.67 | 80 | 261 | 64 | 71.199 | selhsqcgNDsisp | 125 | 138 | -0.5 | 0.04 | 65536 | 65536 | 2 |
| | 9.366 | 1346 | 28.71 | 100 | 292 | 64 | 71.199 | selhsqcgNDsisp | 125 | 138 | -0.5 | 0.04 | 65536 | 65536 | 2 |
| | 4.614 | 5542 | 22.56 | 200 | 270 | 64 | 71.199 | selhsqcgNDsisp | 125 | 138 | -0.5 | 0.04 | 65536 | 65536 | 2 |
| | **45.873** | 56.1 | 52.51 | 20 | 155 | 64 | 15.94 | selhsqcgNDsisp | 125 | 124 | -0.5 | 0.04 | 65536 | 65536 | 2 |
| | **40.000** | 73.812 | 41.32 | ~25 | 652 | 64 | 15.94 | selhsqcgNDsisp | 125 | 124 | -0.5 | 0.04 | 65536 | 65536 | 2 |
| | **23.497** | 210 | 36.78 | 40 | 914 | 64 | 15.94 | selhsqcgNDsisp | 125 | 124 | -0.5 | 0.04 | 65536 | 65536 | 2 |
| | **11.732** | 858 | 30.67 | 80 | 396 | 64 | 15.94 | selhsqcgNDsisp | 125 | 124 | -0.5 | 0.04 | 65536 | 65536 | 2 |
| | **9.366** | 1346 | 28.71 | 100 | 346 | 64 | 15.94 | selhsqcgNDsisp | 125 | 124 | -0.5 | 0.04 | 65536 | 65536 | 2 |
| | **4.616** | 5542 | 22.56 | 200 | 721 | 64 | 15.94 | selhsqcgNDsisp | 125 | 124 | -0.5 | 0.04 | 65536 | 65536 | 2 |
| 30% menthol w/ sel-pip-HSQC | 92.435 | 13.8 | 48.59 | 10 | 44 | 64 | 71.199 | spiphsqc1d_8 | 125 | 138 | -0.5 | 0.04 | 65536 | 65536 | 2 |
| | 45.873 | 56.1 | 42.51 | 20 | 28 | 64 | 71.199 | spiphsqc1d_8 | 125 | 138 | -0.5 | 0.04 | 65536 | 65536 | 2 |
| | 23.497 | 210 | 36.78 | 40 | 29 | 64 | 71.199 | spiphsqc1d_8 | 125 | 138 | -0.5 | 0.04 | 65536 | 65536 | 2 |
| | 11.732 | 858 | 30.67 | 80 | 12 | 64 | 71.199 | spiphsqc1d_8 | 125 | 138 | -0.5 | 0.04 | 65536 | 65536 | 2 |
| | 9.366 | 1346 | 28.71 | 100 | 130 | 64 | 71.199 | spiphsqc1d_8 | 125 | 138 | -0.5 | 0.04 | 65536 | 65536 | 2 |
| | 4.614 | 5542 | 22.56 | 200 | 41 | 64 | 71.199 | spiphsqc1d_8 | 125 | 138 | -0.5 | 0.04 | 65536 | 65536 | 2 |
| | 45.873 | 56.1 | 42.51 | 20 | 560 | 64 | 15.94 | spiphsqc1d_8 | 125 | 124 | -0.5 | 0.04 | 65536 | 65536 | 2 |
| | 40.000 | 73.812 | 41.32 | ~25 | 449 | 64 | 15.94 | spiphsqc1d_8 | 125 | 124 | -0.5 | 0.04 | 65536 | 65536 | 2 |
| | 23.497 | 210 | 36.78 | 40 | 458 | 64 | 15.94 | spiphsqc1d_8 | 125 | 124 | -0.5 | 0.04 | 65536 | 65536 | 2 |
| | 11.732 | 858 | 30.67 | 80 | 428 | 64 | 15.94 | spiphsqc1d_8 | 125 | 124 | -0.5 | 0.04 | 65536 | 65536 | 2 |
| | 9.366 | 1346 | 28.71 | 100 | 443 | 64 | 15.94 | spiphsqc1d_8 | 125 | 124 | -0.5 | 0.04 | 65536 | 65536 | 2 |
| | 4.614 | 5542 | 22.56 | 200 | 735 | 64 | 15.94 | spiphsqc1d_8 | 125 | 124 | -0.5 | 0.04 | 65536 | 65536 | 2 |

**Table 6.** The signal-to-noise test on 'selpiphsqc' and 'selhsqcgpNDsisp' pulse programs of 30% menthol sample at various selected bandwidths. Selected integral width and S/N are highlighted in grey cells.

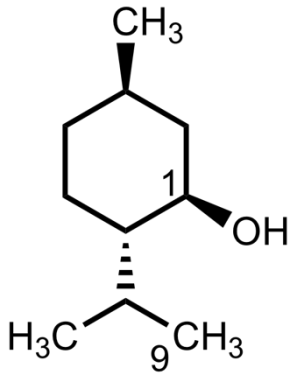


**Figure 24.** Chemical structure of (-)-menthol. In the study, two selected carbons include C1 at 71.199 ppm and C9 at 15.94 ppm, as labeled in the figure.

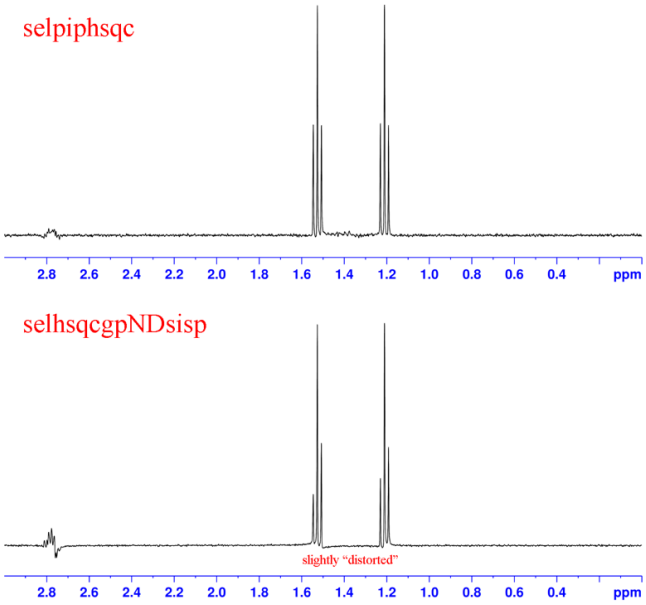


**Figure 25.** The above ethylbenzene spectrum is the 'selpiphsqc' spectrum selected at 15.94 (o2p), the $CH_3$ carbon of ethylbenzene, and the bottom spectrum is the 'selhsqcgpNDsisp' spectrum selected at the same carbon. The extracted coupling constants of the above spectrum are respectively 7.67, 7.67, 7.67, 7.66 Hz, and the extracted coupling constants of the bottom spectrum are respectively 7.64, 7.62, 7.67, 7.63 Hz. Note the variation the bottom spectrum has.

The results of ethylbenzene are summarized in Table 7, results of 'selhsqcgpNDsisp' experiments, and Table 8, results of 'selpiphsqc' experiments. Selected at 15.715 ppm ($CH_3$), the carbon associated with first order pattern proton signal, both 'selhsqcgpNDsisp' and 'selpiphsqc' revealed similar S/N. The carbon

satellites were tested on the aromatic carbons of ethylbenzene. Selected at 125.686 ppm (C4), the attached hydrogen has two hydrogen neighbors, thus H4 appears as a triplet with two satellite signals 160 Hz apart each other as before. At 40 Hz bandwidth and above, additional proton signals started to appear, due to the lack of selectivity of the $^{13}C$ pulse. Similar results were observed selected at 127.952 ppm (C2) and 128.405 ppm (C3). Poor S/N was observed on 'selpiphsqc' spectra selected on these non-first order associated carbons, and both pulse programs experienced distortion. For example, Figure 26 illustrates the 1D-selected experiments of 10% ethylbenzene, selected at 128.405 ppm (C3). Traces of 'selhsqcgpNDsisp' revealed decent first order pattern, despite the

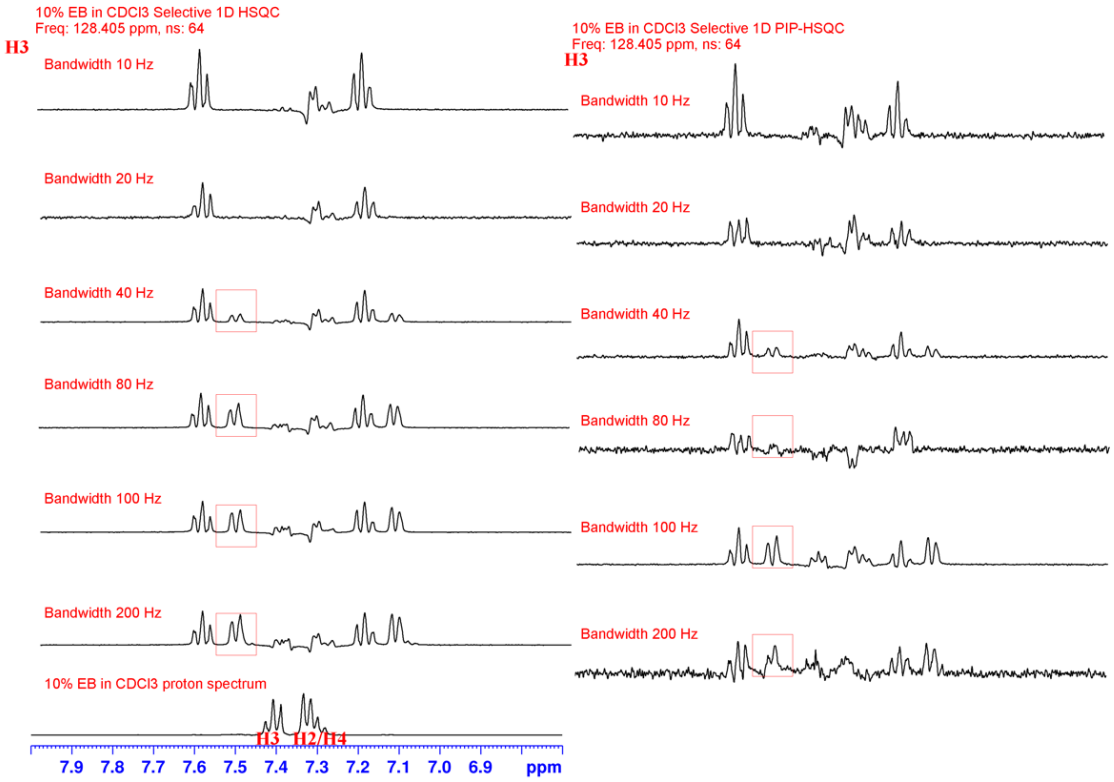


**Figure 26.** Comparison of spectra from selective 1D HSQC and selective 1D PIP-HSQC selected with different bandwidths, activated at carbon frequency 128.405 ppm. Addition signals are boxed on the spectrum.

| Sample | p36 (us) | spw26 | | Integral width (Hz) | sino | ns | o2p | pulprog | CNST2 | | lb | gb | td | si | d1 (s) | first order? |
|---|---|---|---|---|---|---|---|---|---|---|---|---|---|---|---|---|
| | | (uW) | dB | | | | | | used | measured | | | | | | |
| 10% Ethylbenzne in CDCl3 w/ selhsqcND | 92.435 | 13.8 | 48.59 | 10 | 131 | 64 | 15.715 | selhsqcgNDsisp | 125 | 126 | -0.5 | 0.04 | 65536 | 65536 | 2 | |
| | 45.873 | 56.1 | 42.51 | 20 | 50 | 64 | 15.715 | selhsqcgNDsisp | 125 | 126 | -0.5 | 0.04 | 65536 | 65536 | 2 | |
| | 23.497 | 210 | 36.78 | 40 | 243 | 64 | 15.715 | selhsqcgNDsisp | 125 | 126 | -0.5 | 0.04 | 65536 | 65536 | 2 | |
| | 11.732 | 858 | 30.67 | 80 | 120 | 64 | 15.715 | selhsqcgNDsisp | 125 | 126 | -0.5 | 0.04 | 65536 | 65536 | 2 | |
| | 9.366 | 1346 | 28.71 | 100 | 118 | 64 | 15.715 | selhsqcgNDsisp | 125 | 126 | -0.5 | 0.04 | 65536 | 65536 | 2 | |
| | 4.614 | 5542 | 22.56 | 200 | 174 | 64 | 15.715 | selhsqcgNDsisp | 125 | 126 | -0.5 | 0.04 | 65536 | 65536 | 2 | |
| | | | | | | | | | | | | | | | | |
| | 92.435 | 13.8 | 48.59 | 10 | 63 | 64 | 125.686 | selhsqcgNDsisp | 125 | 160 | -0.5 | 0.04 | 65536 | 65536 | 2 | t |
| | 45.873 | 56.1 | 42.51 | 20 | 21 | 64 | 125.686 | selhsqcgNDsisp | 160 | 160 | -0.5 | 0.04 | 65536 | 65536 | 2 | t |
| | 23.497 | 210 | 36.78 | 40 | 90 | 64 | 125.686 | selhsqcgNDsisp | 160 | 160 | -0.5 | 0.04 | 65536 | 65536 | 2 | t |
| | 11.732 | 858 | 30.67 | 80 | 97 | 64 | 125.686 | selhsqcgNDsisp | 160 | 160 | -0.5 | 0.04 | 65536 | 65536 | 2 | t |
| | 9.366 | 1346 | 28.71 | 100 | 95 | 64 | 125.686 | selhsqcgNDsisp | 160 | 160 | -0.5 | 0.04 | 65536 | 65536 | 2 | t |
| | 4.614 | 5542 | 22.56 | 200 | 102 | 64 | 125.686 | selhsqcgNDsisp | 160 | 160 | -0.5 | 0.04 | 65536 | 65536 | 2 | N/A |
| | | | | | | | | | | | | | | | | |
| | 92.435 | 13.8 | 48.59 | 10 | 138 | 64 | 127.952 | selhsqcgNDsisp | 160 | 160 | -0.5 | 0.04 | 65536 | 65536 | 2 | d |
| | 45.873 | 56.1 | 42.51 | 20 | 37 | 64 | 127.952 | selhsqcgNDsisp | 160 | 160 | -0.5 | 0.04 | 65536 | 65536 | 2 | d |
| | 23.497 | 210 | 36.78 | 40 | 150 | 64 | 127.952 | selhsqcgNDsisp | 160 | 160 | -0.5 | 0.04 | 65536 | 65536 | 2 | d; other signals |
| | 11.732 | 858 | 30.67 | 80 | 157 | 64 | 127.952 | selhsqcgNDsisp | 160 | 160 | -0.5 | 0.04 | 65536 | 65536 | 2 | d; other signals |
| | 9.366 | 1346 | 28.71 | 100 | 167 | 64 | 127.952 | selhsqcgNDsisp | 160 | 160 | -0.5 | 0.04 | 65536 | 65536 | 2 | d; other signals |
| | 4.614 | 5542 | 22.56 | 200 | 154 | 64 | 127.952 | selhsqcgNDsisp | 160 | 160 | -0.5 | 0.04 | 65536 | 65536 | 2 | d; other signals |
| | | | | | | | | | | | | | | | | |
| | 92.435 | 13.8 | 48.59 | 10 | 141 | 64 | 128.405 | selhsqcgNDsisp | 160 | 160 | -0.5 | 0.04 | 65536 | 65536 | 2 | t |
| | 45.873 | 56.1 | 42.51 | 20 | 36 | 64 | 128.405 | selhsqcgNDsisp | 160 | 160 | -0.5 | 0.04 | 65536 | 65536 | 2 | t |
| | 23.497 | 210 | 36.78 | 40 | 164 | 64 | 128.405 | selhsqcgNDsisp | 160 | 160 | -0.5 | 0.04 | 65536 | 65536 | 2 | t; other signals |
| | 11.732 | 858 | 30.67 | 80 | 168 | 64 | 128.405 | selhsqcgNDsisp | 160 | 160 | -0.5 | 0.04 | 65536 | 65536 | 2 | t; other signals |
| | 9.366 | 1346 | 28.71 | 100 | 169 | 64 | 128.405 | selhsqcgNDsisp | 160 | 160 | -0.5 | 0.04 | 65536 | 65536 | 2 | t; other signals |
| | 4.614 | 5542 | 22.56 | 200 | 165 | 64 | 128.405 | selhsqcgNDsisp | 160 | 160 | -0.5 | 0.04 | 65536 | 65536 | 2 | t; other signals |

**Table 7.** The signal-to-noise test on selhsqcgpNDsisp pulse programs of 10% ethylbenzene sample at various selected bandwidths. Selected integral width, S/N, and multiplicity pattern are highlighted in grey cells.

| Sample | p36 (us) | spw26 | | Integral width (Hz) | sino | ns | o2p | pulprog | CNST2 | | lb | gb | td | si | d1 (s) | first order? |
|---|---|---|---|---|---|---|---|---|---|---|---|---|---|---|---|---|
| | | (uW) | dB | | | | | | used | measured | | | | | | |
| 10% Ethylbenzne in CDCl3 w/ sel-PIP-HSQC | 92.435 | 13.8 | 48.59 | 10 | 128 | 64 | 15.715 | spiphsqc1d_8 | 125 | 126 | -0.5 | 0.04 | 65536 | 65536 | 2 | |
| | 45.873 | 56.1 | 42.51 | 20 | 140 | 64 | 15.715 | spiphsqc1d_8 | 125 | 126 | -0.5 | 0.04 | 65536 | 65536 | 2 | |
| | 23.497 | 210 | 36.78 | 40 | 126 | 64 | 15.715 | spiphsqc1d_8 | 125 | 126 | -0.5 | 0.04 | 65536 | 65536 | 2 | |
| | 11.732 | 858 | 30.67 | 80 | 107 | 64 | 15.715 | spiphsqc1d_8 | 125 | 126 | -0.5 | 0.04 | 65536 | 65536 | 2 | |
| | 9.366 | 1346 | 28.71 | 100 | 119 | 64 | 15.715 | spiphsqc1d_8 | 125 | 126 | -0.5 | 0.04 | 65536 | 65536 | 2 | |
| | 4.614 | 5542 | 22.56 | 200 | 144 | 64 | 15.715 | spiphsqc1d_8 | 125 | 126 | -0.5 | 0.04 | 65536 | 65536 | 2 | |
| | | | | | | | | | | | | | | | | |
| | 92.435 | 13.8 | 48.59 | 10 | 18 | 64 | 125.686 | spiphsqc1d_8 | 160 | 160 | -0.5 | 0.04 | 65536 | 65536 | 2 | t |
| | 45.873 | 56.1 | 42.51 | 20 | 10 | 64 | 125.686 | spiphsqc1d_8 | 160 | 160 | -0.5 | 0.04 | 65536 | 65536 | 2 | t |
| | 23.497 | 210 | 36.78 | 40 | 18 | 64 | 125.686 | spiphsqc1d_8 | 160 | 160 | -0.5 | 0.04 | 65536 | 65536 | 2 | t |
| | 11.732 | 858 | 30.67 | 80 | 4 | 64 | 125.686 | spiphsqc1d_8 | 160 | 160 | -0.5 | 0.04 | 65536 | 65536 | 2 | N/A |
| | 9.366 | 1346 | 28.71 | 100 | 38 | 64 | 125.686 | spiphsqc1d_8 | 160 | 160 | -0.5 | 0.04 | 65536 | 65536 | 2 | t |
| | 4.614 | 5542 | 22.56 | 200 | 6 | 64 | 125.686 | spiphsqc1d_8 | 160 | 160 | -0.5 | 0.04 | 65536 | 65536 | 2 | N/A |
| | | | | | | | | | | | | | | | | |
| | 92.435 | 13.8 | 48.59 | 10 | 23 | 64 | 127.952 | spiphsqc1d_8 | 160 | 160 | -0.5 | 0.04 | 65536 | 65536 | 2 | d |
| | 45.873 | 56.1 | 42.51 | 20 | 15 | 64 | 127.952 | spiphsqc1d_8 | 160 | 160 | -0.5 | 0.04 | 65536 | 65536 | 2 | d |
| | 23.497 | 210 | 36.78 | 40 | 29 | 64 | 127.952 | spiphsqc1d_8 | 160 | 160 | -0.5 | 0.04 | 65536 | 65536 | 2 | d; slight other signals |
| | 11.732 | 858 | 30.67 | 80 | 6 | 64 | 127.952 | spiphsqc1d_8 | 160 | 160 | -0.5 | 0.04 | 65536 | 65536 | 2 | N/A |
| | 9.366 | 1346 | 28.71 | 100 | 67 | 64 | 127.952 | spiphsqc1d_8 | 160 | 160 | -0.5 | 0.04 | 65536 | 65536 | 2 | d; other signals |
| | 4.614 | 5542 | 22.56 | 200 | 8 | 64 | 127.952 | spiphsqc1d_8 | 160 | 160 | -0.5 | 0.04 | 65536 | 65536 | 2 | d; other signals |
| | | | | | | | | | | | | | | | | |
| | 92.435 | 13.8 | 48.59 | 10 | 27 | 64 | 128.405 | spiphsqc1d_8 | 160 | 160 | -0.5 | 0.04 | 65536 | 65536 | 2 | t |
| | 45.873 | 56.1 | 42.51 | 20 | 13 | 64 | 128.405 | spiphsqc1d_8 | 160 | 160 | -0.5 | 0.04 | 65536 | 65536 | 2 | t |
| | 23.497 | 210 | 36.78 | 40 | 32 | 64 | 128.405 | spiphsqc1d_8 | 160 | 160 | -0.5 | 0.04 | 65536 | 65536 | 2 | t; slight other signals |
| | 11.732 | 858 | 30.67 | 80 | 7 | 64 | 128.405 | spiphsqc1d_8 | 160 | 160 | -0.5 | 0.04 | 65536 | 65536 | 2 | N/A |
| | 9.366 | 1346 | 28.71 | 100 | 66 | 64 | 128.405 | spiphsqc1d_8 | 160 | 160 | -0.5 | 0.04 | 65536 | 65536 | 2 | t; other signals |
| | 4.614 | 5542 | 22.56 | 200 | 8 | 64 | 128.405 | spiphsqc1d_8 | 160 | 160 | -0.5 | 0.04 | 65536 | 65536 | 2 | N/A |

**Table 8.** The signal-to-noise test on selpiphsqc pulse programs of 10% ethylbenzene sample at various selected bandwidths. Selected integral width, S/N, and multiplicity pattern are highlighted in grey cells.

appearance of additional signal, because of the relatively better S/N. On the other hand, traces of 'selpiphsqc', for instance, at bandwidth of 80 Hz, lost its first order pattern, having two signal margining together, due to, poor S/N after only 64 scans, and $\Delta\nu/J$ with neighboring signal at roughly 5. The lack of sensitivity is thus indicated by addition signals that begin to appear at 40 Hz excitation bandwidth and wider. In summary, it is obvious that 'selpiphsqc' does help a non-first order signal adopting first order pattern, and obtain a better lineshape, nonetheless, it might sacrifice slightly on S/N ratio.

**cIDPR – A Real Challenge.** Test of the two modified pulse programs on **12b** resulted surprisingly. Following the similar setup at variable selected bandwidths and selected at R-C3, traces of 'selhsqcgpNDsisp' showed similar S/N ratio, with analyzable lineshape adopting first-order doublet of doublet. With increased number of scans, the S/N was enhanced significantly, and maintaining the same multiplicity pattern. However, traces of 'selpiphsqc' resulted in no significant signals at all selected bandwidths, except bandwidth at 100 Hz. Selecting 'selhsqcgpNDsisp' to be the pulse program, extracted coupling constants $J_{2,3}$, and $J_{3,4}$, were acquired at variable temperatures at P36 =11.732 μs. This pulse was chosen because of its best S/N results tested at room temperature. The results are listed in Table 9, along with coupling values extracted from slice of 2D HSQC. Margin of error of the two sets of data is relatively within 0.1 Hz. The spectra of 'selpiphsqc' shared the advantage having greater S/N, offering room for resolution enhancement. Figure 27 illustrates the obvious S/N enhancement between 1D selective spectrum and slice of 2D spectrum. Note here 'selhsqcgpNDsisp' introduced the natural distortion to one of the satellite signals, and such distortion shifted the accuracy of

extracted coupling constants. To minimize the error, coupling constants shown in Table 9 were calculated by averaging the extracted values of the two satellite signals.

| | T (K) | selpiphsqc | | Slice of PIP-HSQC | | Margin of Error (Hz) |
|---|---|---|---|---|---|---|
| | | *J*2'3' | *J*3'4' | *J*2'3' | *J*3'4' | |
| R ring | 277 K | 4.97 | 7.36 | 4.76 | 8.27 | 0.11 |
| | 298 K | 4.77 | 7.39 | 4.75 | 7.54 | 0.01 |
| | 318 K | 4.86 | 7.19 | 4.78 | 7.68 | 0.04 |
| | 338 K | 4.89 | 6.71 | 4.77 | 7.23 | 0.06 |
| | 353 K | N/A | N/A | 5.00 | 7.27 | N/A |

**Table 9.** Table of observed coupling constant *J* values of the R-ring of **12b** at variable temperature, extracted from 'selpiphsqc', and slice of 2D PIP-HSQC. Last column shows margin of error of the two sets of data.

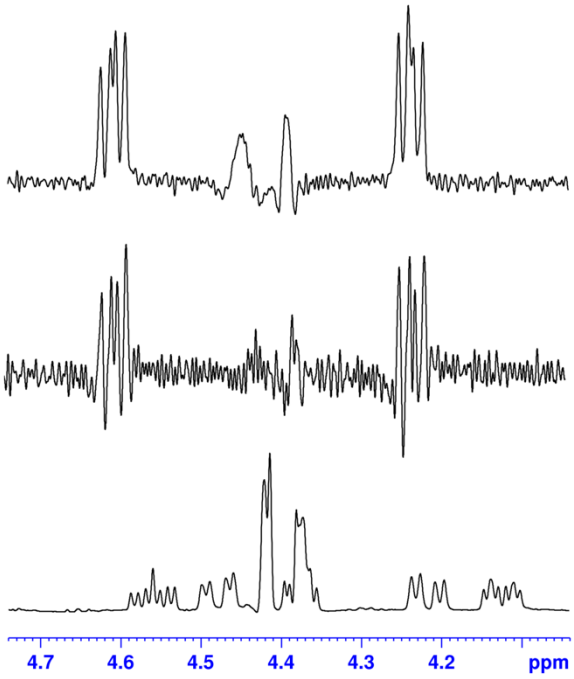


**Figure 27.** Comparison of three experiments of **12b** on R3'. The bottom spectrum is 1D $^{1}$H spectrum of 12b. The middle spectrum is slice of 2D PIP-HSQC spectrum selected at R-C3. The top spectrum is 'selpiphsqc' spectrum selected at R-C3.

## CONCLUSION

In summary, we have developed a successful and efficient synthetic method of **12b** with improved yield. Two methods with modified NMR pulse programs have been developed for the extraction of accurate and precise coupling constants from crowd, non-first order spectra of **12b** at variable temperature. The coupling constants extracted with the two methods were essentially similar. The S/N of 1D-sel HSQC was slightly better than 1D-sel PIP-HSQC. Satellite signals of 1D-sel HSQC were often distorted, while those of 1D-sel PIP-HSQC were pure in phase. In addition, the S/N ratio of signals in the 1D-sel PIP-HSQC were often less sensitive to the selected bandwidth of carbon signal.

## EXPERIMENTAL PROCEDURE

**General Information.** Moisture sensitive reactions in this study were performed under the atmosphere of dry nitrogen using syringe techniques. Hydrous solid disodium salt inosine monophosphate (IMP·x$H_2O$) obtained from commercial supplier, was dried via Electrothermal Chem Dry Oven at 35 °C under mechanical pump overnight prior to use. Diphenyl phosphoryl chloride (DPPC) and anhydrous dimethylformamide (DMF) were stored in a desiccated jar, used as obtained from commercial suppliers. Triethylamine (TEA) and pyridine were distilled from KOH prior to use. 2',3'-Di-O-acetyl nicotinamide mononucleotide ($Ac_2$NMN) was synthesized as desired from nicotinamide mononucleotide (NMN), the commercially available precursor. $Ac_2$NMN was dried by evaporating from toluene three times, and pumped on a mechanical oil pump prior to use. The enzyme ADP-ribosyl cyclase was purchased from commercial supplier Sigma, containing ~100 μg of protein at 2540 Unit/mg protein, per vial. Deionized water was 18.2 MΩ/cm quality. Analytical LC-MS and HPLC utilized a 250 × 4.60 mm 4 micron Synergi™ Fusion-RP column, an ACQUIY® QDa™ mass detector, and a UV array detector. Eluent A was generally 5 mM pH 3.0 formic acid solution (FA); eluent B was a 90:10 mixture of eluent A and 2-propanol; eluent D was a 75:25 mixture of acetonitrile (AcCN) and water (deionized). The seal wash and needle wash solvents were guided by the instruction manual provided by the manufacturer. The flow rate was generally 1 mL/min. Anion exchange chromatography was performed using a 12.5 × 2.5 cm column packed with Q Sepharose Fast Flow resins, conditioned by 1 M sodium acetate solution prior to use, and performed under either two methods, including triethylammonium acetate (TEAA) gradients, or trimethylammonium acetate (TMAA)

gradients. The flow rate of sample loading was generally 5 mL/min, and the flow rate of gradients was generally 10 mL/min. Cation exchange chromatography featured an 8.0 × 1.5 cm column packed with SP Sepharose Fast Flow resins, conditioned by 1 M sodium acetate solution prior to use, and eluted with deionized water. “Lyophilized” in this study signifies a frozen aqueous sample lyophilized on a dry-freeze system. “Evaporated” signifies removal of solvents, including water, on a rotary evaporator connecting to a diaphragm pump, or a mechanical oil pump for evaporation of high-boiling solvents.

**NMR Spectroscopy.** NMR spectra were acquired on Bruker’s 400 MHz spectrometer utilized a variable temperature (VT) unit, along with liquid nitrogen (LN) evaporator that had been recently calibrated. The 1D spectra, including routine $^{1}H$, $\{^{31}P\}^{1}H$, 1D TOSCY, and 1D NOESY, were collected with a spectral width of 8000 Hz, 64K time domain data point, and zero-filled processed to 128K points (giving spectral resolution of 0.06 Hz/pt). 1D HSQC spectra were collected with the same spectral width, but 128K time domain data point, and zero-filled to 128K points. The 2D PIP-HSQC were collected with a spectral width of 1000 Hz of the proton domain, 4K domain data point, and 4000 Hz of the carbon domain, 512 domain data point, and zero-filled to 64K and 2K, respectively. The 1D TOSCY mixing time was generally set to 30 ms. Resolution enhancement was routinely applied (lb ~ -4.0 Hz and gb ~ 0.12-0.18) to all spectra when processing. Samples were prepared by first lyophilized from ~ 1 mL 99% $D_2O$ twice, followed by subsequent dissolution in 99.96% $D_2O$ under the atmosphere of dry nitrogen gas. Samples were generally degassed with three cycles using Freeze-Pump-Thaw technique. The internal standard used was 3-(trimethylsilyl)-2,2,3,3-

tetradeuteropropionic acid (TMSP-$d_4$), and the spectra were generally shimmed when the half-height line width of the internal standard was less than 1 Hz. All spectra were acquired with ~ 100-200 mM concentrations. Assignments wre based on 1D TOCSY and 2D HMBC experiments.

**8-Bromoinosine 5'-Monophosphate (8-Br-IMP, 10b).** Solid **10a** (anhydrous disodium salt, 406.8 mg, 1.037 mmol) was dissolved in 0.4 M acetate buffer (15 mL, pH4.0), followed by freshly prepared bromine water (3.5% w/v, 20 mL) added dropwise into the solution over 5 minutes. The resulting dark red solution was wrapped in aluminum foil and stirred in dark at room temperature for approximately 2.5 days. The reaction process was monitored by LC-MS/HPLC (85:15 A: B, isocratic), following 75% conversion to the product (area%, $t_R$ ~7 min). The resulting slightly red solution (pH 3.3) was evaporated, following co-evaporation with water two additional times. The resulting residue was dissolved in water (400 mL). the pH of the crude product solution was adjusted to 8.1 with the addition of diluted NaOH solution. The reaction mixture was purified by GradiFrac through the preconditioned Q Sepharose Fast Flow column (acetate form) utilizing a gradient of 5-30% triethylammonium acetate (TEAA, 1 M, pH 7.0) over 1000 mL. Fraction 61-86 (25-30%B) were combined and evaporated. The resulting residue was evaporated two additional times from water, following five times from methanol (HPLC grade), till the formation of oily residue. The resulting oily residue was dissolved in water (1.5 mL) and added dropwise into ice-cold rapidly stirred acetone (HPLC grade, 49 mL). The resulting precipitate was centrifuged, followed with decantation of the supernatant. The precipitate was dissolved in water and lyophilized overnight to yield 287.5 mg (0.5445 mmol, 55%) of the monotriethylammonium salt of

**10b** (one equiv by NMR) as a glassy residue: $^1$H NMR (400 MHz, $D_2O$) δ 8.19 (s, 1H, H2), 6.14 (d, 1H, J = 5.7 Hz, H1'), 5.31 (t, 1H, J = 5.7 Hz, H2'), 4.66 (app t, 1H, J = 4.5/5.7 Hz, H3'), 4.31 (m, 1H, H4'), 4.22-4.10 (m, 2H, H5'/5''). HPLC (fusion-RP): $t_R$ ~7.3 min ($\lambda_{max}$ 254.2 nm). LC-MS (m/z, negative): cal. for $C_{10}H_{12}O_8BrN_4P$ 424.949791, 426.947744 (free acid), found 424.95, 426.89 (mobile phase pH 3.0).

**Nicotinamide 8-Bromohypoxanthine 5'-Dinucleotide (8-Br-NHD+, 11b).**

Solid **10b** (di-triethylammonium salt, 120.2 mg, 191.0 μmol) was dissolved in dry DMF (1000 μL) via syringe technique, followed by evaporation of the resulting solution to dryness. The procedure was repeated two additional times and the resulting residue was lyophilized overnight prior to use. The dry residue was dissolved in dry DMF (800 μL) the following day via syringe technique. Next, dry diphenyl phosphoryl chloride (DPPC, 60 μL, 286.5 μmol, 1.5 equiv) and dry trimethylamine (TEA, 80 μL, 573.0 μmol, 3 equiv) were added via syringe technique under the atmosphere of dry nitrogen. The reaction was run under the atmosphere of dry nitrogen thoroughly. The stirred suspension became cloudy within few minutes. The reaction process was monitored by LC-MS/HPLC (85:15 A: B isocratic for 8.5 min, then a linear gradient to 100%D over 10 min), monitoring the disappearance of staring IMP analog signal ($t_R$ ~7 min) and the appearance of the activated phosphoric anhydride ($t_R$ ~20 min). The phosphate activation was completed after 1-1.5 hours. The prepared dry solid 2',3'-di-O-acetyl nicotinamide mononucleotide ($Ac_2$-NMN, 243.3 mg, 581.7 μmol, 3.0 equiv) was added into the solution of crude activated mixed phosphoric anhydride. The reaction process was monitored by LC-MS/HPLC via same instrumental method as above, and this time monitoring the

disappearance of activated anhydride ($t_R$ ~20 min) and the appearance of $NHD^+$ analog ($t_R$ ~7 min). The reaction took 1-1.5 hr at room temperature. The resulting mixture was evaporated, and the resulting residue was dissolved in freshly prepared 1:1 $CH_3OH$: concentrated aqueous ammonia solution (2 mL), and stirred at room temperature for 15 min. the solution was then quickly evaporated, co-evaporated with water, and briefly lyophilized. Afterwards, the resulting residue was dissolved in water (50 mL), with the pH of crude products adjusted to 8.1 with the addition of diluted NaOH solution. The reaction mixture was purified by GradiFrac through preconditioned Q Sepharose Fast Flow column (acetate form) utilizing two gradients: first, 0-50% TMAA (0.5 M, pH 7.0) over 1000 mL, and second, 50-100% TMAA (0.5 M, pH 7.0) over 250 mL. The flow rate was at 8 mL/min. Fraction 28-41 (20-30%B) were combined and evaporated. Resulting residue was evaporated two times from water, followed by five times evaporation from MeOH (HPLC grade), five times evaporation from toluene, and five times evaporation form MeOH (HPLC grade), till the formation of oily residue. The resulting precipitate was dissolved in water and lyophilized to yield 53.4 mg (66.5 μmol, 34.8%) of the monotrimethylammonium salt of **11b** as light brown solid: $^1$H NMR (400 MHz, $D_2O$) δ 9.38 (s, 1H, Nic-H2), 9.20 (d, 1H, J = 6.3 Hz, Nic-H6), 8.94 (d, 1H, J = 8.1 Hz, Nic-H4), 8.29 (app t, 1H, J = 6.3/8.0 Hz, Nic-H5), 8.20 (s, 1H, Ino-H2), 6.09 (d, 1H, J = 5.4 Hz, A-H1'), 6.02 (d, 1H, J = 5.4 Hz, Nic-H1'), 5.24 (t, 1H, J = 5.6 Hz, Nic-H2'), 4.66 (t, 1H, J = 4.4/5.8 Hz, Nic-H3'), 4.51-4.46 (app t, 2H, A-H2'), 4.43 (dd, 1H, J = 2.7/5.1 Hz), 4.37-4.17 (m, 5H). HPLC (fusion-RP): $t_R$ ~6.8 min ($\lambda_{max}$ 254.2 nm). LC-MS (m/z, negative): cal. for $C_{21}H_{25}O_{15}BrN_6P_2$ 740.995831, 742.993784 (free acid), found 740.94, 742.80 (mobile phase pH 3.0).

**N1-Cyclic 8-Bromo-Inosine 5'-Diphosphate Ribose (8-Br-N1-cIDPR, 12b).**

Solid **11b** (25.3 mg, 31.5 μmol) was dissolved in 20 mL of water and diluted to 110 mL by the addition of HEPES buffer (25 mM, pH 7.0), with the pH of the resulting solution adjusted to be 7.21 by adding diluted KOH solution. The resulting solution was incubated with stock ADP-ribosyl cyclase solution (70 μL, 0.1-0.3 U/μL) at room temperature. The enzymatic cyclization process was monitored by LC-MS/HPLC (60:40 A: B, isocratic), monitoring the disappearance of **11b** ($t_R$ ~3.7 min) and the appearance of **12b** ($t_R$ ~9.3 min). once the signal of **11b** had disappeared, or the signal of **12b** ceased to increase. The solution was then diluted to 250 mL with water, with the pH adjusted to 6.3 by adding diluted HCl solution. The crude product was purified by GradiFrac via preconditioned Q Sepharose Fast Flow column (acetate form) utilizing two gradients: first, 0-50% TMAA (0.5 M, pH 7.0) over 500 mL; second, 50-100% TMAA (0.5 M, pH 7.0) over 500 mL. Fraction 39-47 (63-75%B) were combined and evaporated three times from water, following five times evaporation from methanol (HPLC grade), five times evaporation from toluene, and five times evaporation from MeOH (HPLC grade), till the formation of glassy residue. Resulting residue was dissolved in water (1.5 mL) and added dropwise into ice-cold rapidly stirred acetone (HPLC grade, 49 mL). The resulting solid precipitate was centrifuged, and supernatant removed by glass pipette. The precipitate was dissolved in water and lyophilized to yield 12.2 mg (16.5 μmol, 52.4%) of the ditrimethylammnium salt of **12b** as light brown powder. Resulting powder was dissolved in water (20 mL) and loaded onto the preconditioned SP Sepharose Fast Flow column (acetate form), eluted by water. Pure fractions were combined and lyophilized to obtain the disodium salt of **12b** as light brown powder: $^1$H NMR (400 MHz, $D_2O$, 298 K) δ 8.85 (s, 1H, H2), 6.14 (d, 1H, J

= 5.7 Hz, A-H1'), 6.01 (s, 1H, R-H1'), 5.33 (t, 1H, J = 5.4 Hz, A-H2'), 4.77 (dd, 1H, 3.2/5.0 Hz, A-H3'), 4.56 (dtd, 1H, A-H5'd), 4.48 (dd, 1H, J = 3.5/12 Hz, R-H5'd), 4.45-4.41 (m, 3H, R-H2', R-H3', and R-H4'), 4.21 (m, 1H, A-H4'), 4.21 (dd, 1H, J = 4.4/11.8 Hz, R-H5'u), 4.12 (dt, 1H, J = 3.6/11.0 Hz, A-H5'u). $^{13}$C NMR (400 MHz, $D_2O$, 298 K) δ 159.2, 152.0, 147.0 (C2), 131.5, 126.6, 94.7 (R1), 94.0 (A1), 87.5 (d, J = 10.4 Hz, A4), 86.1 (d, J = 9.4 Hz, R4), 78.3 (R3), 75.5 (A2), 73.3 (A3), 70.4 (R2), 67.6 (d, J = 5.1 Hz, A5), 65.1 (d, J = 3.6 Hz, R5). $^{1}$H{$^{31}$P} NMR (400 MHz, D2O, 298 K) (only the signals that changed upon $^{31}$P decoupling are listed) δ 4.56 (dd, J = 11.0/7.4 Hz, A-H5'd), 4.48 (d, J = 11.7 Hz, R-H5'd), 4.21 (d, J = 11.7 Hz, R-H5'u), 4.12 (dd, J = 11.0/3.0 Hz, A-H5'u). HPLC (Fusion-RP): $t_R$ ~9.3 min ($\lambda_{max}$ 255.4 nm). LCMS (m/z, negative): cal. for $C_{15}H_{17}O_{14}BrN_4P_2$ 618.947818, 620.945771 (free acid), found 618.99, 621.08 (mobile phase pH 3.0).

# APPENDICES

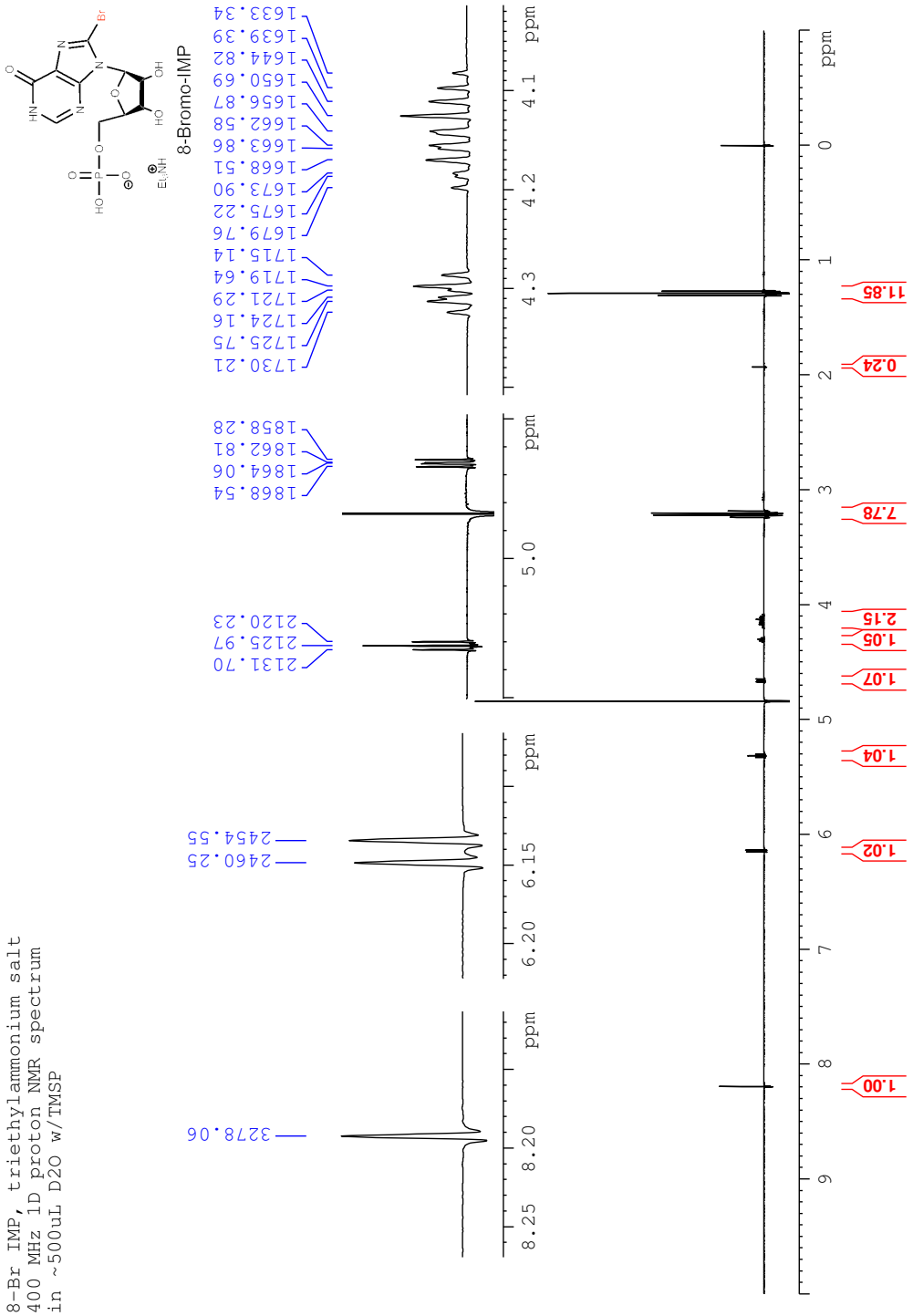


**Appendix 1.** $^{1}$H spectrum of 8-Br IMP, triethylammonium salt.

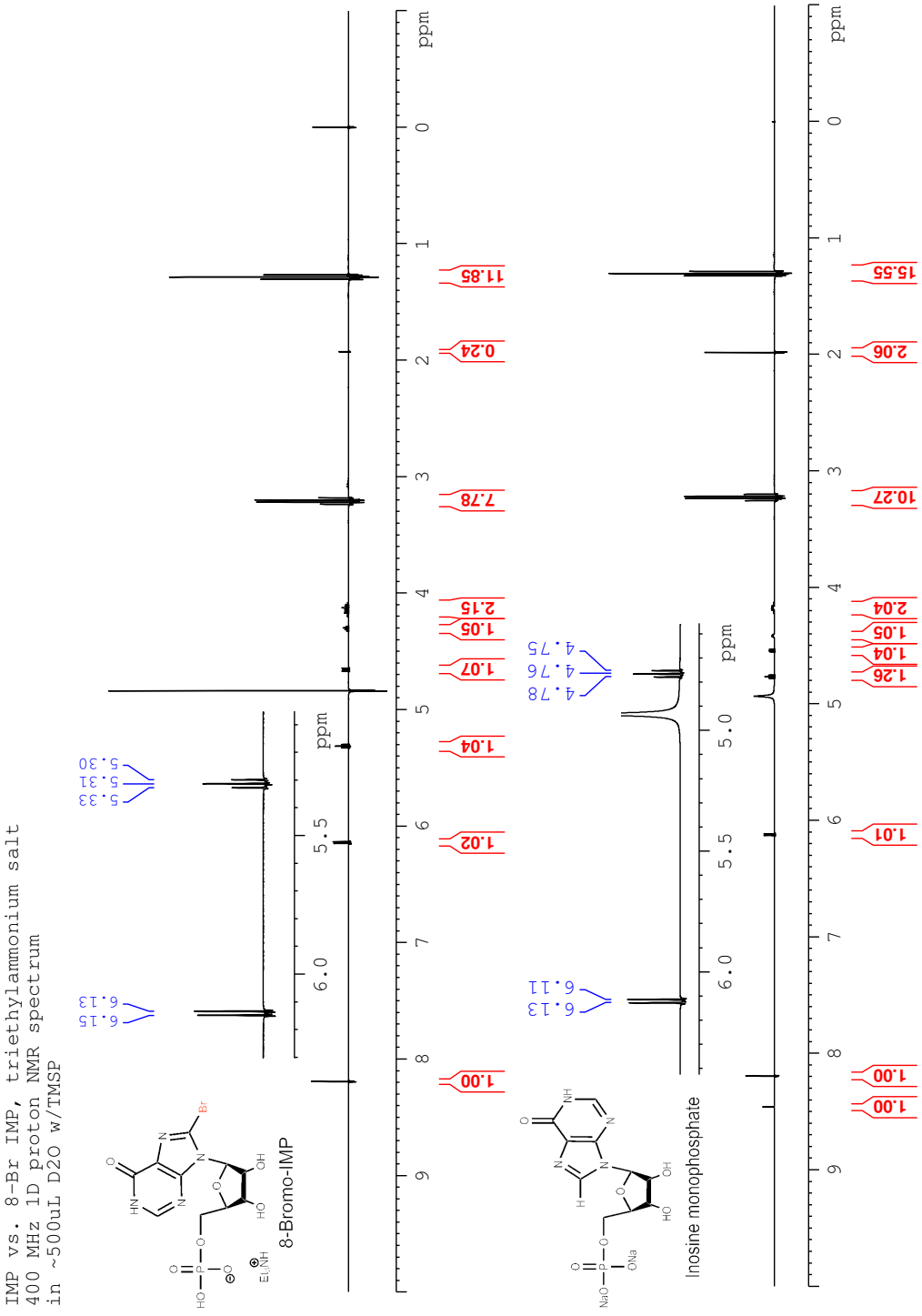


**Appendix 2.** Comparison of $^{1}H$ spectra of IMP and Br-IMP.

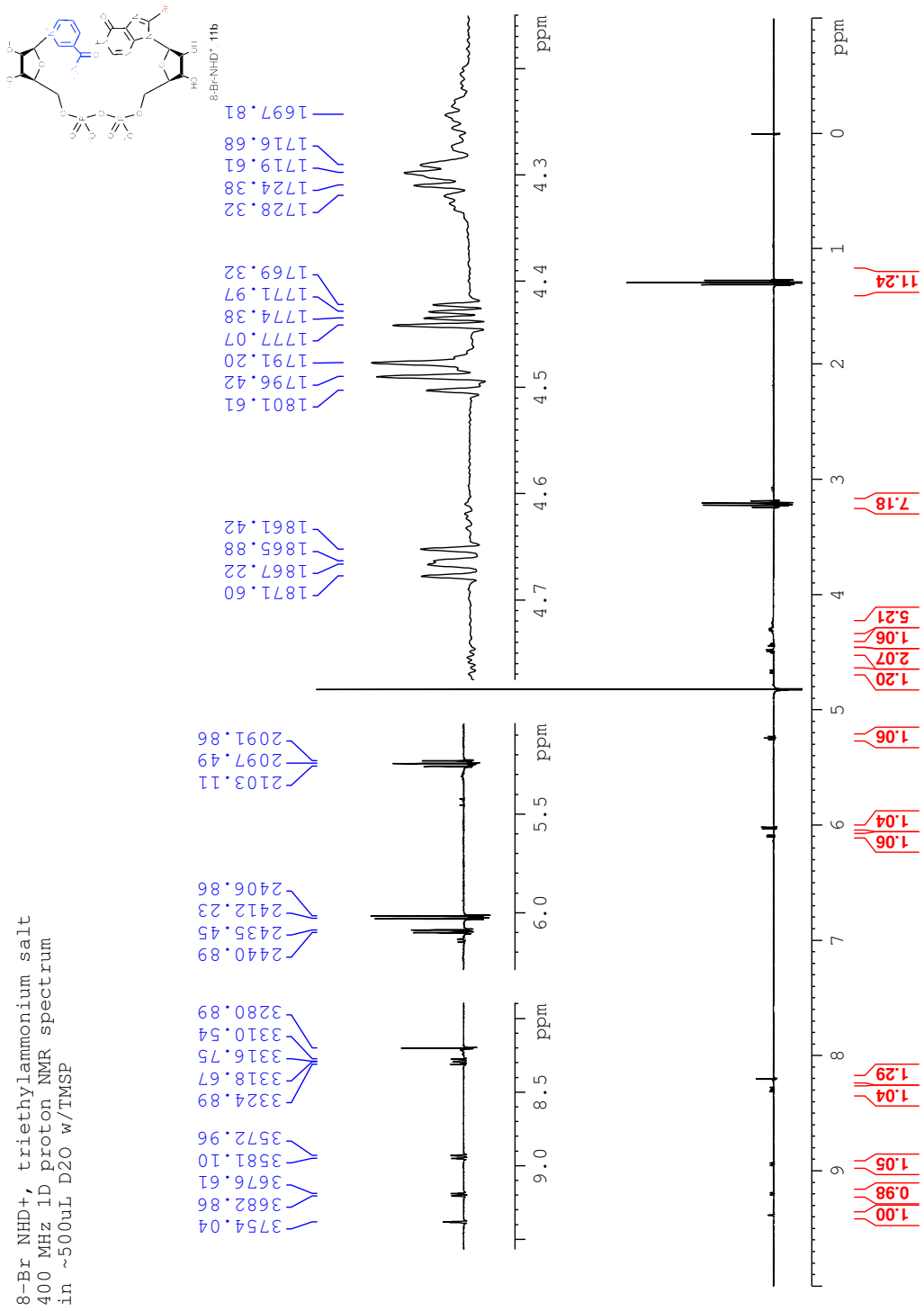


**Appendix 3.** $^{1}$H spectrum of 8-Br NHD$^{+}$, triethylammonium salt.

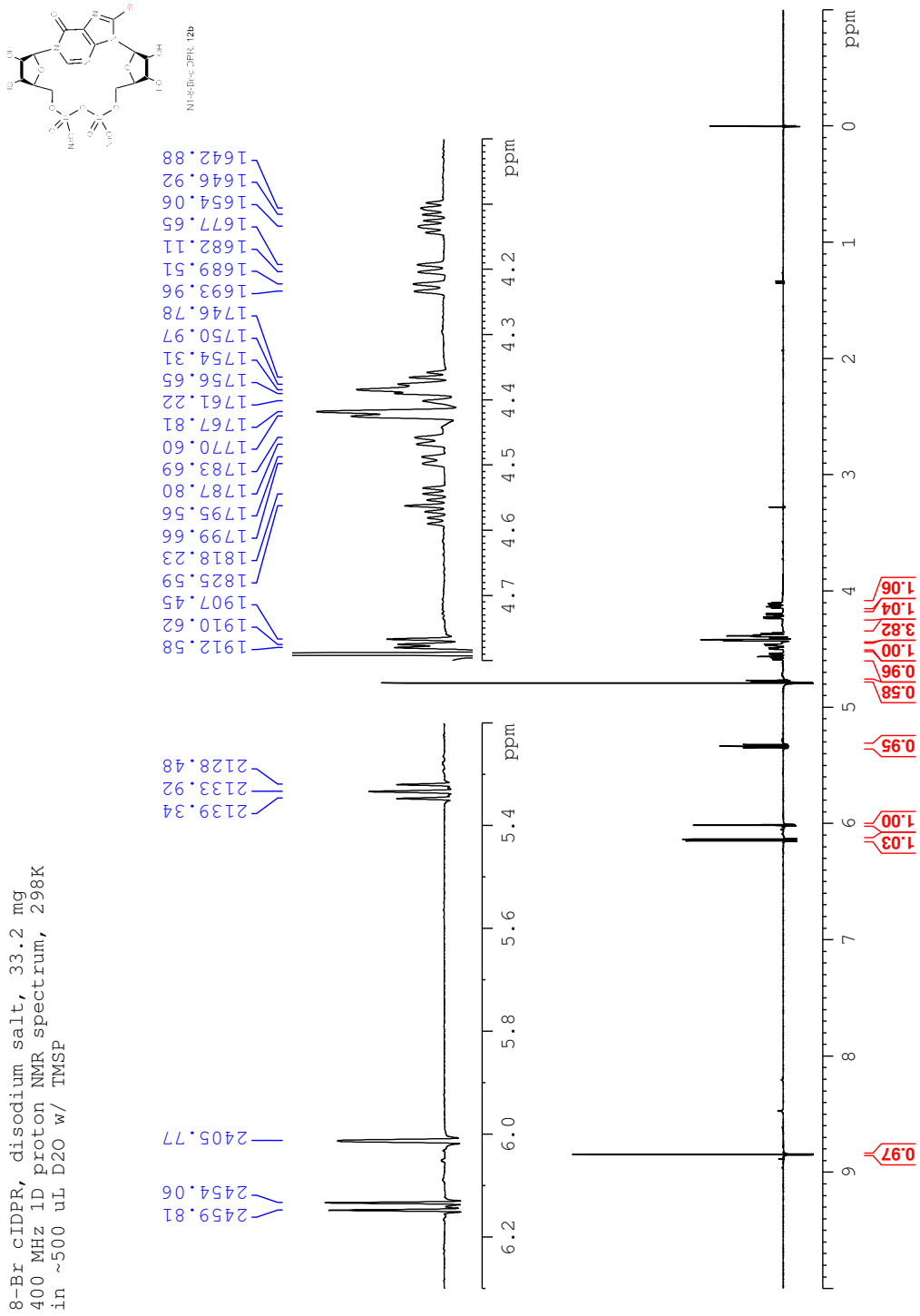


**Appendix 4.** [1]H spectrum of 8-Br-N1-cIDPR, sodium salt, at 298K.

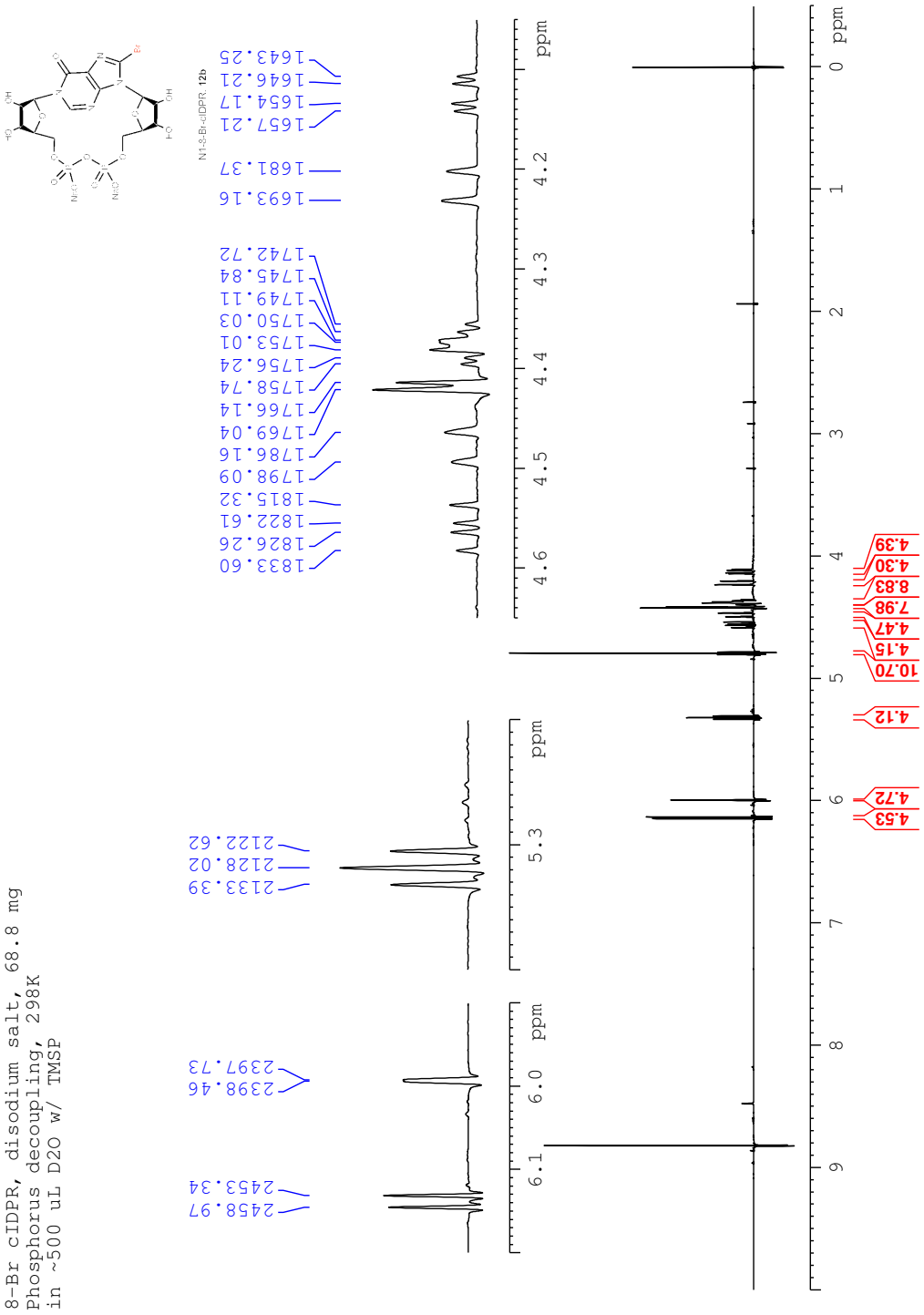


**Appendix 5.** $^{1}H$ and $^{1}H\{^{31}P\}$ spectrum of 8-Br-N1-cIDPR, sodium salt, at 298K.

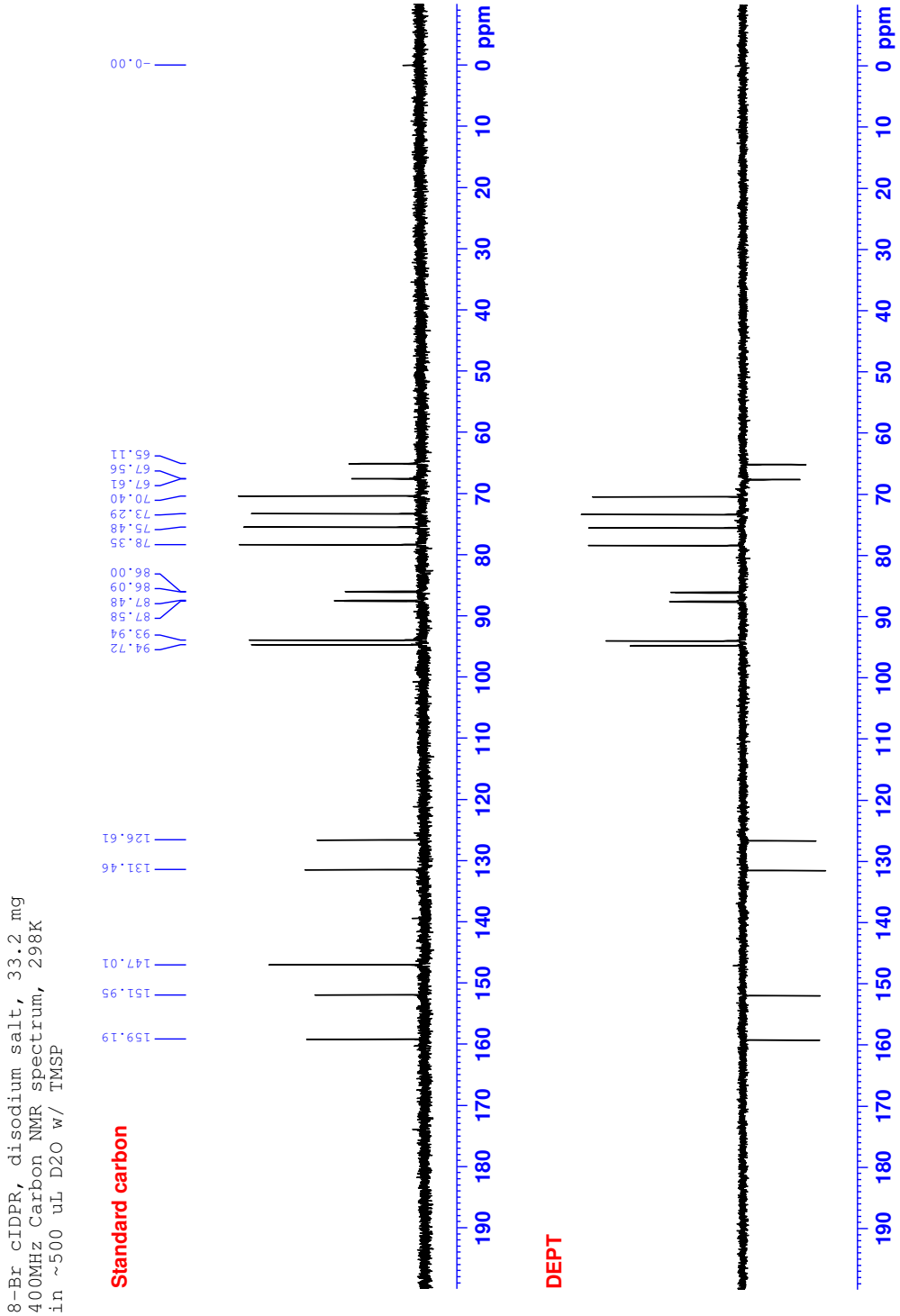


**Appendix 6.** $^{13}C$ and DEPT $^{13}C$ spectra of 8-Br-N1-cIDPR, at 298K.

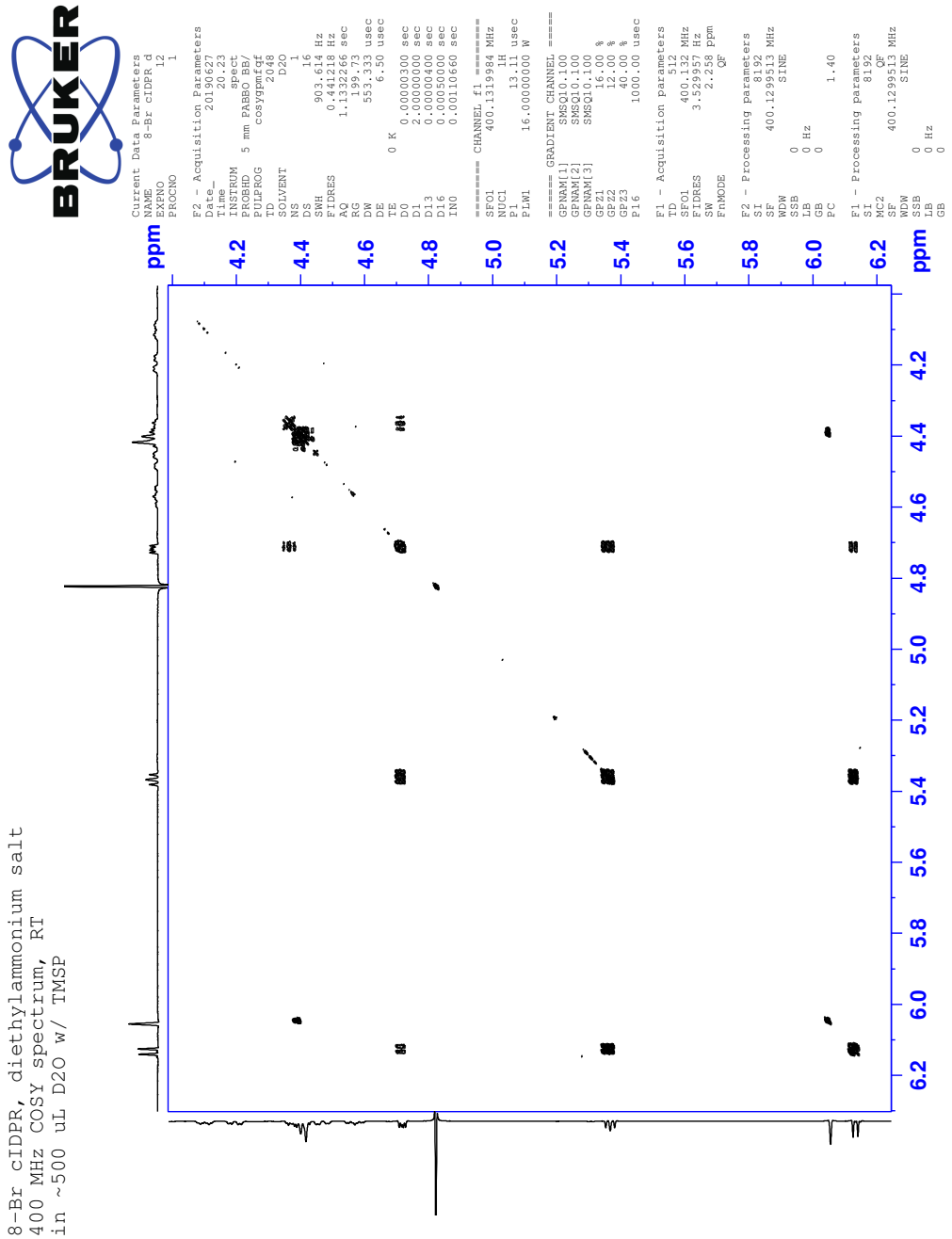


**Appendix 7.** COSY spectrum of 8-Br-N1-cIDPR, at RT.

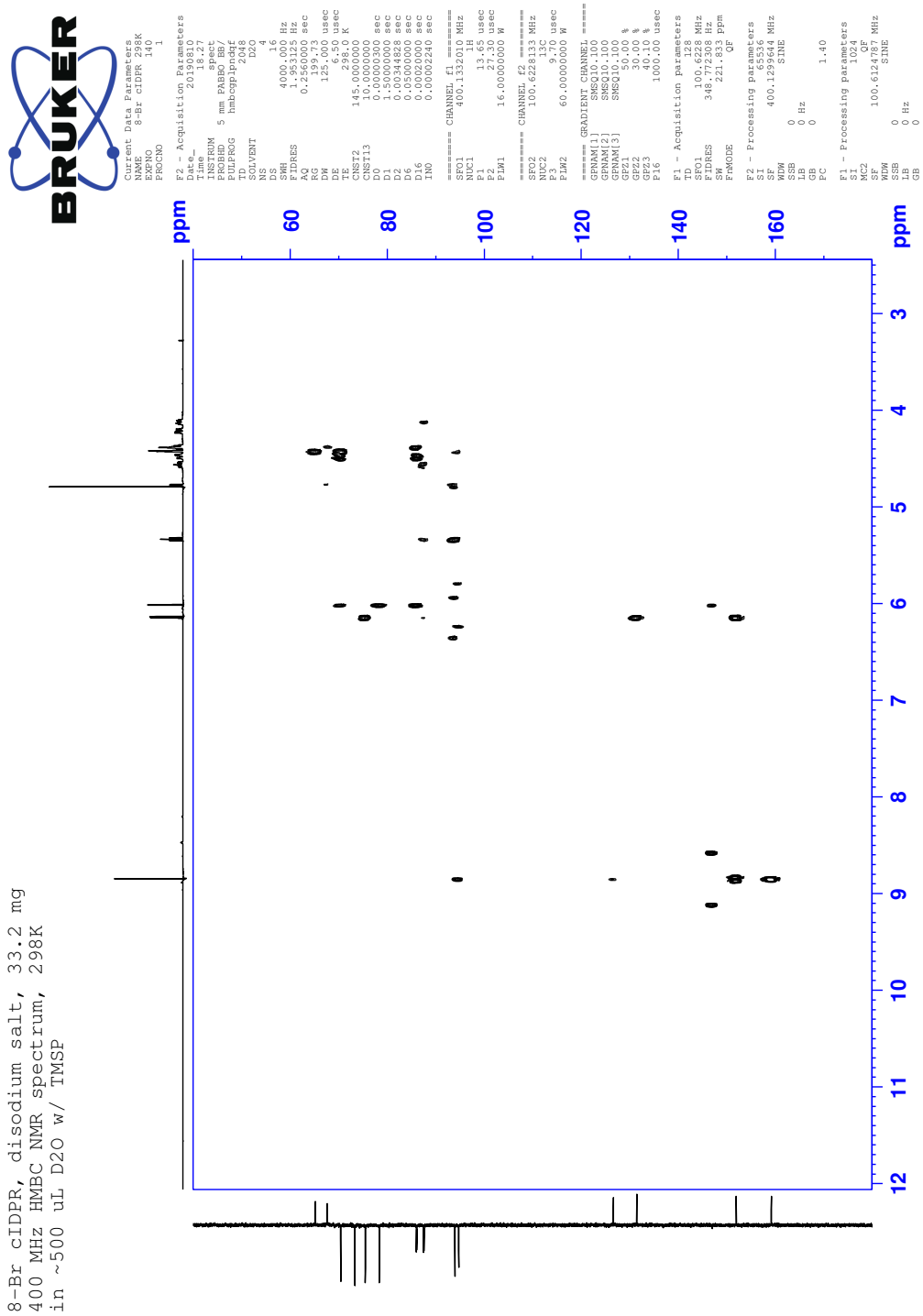


**Appendix 8.** HMBC spectrum of 8-Br-N1-cIDPR, at 298K.

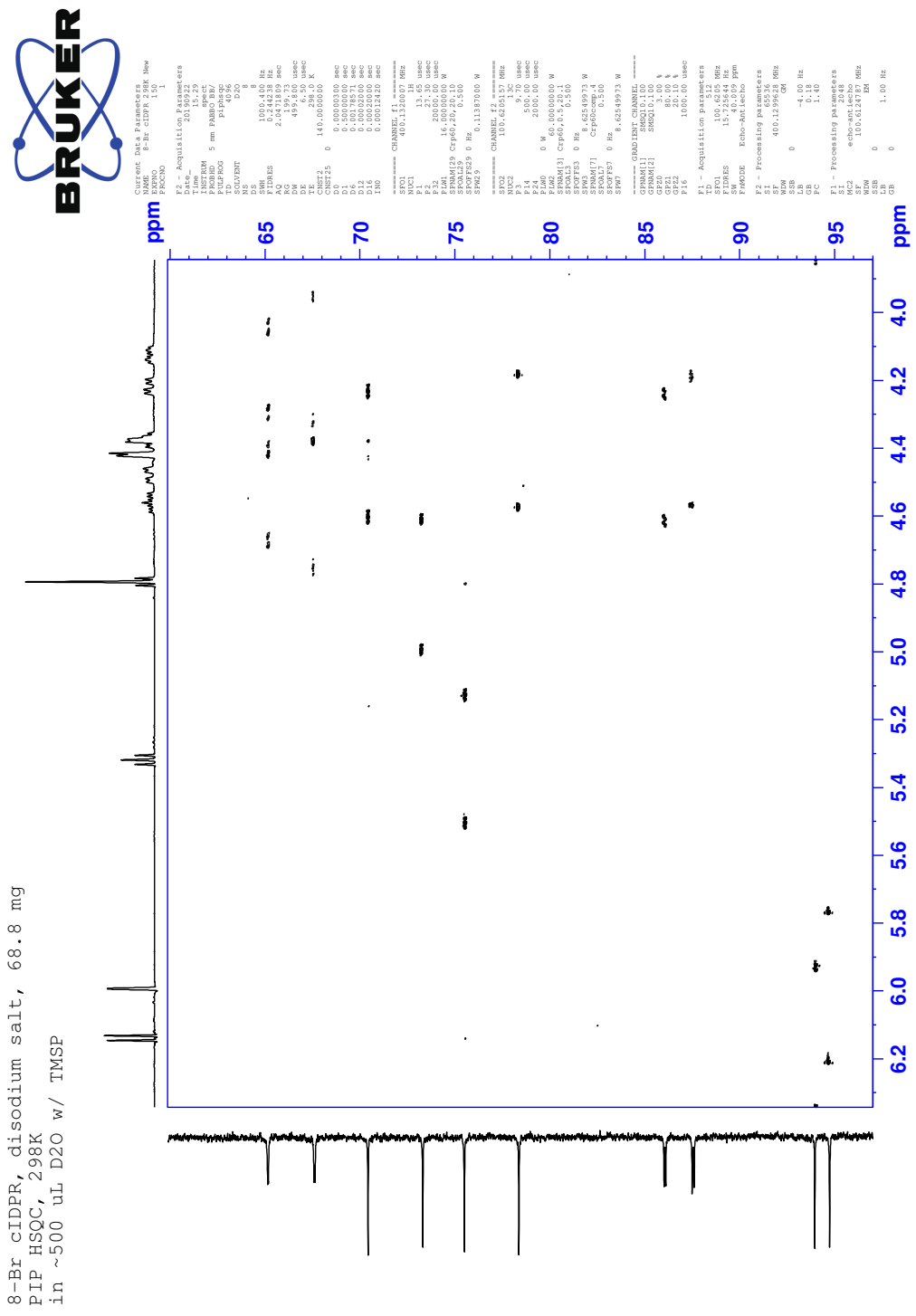


**Appendix 9.** PIP-HSQC spectrum of 8-Br-N1-cIDPR, at 298K.

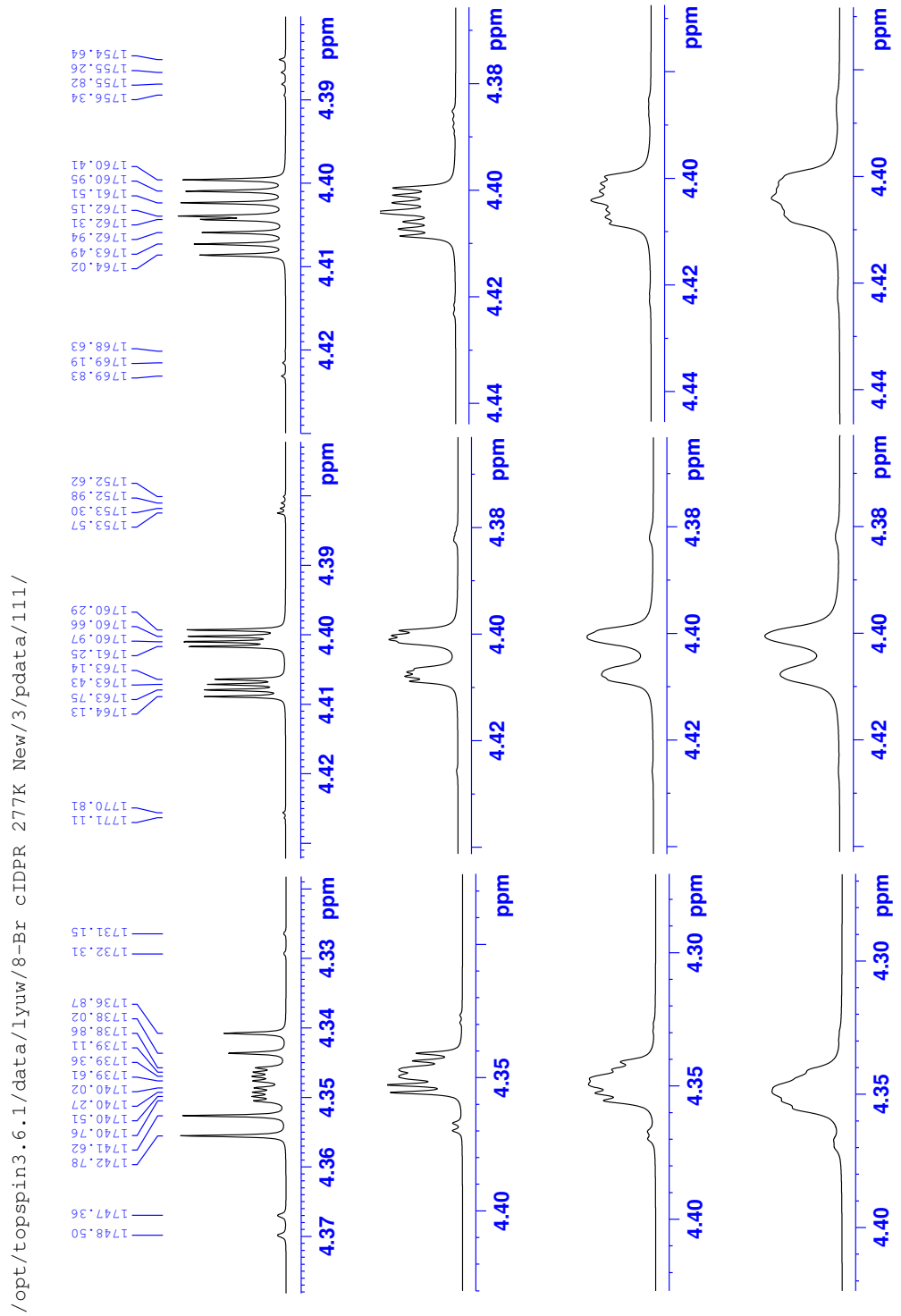


**Appendix 10.** Simulation spectra of non-first order signals of 8-Br-N1-cIDPR.

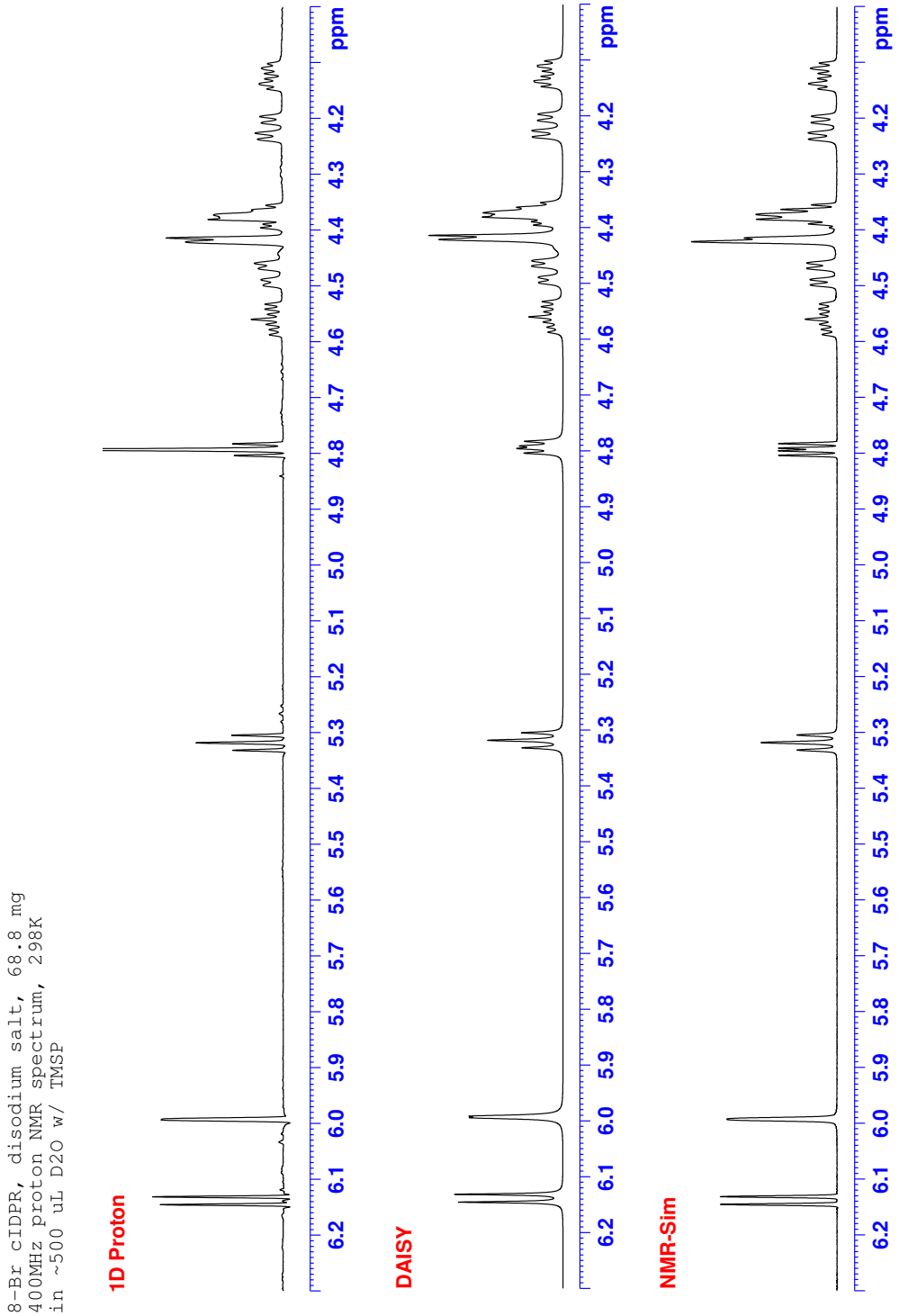


**Appendix 11.** Experimental and simulated $^{1}$H spectra of 8-Br-N1-cIDPR, at 298K.

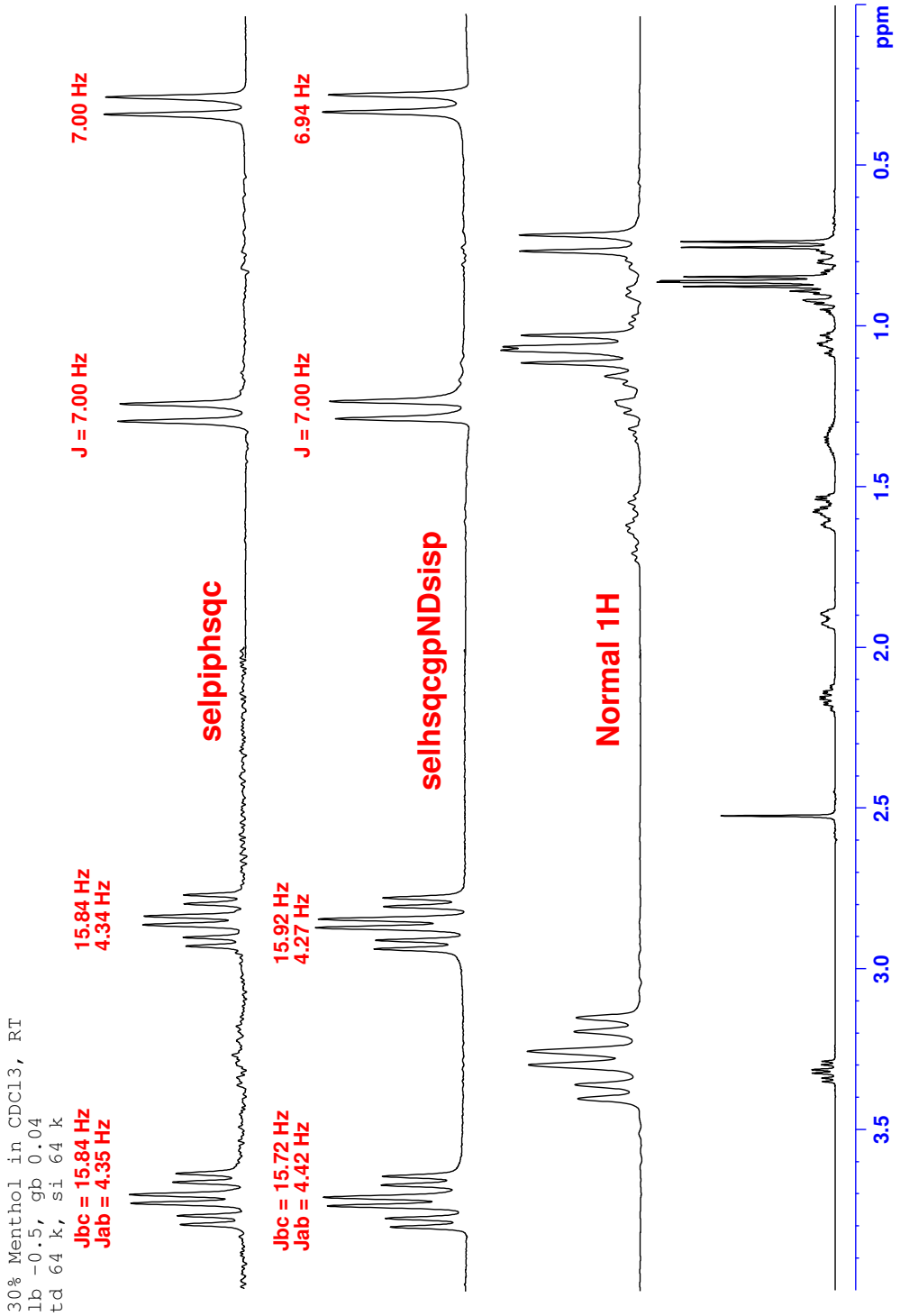


**Appendix 12.** Comparison of selpiphsqc and selhsqcNDsisp spectra of 30% menthol in $CDCl_3$, at RT.

## REFERENCES


1. Warburg, O.; Charistian, W. P. The Hydrogen-transferring Component of the Fermentation Enzymes. *Biochemische Zeitschrift* **1936,** 287-291.
2. Chambon, P.; Weill, J. D.; Mandel, P. Nicotinamide Mononucleotide Activation of New DNA-dependent Polyadenylic Acid Synthesizing Nuclear Enzyme. *Biochem. Biophys. Res. Commun.* **1963,** *11,* 39-43.
3. Chini, C.; Tarrago, M.; Chini, E. NAD and the Aging Process: Role in Life, Death and Everything in Between. *Mol. Cell Endocrinol* **2017,** *455,* 62-74.
4. Nikiforov, A.; Kulikova, V.; Ziegler, M. The human NAD metabolome: functions, metabolism, and compartmentalization. *Grit Rev. Biochem. Mol. Biol* **2015,** *50* (4), 284-297.
5. Gomes, A. P.; Price, N. L.; Ling, A. J. Y.; Moslehi, J. J.; Montgomery, M. K.; Rajman, L.; White, ; etc. Declining NAD(+) Induces a Pseudohypoxic State Disrupting Nuclear-Mitochondrial Communication During Aging. *Cell.* **2013,** *155,* 1624-1638.
6. Massudi, H.; Grant, R.; Braidy, N.; Guest, J.; Farnsworth, B.; Guillemin, G. Age-associated Changes In Oxidative Stress and NAD+ Metabolism In Human Tissue. *PLoS One* **2012,** *7* (e42357).
7. Preyat, N.; Leo, O. Sirtuin deacylases: a molecular link between metabolism and immunity. *Journal of Leukocyte Biology* **2013,** *93* (5), 669-680.
8. Vazquez, B. N.; Thackray, J. K.; Serrano, L. Sirtuins and DNA damage repair: SIRT7 comes to play. *Nucleus.* **2017,** *8* (2), 107-115.
9. Houtkooper, R. H.; Pirinen , E.; Auwerx, J. Sirtuins as Regulators of Metabolism and Healthspan. *Nat. Rev. Mol. Cell Biol.* **2013,** *13,* 225-238.
10. Diefenbach, J.; Bürkle, A. Poly-ADP-ribosylation In Health and Disease. *Cell Mol. Life Sci.* **2005,** *62,* 721-730.
11. Rack, J. G. M.; Perina, D.; Ahel, I. Macrodomains: Structure, Function, Evolution, and Catalytic Activites. *Annu. Rev. Biochem.* **2016,** *85,* 431-454.
12. Leung, A. K. L.; McPherson , R. L.; Griffin, D. E. Macrodoman ADP-ribosylhydrolase and the pathogenesis of infectious diseases. *PLoS Pathog.* **2018,** *14* (3), e1006864.
13. Fehr, A. R.; Channappanavar, R.; Jankevicius, G.; Fett, C.; Zhao, J.; Athmer, J.; Meyerholz, D. K.; Ahel, I.; Perlman , S. The conserved coronavirus macrodomain promotes virulence and suppresses the innate immune response during severe acute respiratory syndrome coronavirus infection. *mBio* **2016,** *7* (6), e01721-e01716.
14. Mehta, P.; McAuley, D. F.; Brown, M.; Sanchez, E.; Tattersall, R. S.; & Manson, J. J. COVID-19: consider cytokine storm syndromes and immunosuppression. *Lancet.* **2020,** *395* (10229), 1033-1034.
15. Curtin, N.; Bányai, K.; Thaventhiran, J.; Le Quesne, J.; Helyes, Z.; Bai, P. Repositioning PARP inhibitors for SARS-CoV-2 infection (COVID-19): a new

multi-pronged therapy for ARDS? *Br J Pharmacol.* **2020,** https://doi.org/10.1111/bph.15137.

16. Lee, H. C.; Aarhus, R. ADP-ribosyl Cyclase: An Enzyme That Cyclizes NAD+ Into a Calcium-mobilizing Metabolite. *Cell Regul.* **1991,** *3,* 203-209.
17. States, D. J.; Walseth, T. F.; Lee, H. C. Similarities In Amino Acid Sequences of Aplysia ADP-ribosyl Cyclase and Human Lymphocyte Antigen CD38. *Trends Biochem. Sci.* **1992,** *17,* 495.
18. Thomas, J. M.; Masgrau, R.; Churchill, G. C.; Galione, A. Parmacological characterization of the putative cADP-ribose receptor. *Biochem.* **2001,** *359,* 451-457.
19. Eisner, D. A.; Caldwell, J. L.; Kistamas , K.; Trafford , A. W. Calcium and excitation-contraction coupling in the heart. *Circ. Res.* **2017,** *121,* 181-195.
20. Lee, H. C. Physiological functions of cyclic ADP-ribose and NAADP as calcium messengers. *Annu. Rev. Pharmacol. Toxicol.* **2001,** *41,* 317-345.
21. Clapper , D. L.; Walseth, T. F.; Dargie , P. J.; Lee, H. C. Pyridine nucleotide metabolites stimulate calcium release from sea urchin egg microsomes desensitized to inositol trisphosphate. *J. Biol. Chem.* **1987,** *262,* 9561-9568.
22. Tanaka, Y.; Tashjian, A. H. Calmodulin is a selective mediator of Ca2+-induced Ca2+ release via the ryanodine receptor-like Ca21 channel triggered by cyclic ADP-ribose. *Proc. Natl. Acad. Sci* **1995,** *92,* 3244-3248.
23. Bai, N.; Lee, H. C.; Laher, I. Emerging role of cyclic ADP-ribose (cADPR) in smooth muscle. *Pharmacology & Therapeutics* **2005,** *105,* 189-207.
24. Noguchi , N.; Takasawa, S.; Nata, K.; Tohgo, A.; Kato, I.; Ikehata, ; Yonekura, H.; Okamoto, H. Cyclic ADP-ribose binds to FK506-binding protein 12.6 to release Ca2+ from islet microsomes. *J. Biol. Chem.* **1997,** *272,* 3133-3136.
25. Morrissette, J.; Heisermann, G.; Cleary, J. Putative cADP-ribose receptor. *Biochem. J.* **2001,** *359,* 451-457.
26. Partida-Sánchez, S.; Cockayne, D. A.; Monard, S.; Jacobson, E. L.; Oppenheimer, N.; Garvy, B.; Kusser, K.; Goodrich, S.; Howard, M.; Harmsen, A.; Randall, T. D.; Lund, F. E. Cyclic ADP-ribose production by CD38 regulates intracellular calcium release, extracellular calcium influx and chemotaxis in neutrophils and is required for bacterial clearance in vivo. *Nature Medicine* **2001,** *7,* 1209-1216.
27. Yu, P.; Liu, Z.; Yu, X.; Ye, P.; Liu, H.; Xue, X.; Yang, L.; Li, Z.; Wu, Y.; Fang, C.; Zhao, Y.; Yang, F. Direct gating of the TRPM2 channel by cADPR via specific interactions with the ADPR binding pocket. *Cell Reports* **2019,** *27,* 3684-3695.
28. Walseth, T. F.; Lee, H. C. Synthesis and characterization of antagonists of cyclic ADP-ribose induced Ca2+ release. *Biochem. Et Biophys. Acta.* **1993,** *1178,* 235-242.
29. Graham, S. M.; Macaya, D. J.; Sengupta, R. N.; Turner , K. B. cADPR analogues: effect of an adenosine 2'- or 3'-methoxy group on conformation. *Organic letters* **2004,** *6,* 233-236.
30. Ashamu, G. A.; Sethi, J. K.; Galione, A.; Potter, B. V. L. Roles for adenosine ribose hydroxyl groups in cyclic adenosine 5'-diphosphate ribose mediated Ca2+ release. *Biochemistry* **1997,** *36,* 9509-9517.
31. Graff; Graham; Lee. unpublished.

32. Mort, C. J. W.; Migaud, M. E.; Galione, A.; Potter, B. V. L. Aplysia californica medicated cyclisation of novel 3'-modified NAD+ analogues: a role for hydrogen bonding in the recognition of cyclic adenosine 5'-diphosphate ribose. *bioorganic & Med. Chem.* **2004,** *13,* 475-487.
33. Saatori, S. M.; Perez, T. J.; Graham, S. M. Variable-temperature NMR Spectroscopy, Conformational Analysis, and Thermodynamic Parameters of Cyclic Adenosine 5'-Diphosphate Ribose Agonists and Antagonists. *J. Org. Chem.* **2018,** *83,* 2554-2569.
34. Moreau, C.; Ashamu, G. A.; Bailey, V. C.; Galione, ; Guse, A. H.; Potter, B. V. L. Synthesis of cyclic adenosine 5'-diphosphate ribose analogues: a C2' endo/syn "southern" ribose conformation underlies activity at the sea urchin cADPR receptor. *Org. & Biomol. Chem.* **2011,** *9,* 278-290.
35. Wagner, G. K.; Guse, A. H.; Potter, B. V. L. Rapid synthetic route toward structurally modified derivatives of cyclic adenosine 5'-diphosphate ribose. *J. Org. Chem.* **2005,** *70,* 4810-4819.
36. Lee, H. C.; Aarhus, R. Wide distribution of an enzyme that catalyzes the hydrolysis of cyclic ADP-ribose. *Biochim. Biophys. Acta.* **1993,** *1964,* 68-74.
37. Kirchberger, T.; Moreau, C.; Wagner , G. K.; Fliegert, ; Siebrands, C. C.; Nebel, M.; Schmid, F.; Harneit, A.; Odoardi, F.; Flugel, A.; Potter, B. V. L.; Guse, A. H. 8-bromo-cyclic inosine diphosphoribose: towards a selective cyclic ADP-ribose agonist. *Biochem. J.* **2009,** *422,* 139-149.
38. Bailey, V. C.; Sethi, J. K.; Fortt, S. M.; Galione, A.; Potter, B. V. L. 7-Deaza cyclic adenosine 5'-diphosphate ribose: first example of a Ca2+-mobilizing partial agonist related to cyclic adenosine 5'-diphosphate ribose. *Chem. & Biol.* **1997,** *4,* 51-61.
39. Oliviero, G.; D'Errico, S.; Borbone, N.; Amato, J.; Piccialli, V.; Varra, M.; Piccialli, ; Mayol, L. A solid-phase approach to the synthesis of N-1-alkyl analogues of cyclic inosine-diphosphate-ribose. *Tetrahedron* **2010,** *88* (10), 1931-1936.
40. Zhang , F. J.; Yamada , S.; Gu, Q. M.; Shi, C. J. Synthesis and characterization of cyclic ATP-ribose: a potent mediator of calcium release. *Bioorganic & med. chem. lett.* **1996,** *6,* 1203-1208.
41. Kilpatrick, J. E.; Pitzer, K. S.; Spitzer, R. J. *Am. Chem. Soc.* **1947,** *69,* 2483-2488.
42. Castañar, L.; J., S.; T., W. R.; Virgili, A.; T., P. Pure in-phase heteronuclear correlation NMR experiments. *Angew. Chem. Ed.* **2014,** *53,* 8379-8382.
43. Roelen, H.; Veldman, N.; Spek, A. L.; Kinzel , J. V. D.; Mathot, R. A. A.; Ijzerman, A. P. N6,C8-Disubstituted Adenosine Derivatives as Partial Agonists for Adenosine A1 Receptors. *J. Med. Chem.* **1996,** No. 39, 1463-1471.
44. Uesugi, S.; Ikehara, M. Carbon-13 Magnetic Resonance Spectra of 8-Substituted Purine Nucleosides. Characteristic Shifts for the Syn Conformation. *J. Am. Chem. Soc.* **1977,** No. 99, 3250-3253.
45. Michelson, A. M. *Biochim. Biophys. Acta.* **1964,** No. 91, 1-13.
46. Kim, D. H.; Hee, S. Q.; Norris, A. J.; Faull, K. F.; Eckhert, C. D. Boric acid inhibits adenosine diphosphate-ribosyl cyclase non-competitively. *J. Chromatogr. A* **2006,** No. 1-2, 246-252.

47. Graham, S. M.; Pope, S. C. NMR solution structure and conformational analysis of the calcium release agent cyclic adenosine 5'-diphosphate ribose. *Nucleosides, Nucleotides & Nucleic Acids* **2001,** No. 20, 169-183.
48. Silverstein, R. M.; Webster, F. X.; Kiemle, D. J.; Bryce, D. L. *Spectrometric identification of organic compounds ,* 8th ed.; John Wiley & Sons. Inc., 2015.
49. Minch, M. J. Orientational Dependence of Vicinal Proton-Proton NMR Coupling Constants: The Karplus Relationship. *Concepts in Magnetic Resonance* **1994,** No. 6, 41-56.
50. Altona, C.; Sundaralingam, M. Conformational analysis of the sugar ring in nucleosides and nucleotides: new description using the concept of pseudorotation. *J. Am. Chem. Soc.* **1972,** No. 94, 8205-8212.
51. Altona, C.; Sundaralingam, M. Conformational analysis of the sugar ring in nucleosides and nucleotides: improved method for the interpretation of proton magnetic resonace coupling constants. *J. Am. Chem. Soc.* **1973,** No. 95, 2333-2344.
52. van Wijk, J.; Haasnoot, C. A. G.; de Leeuw, F. A. A. M.; Huckriede, B. D.; Westra Hoekzema, A. J. A.; Altona, C. *C. PSEUROT6.3* **1999**.
53. Peralla, T.; Espinosa, J. F. *Prog. Nucl. Magn. Ewson. Spectrosc.* **2013,** No. 73, 17-55.

# Vita

| | |
|---|---|
| Name | *Wenjie Lyu* |
| Baccalaureate Degree | *Bachelor of Science*, *St. John's University, New York*<br>*Major: Biology* |
| Date Graduated | *May, 2017* |